Distribution Agreement

In presenting this thesis or dissertation as a partial fulfillment of the requirements for an advanced degree from Emory University, I hereby grant to Emory University and its agents the non-exclusive license to archive, make accessible, and display my thesis or dissertation in whole or in part in all forms of media, now or hereafter known, including display on the world wide web. I understand that I may select some access restrictions as part of the online submission of this thesis or dissertation. I retain all ownership rights to the copyright of the thesis or dissertation. I also retain the right to use in future works (such as articles or books) all or part of this thesis or dissertation.

Signature:

_____	_____
Qinyi Lu	Date

DNA Origami in Protein Oligomer Assembly & Mesoscale Self-assembly of DNA Origami Nanorod with Polynucleotide Brush

By

Qinyi Lu

Doctor of Philosophy

Chemistry

_____

Yonggang Ke

Advisor

_____

David Lynn

Committee Member

_____

Vincent Conticello

Committee Member

Accepted:

_____

Kimberly Jacob Arriola, Ph.D.

Dean of the James T. Laney School of Graduate Studies

_____

Date

DNA Origami in Protein Oligomer Assembly & Mesoscale Self-assembly of DNA Origami Nanorod with Polynucleotide Brush

By

Qinyi Lu

B.S., University of Science and Technology of China, 2018

Advisor: Yonggang Ke, Ph.D.

An abstract of

A dissertation submitted to the Faculty of the

James T. Laney School of Graduate Studies of Emory University

in partial fulfillment of the requirements for the degree of

Doctor of Philosophy

in Chemistry

2023

Abstract

DNA Origami in Protein Oligomer Assembly & Mesoscale Self-assembly of DNA Origami Nanorod with Polynucleotide Brush

By

Qinyi Lu

Over the last two decades, research in DNA nanotechnology has seen astonishing growth and has yielded exquisite DNA-based nanostructures that span a broad range of sizes and complexity. DNA origami nanostructures (DONs) have been widely investigated for numerous biomedical applications. This dissertation describes an application using DNA origami to guide protein complexes assembly, and construction of larger DNA nanostructure. Chapter 1 focus on developing a method for controlling the assembly of protein oligomers on DNA nanostructures using a strand replacement strategy, resulting in the production of different protein oligomers. Chapter 2 and 3 both describe the combination of surface-initiated enzymatic polymerization with DNA origami to create stable, polynucleotide brush-functionalized structures can be precisely controlled in terms of composition, morphology, and site-specific location of initiation sites on the origami core. The resulting structures have potential applications in drug delivery and other nanoscale delivery systems. Later, Chapter 4 and 5 include some other work during my PhD journey.

DNA Origami in Protein Oligomer Assembly & Mesoscale Self-assembly of DNA Origami Nanorod with Polynucleotide Brush

By

Qinyi Lu

B.S., University of Science and Technology of Chine, 2018

Advisor: Yonggang Ke, Ph.D.

A dissertation submitted to the Faculty of the

James T. Laney School of Graduate Studies of Emory University

in partial fulfillment of the requirements for the degree of

Doctor of Philosophy

in Chemistry

2023

Table of Content

Chapter 1. Controlling Protein Assembly by Sequentially Regulating Proximity and Valency with A DNA Origami Template

1.1 Abstract

Proteins are critical building blocks that can lead to numerous nanomaterials. Accurate control of protein oligomer assembly is necessary for the formulation of novel protein complexes. Instead of protein-protein interaction, DNA hybridization among protein-DNA conjugates provides more possibility for nanomaterial construction and makes the process more manageable. However, the random DNA-DNA interaction between protein surfaces has limitations with respect to the protein number and the product shape. To overcome this hurdle, other DNA materials may participate in and execute a strand replacement strategy to guide the assembly pathway. In the current work, we developed a method using a C3-symmetry protein-DNA conjugate as elements to form isomeric oligomers on the DNA nanostructure platform. Attachment strands stick out from the DNA nanostructure and bind with protein-ssDNA. The attachment manner can be controlled by strand design, and further impacts the connection among proteins. Replacement strands in different sequences were involved to realize the sequential release of proteins, thereby allowing stepwise connection in designed pathways. With this method, we successfully produce two trimer isomers, linear trimer and Triangle, as well as three tetramer isomers, linear tetramer, Square and the Y shape tetramer. Our approach significantly expands the scope for precise design and assembly of protein oligomers and leads to new insights into the formulation of functional protein complexes.

1.2 Introduction

Cells can be thought to consist of modular supramolecular complexes, each of which performs independent, discrete biological functions. Protein complexes are one of the cornerstones of many biological processes. The assembly of proteins into divinable structures allows for multiple functions in nature, including structural actuation in muscles[1], transport along the membrane via

ion channels[2], and multienzyme catalysts[3]. Synthetic protein assemblies are therefore a promising class of biomaterial that can mimic and surpass the functions of naturally occurring protein assemblies[4, 5]. Proteins in a protein complex are normally bound by noncovalent protein–protein interactions[6, 7], including hydrogen bonding, ionic interactions, Van der Waals forces, or hydrophobic bonds[8, 9]. However, **protein-protein interactions** are physical contacts of high specificity established between two or more certain protein molecules, which restrict connection between other proteins to meet certain scientific demands.

To solve this, protein-DNA conjugate has been used for protein assembly[10]. Since DNA strands with defined lengths and sequences are linked to the protein covalently, the specificity is transferred to the DNA strand from the protein surface[11]. All proteins that attach DNA strands can be bound to each other via DNA hybridization. A protein with only one ssDNA attached can be directly bound with another protein-ssDNA and form a protein dimer[12]. With more than one ssDNA, larger and more complicated structures can be produced. Mirkin *et. al.* has modified a lot of unnatural protein-ssDNA to form 1D[13] and 3D structures[14, 15, 16]. Nonetheless, protein single crystals were assembled with the greatest degree of positional, orientational, and translational order of those protein-ssDNAs[16]. However, existing research has not provided a method to precisely control the connection among proteins. The production of functional protein complexes requires precise control of either the type of protein, the number of proteins, or the mode of connection. **This can be done by using different sequences of DNA handles on proteins and connect them through various double-strand connectors. Also, precise control of DNA handle conjugating sites can guide the protein multimer linkage pattern (Figure 1A). However, misconnection between proteins still highly possible occurs regardless of the DNA handle sites.** In this work, we use DNA origami as a platform to guide the protein-DNA

connection to form shaped protein oligomers. Isomers of trimer and tetramers demonstrated the high controllability of the method.

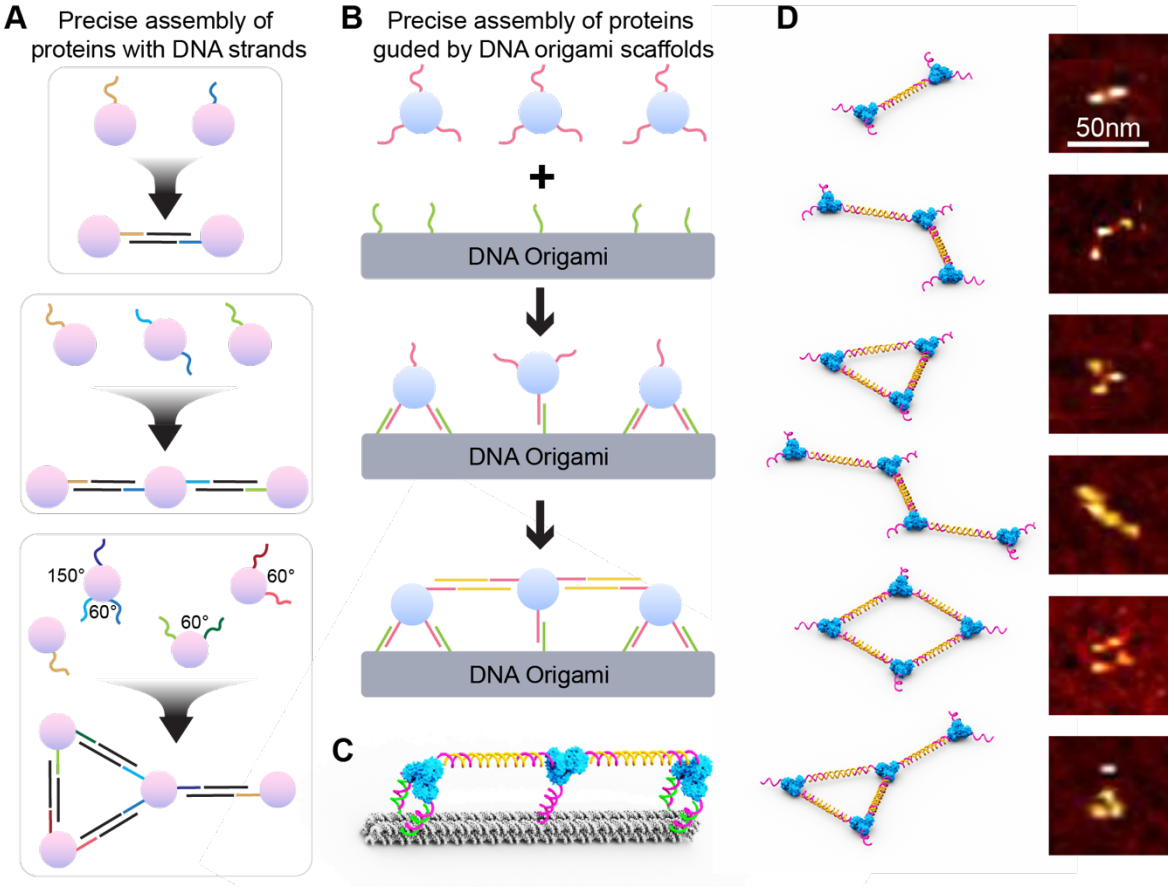

Figure 1. Protein-DNA conjugate connection strategy and multimers production in this work. (A) The way protein dimer, linear trimer and Y shape tetramer are directly connected. (B) Linear protein trimer assembly guided by DNA origami. (C) 3D image showing linear protein trimer attaching on DNA origami. (D) Protein oligomers produced with the DNA origami guidance.

As a proof-of-concept, we used a protein-ssDNA conjugate with super-stable C3 symmetry and a double-stranded connector with sticky ends as the elements (Figure 2A). Without any guidance, the protein-ssDNA will be randomly connected through double-stranded DNA hybridization. Aggregation, oligomers, and the protein monomer with connectors attached may exist together after the hybridization (Supplementary Information Figure S4a). This hypothesis was

demonstrated by the AFM image (Supplementary Information Figure S4b). For this reason, we use DNA origami as a guide. While protein-DNA conjugate is attached to DNA origami, the arrangement pattern and distance among proteins can be designed. Which makes it possible to precisely control protein assemble into the desired shape. Attachment strands were used to bind the protein-ssDNA conjugate to the origami surface. The remaining single-stranded DNA on the protein can be connected via a double-stranded DNA connector. Releasing strands that were complementary to attachment strands would replace the ssDNA and free the protein dimer from the origami (Figure 1B). Compared to a disorder when protein-ssDNA and the connector randomly link, this pathway produces pure dimer theoretical. For more complicated structures, attaching and releasing strands of different sequences will be used to perform the sequential release and connection. In this way, the precisely controlled connection between proteins can be achieved and the protein multimer in the desired forms can be obtained. Besides the simplest protein dimer, linear trimer and Triangle, linear tetramer, Square and Shape Y have been made through this precisely controlled approach (Figure 1D). This method can be an artificial biomolecular pathway to produce protein-protein conjugate, like several enzymes in a pattern for composite reaction. It also provided new insights to guide the assembly of nanoparticles not only in biomolecular but other fields.

1.3 Results and Discussion

1.3.1 (ald-DNA)$_3$ Preparation

The trimeric protein is 2-dehydro-3-deoxyphosphogluconate (KDPG) aldolase (ald), a 25 kDa protein that forms the ald$_3$ with C3-symmetric[17, 18]. The symmetricity and the size of ald$_3$ (6nm diameter, 3nm thickness) are suitable for the shaped protein formation study. Although ald is an enzyme, here we only used it as a structural building block. Glu54, a solvent-exposed residue on

the outer edge of the trimer, was selected as an appropriate site for modification with DNA. We mutated this residue to cysteine (E54C) in order to perform thiol-selective chemistry with the heterobifunctional crosslinker succinimidyl 3-(2-pyridyldithio)propionate (SPDP) and a 5′-amino-modified oligonucleotide. After exposure to 6 equiv of purified SPDP−DNA, a band with higher retention was observed by electrophoresis on a denaturing polyacrylamide gel (SDS-PAGE), corresponding to oligonucleotide-bound ald monomer, in about 50% yield[19] (for more information, see Supplementary Information Section S2).

1.3.2 DNA origami formation & Attachment of ald-DNA to the origami

The 6nm ald is tiny compared to normal hundred-nm-sized origamis. Furthermore, the 3 nm thickness is too thin compared to origamis which contain several layers. To observe how proteins were tethered to the origami structure clearly, here we designed a rather small origami, 4-helix bundle (4HB) with a 1800nt plasmid scaffold produced by plasmid[20] (for design details and sequence information, see Supplementary Information Section S1, S3). The 4HB is only 150nm in length and 5nm in thickness. This size makes it easier to see how proteins are arranged on the origami in AFM images. To assemble the origami, the 50nM scaffold and 5 equiv of staples were mixed in 1×TE and 10mM MgCl2 buffer. The mixture was incubated under 95°C for 5 min, then annealed from 65 to 25°C for 3.5h. The origami was purified through a 0.67% Agarose gel and a freeze column. Binding strands for the attachment of ald-DNA were assembled previously as well as the 4HB formation. Two proteins were attached to the 4HB with one strand, and distance between two protein is 40bp along the 4HB (Figure 2B). The mobility of DNA origami attached with different number of proteins differs in the agarose gel (Figure 2C). After purification, 10 equiv per binding site of ald-DNA was added to the 4HB. To ensure efficient protein binding, the mixture was allowed to sit at 25°C for 48h. After that, the sample will go through a 1% agarose

to remove free ald-DNA. Unfortunately, after attaching the ald-DNA to the 4HB, the protein-origami conjugate has mobility very similar to that of the free ald-DNA, which complicates the purification process (Figure 2E). The AFM image also showed that the ald-origami sample has a large amount of free ald-DNA present even after purification (Supplementary Information Figure S4c). To overcome this obstacle, we engineered a 300nm 4HB dimer that connects two identical 4HB tail to tail via four sticky ends (Figure 2B). Each strand of sticky ends has 10nt domains complementary to the others and the remaining ends hybridize with the remnants of the scaffold on the 4HB tail (for design detail and sequence information, see Supplementary Information Section S1, S3). After only one-pot anneal with the same protocol as the 4HB monomer described above, the 4HB with sticky ends assembles and the tail-to-tail connection forms (Figure 2D, 2E). Agarose gel purified 4HB dimer was then used to attach ald-DNA. The ald-origami conjugate was run on a 1% agarose gel with 4HB dimer as well as ald. Despite the fact that the 4HB dimer has almost the same mobility as free ald-DNA, the ald-4HB dimer can be successfully separated from it (Figure 2E). Further evidence for this comes from the much clearer AFM image of the purified ald-4HB dimer background (Figure 2G).

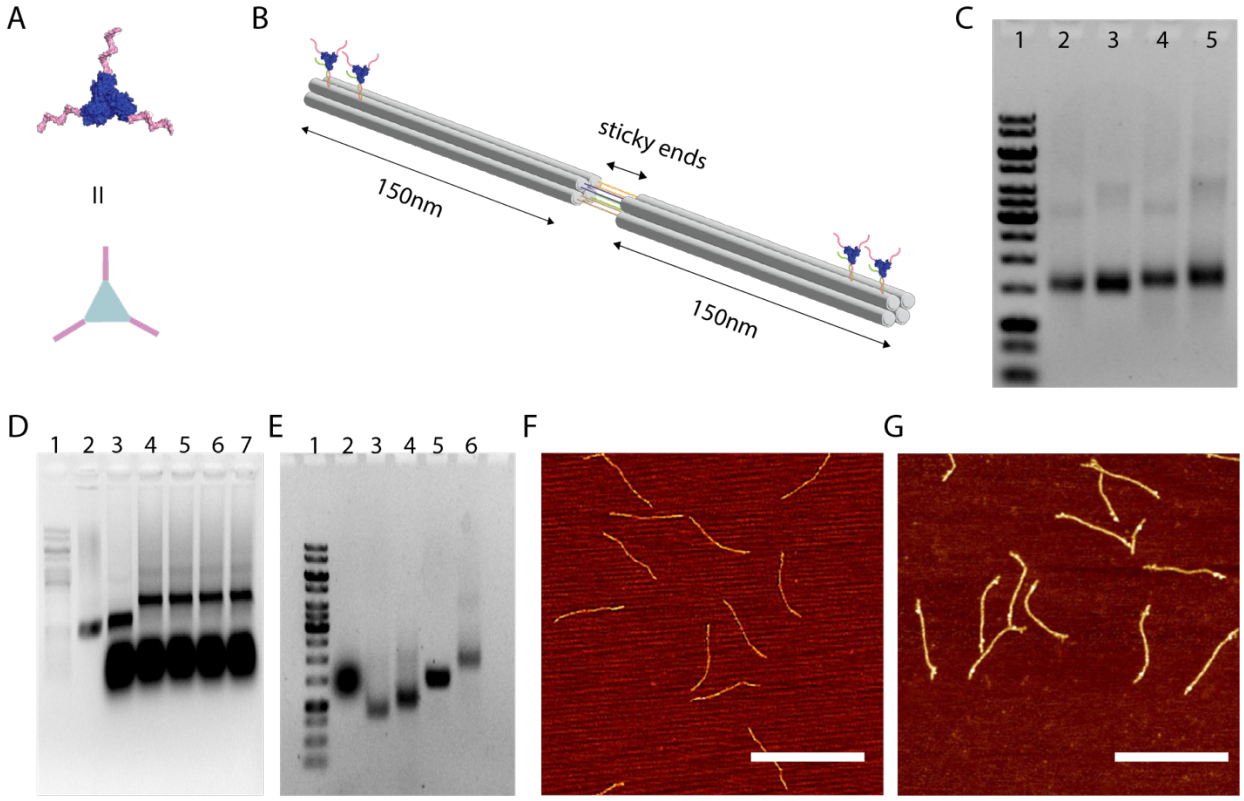

Figure 2. Origami formation, proteins attachment to the origami. (A) Ald-ssDNA. (B) 4HB dimer with two ald-ssDNA attached to it at both ends. (C) Agarose gel of 4HB dimer bind with 2/3/4 ald-ssDNA at ends. Lane 1: 1kb ladder; lane 2: bare 4HB dimer; lane 3: 2 ald each end; lane 4: 3ald each end; lane 5: 4ald each end. (D) Agarose gel of 4HB monomer and dimer. Lane 1: 1kb ladder; lane 2: 1800nt scaffold; lane 3: 4HB monomer; lane 4: 4HB dimer; lane 5: 4HB dimer for 2 ald attachment; lane 6: 4HB dimer for 3 ald attachment; lane 7: 4HB dimer for 4 ald attachment. (E) Agarose gel of 4HB monomer and dimer attaching 2 ald-ssDNA. Lane 1: 1kb ladder; lane 2: free ald-ssDNA; lane 3: 4HB monomer; lane 4: 4HB monomer attached 2 ald; lane 5: 4HB dimer; lane 6: 4HB dimer attached 2 ald on both ends. (F) AFM image of 4HB dimer. (G) AFM image of gel-purified 4HB dimer + 2 ald. Scale bar: 400nm.

1.3.3 ssDNA (on ald) and Connector Length Modification

Prior to initiating the connection, a study of the connector and ssDNA on the ald was performed. We designed a set of connectors to choose the best one for the later experiments. The connector was hybridized by two ssDNA. While two sticky ends are complementary to ssDNA on the protein, the length can be modified by the double-strand domain in the middle. The middle domain length cannot be too long to increase the difficulty of protein binding but would also

need to be greater than 15bp in length to ensure stability. Since both ends of the connectors can bind to the ssDNA, the intramolecular connection might happen to form a loop on one ald-DNA conjugate (Figure 2a). Though the intermolecular connection is desired in all pathways. Our first test used three connectors with middle domain lengths of 15bp, 25bp, and 35bp to bind with ald with 21nt ssDNA, which was reported in a previous study[19]. We mixed ald-DNA and connectors with the molecular ratio of 1:1.5 and incubated overnight and run an 8% native PAGE gel (Figure 2b). If the intermolecular connection dominates, aggregation will occur after mixing the ald-DNA and connectors. In all cases, no aggregation was observed while the brighter band indicates one ald-DNA binding with one or more connectors. Even though higher bands suggested that intermolecular connections partially occurred, this is not good enough for subsequent experiments. Shorter connectors can loosen the loop formed by ald-DNA and connectors. To decrease the total length of the connector, we modified the ssDNA attached to ald from 21nt to 15nt. Two middle domain lengths, 15bp and 21bp were tested at this time. Ald-DNA and connectors were mixed and incubated with the molecular ratio of 1:1.5. Aggregation was observed in all ratios with the shortest connector (15ss + 15bp + 15ss) (Figure 2c). Though single protein-DNA with connectors still existed, it was supposed to be ald-DNA binding a single sticky-end without the loop. Thus, we would use the 15ss + 15bp + 15ss connector for shaped protein multimers connection.

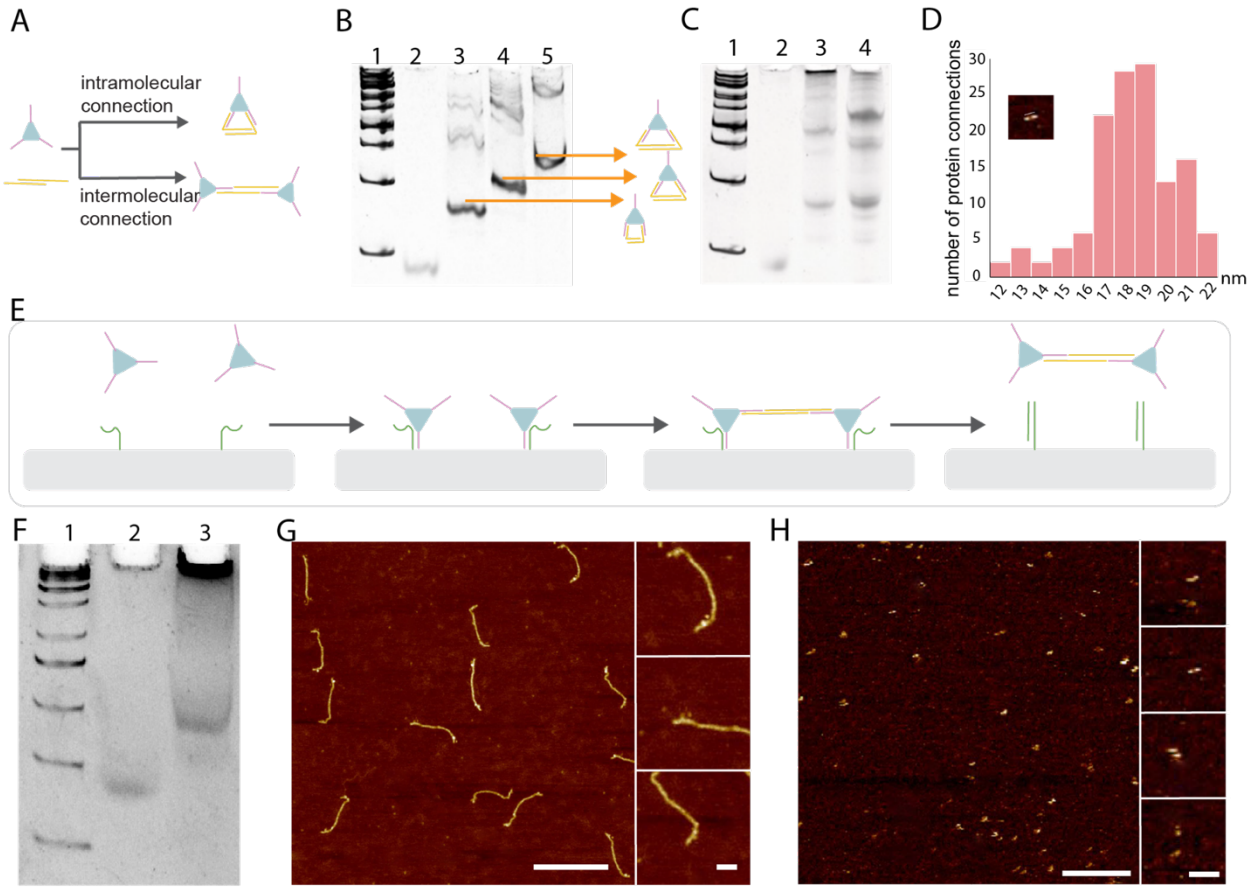

Figure 3. ssDNA on the ald and connection modification and ald dimer formation. (A) Intramolecular and intermolecular connection of ald-ssDNA (B) Native PAGE of ald-21nt ssDNA + connectors, lane 1: 100bp ladder; lane 2: ald-21nt ssDNA; lane 3: ald-ssDNA: (21ss + 15bp + 21ss) connector = 1:1.5; lane 4: ald-ssDNA: (21ss + 25bp + 21ss) connector = 1:1.5; lane 5: ald-ssDNA: (21ss + 35bp + 21ss) connector = 1:1.5. (C) Native PAGE of ald-15nt ssDNA + connectors, lane 1: 100bp ladder; lane 2: ald-15nt ssDNA; lane 3: ald-ssDNA: (15ss + 15bp + 15ss) connector = 1:1.5; lane 4: ald-ssDNA: (15ss + 15bp + 15ss) connector = 1:1.5. (D) Connection lengths measured in ald dimer. (E)Pathway of dimer formation guided by DNA origami. (F) Native PAGE gel of ald dimer released from 4HB dimer. Lane 1: Ultra low range DNA ladder; lane 2: ald-ssDNA; lane 3: ald dimer released from 4HB dimer. (G) AFM image of 2 ald attached at both ends of 4HB dimer. Scale bar: Zoom out 400nm, zoom in 50nm. (H) Recovered ald dimer. Scale bar: Zoom out 200nm, zoom in 50nm.

1.3.4 Connect & Release Ald Dimer

After attaching proteins to the 4HB dimer properly, we finally start the protein multimer production. Each attachment strand is 35nt (15nt +20nt) in length. While the ends close to the origami surface binding with ssDNA on ald, the 3' end toehold is left for the releasing strand

hybridization. When the bridges between proteins formed, releasing strands added after would hybridize with the toeholds at first and gradually take place of the protein (Figure 3E). All releasing strands have 20nt complementary to attachment strand toeholds and 10nt hybridizing with the protein binding domain. A 15nt binding domain was not used here to avoid mis binding with connectors (15nt binding domain of attachment strands is the same as connector sticky ends). After final products are released from the origami, leftover connectors in the solution may bind to the released protein multimer and further cause aggregation. To solve this, a 15nt-blocker will be added to deactivate the extra connector before the last releasing step (Supplementary Information Figure S5a, S5c). The PAGE gel shows little difference whether adding the blocker or not (Supplementary Information Figure S5b). However, after recovering the product from the gel and performing AFM images, a lot of aggregation was found in ald dimer and linear trimer samples assembled without blocker (Supplementary Information Figure S5d, S5e). This observation demonstrated our hypothesis that post-connection exists with the leftover connector.

First, we start with the simplest structure, dimer. Once connected, it can be released from 4HB in one step. In this case, all attachment strands could share the same sequence, and be released by only one type of releasing strand. 4HB dimer with two ald attached to at both ends was purified by agarose gel (Figure 2C) and verified by AFM images (Figure 2G). 5 equiv of connector per connection (5eq for dimer) was added to the sample and leave at 25°C overnight (for connector concentration test, see Supplementary Information Section S5). 4 equiv blocker per connector (20eq for dimer) added then and sit for 1h. Later, 5 equiv of releasing strands per attachment strand (10eq for dimer) was added to let go of the dimer and linear trimer for 3h. We run the product mixture through an 8% native PAGE gel. The origami was stuck in the well because of its large molecular weight, while the band indicate ald dimer were obtained (Figure 3I).

We have tried multiple techniques to recover ald multimers such as alcohol precipitation and freeze column centrifugation. However, these techniques can lead to many broken connections and disassembled ald multimer products. The recovery method we used here protects final products better than other methods. In this method, we cut the band and crush it with a small pestle at room temperature. For each band, 20uL of elution buffer (500mM Ammonium Acetate, 10mM Magnesium Acetate, 2mM EDTA) was added to the crushed gel to absorb the protein products. This method is rather gentle than others and causes less breakage of connection. The recovered ald dimer can be observed by AFM images (Figure 3H), and we reached a decent recovery rate as 84.4%. The recovery rate was calculated by counting the protein number in AFM images. It should be noted that ald is able to aggregate on its own without DNA connections. The total dsDNA length between two connected alds is 45bp. Because it is discontinuous, the actual length could be smaller. With the ald dimension, we consider the connection length from the protein center to center as 12nm to 22nm (Figure 3D). The average length was calculated to be 17.31nm (Supplementary Information Section S7). If the distance between two proteins is less than 12nm, the complex would be perceived as aggregated, and would be discarded while counting the number of proteins. Recovery Rate = Intact product number × product containing ald number / (Intact product number × product containing ald number + all ald number in other shapes) × 100%.

1.3.5 Attachment Manner Modifications for Trimer and Tetramer Assembly

Overall, ald dimer is simple and only has one shape. Thus, we move forward to attach three ald-ssDNA to 4HB ends and connect them into trimers. The manner in which the ald-DNA is attached to the origami has an impact on the posterior connection. To leave at least one free

ssDNA for connection, one or two "legs" (ssDNA) can be locked bound to the origami. In the case of a dimer connection, regardless of which protein has one or two legs free, they will ultimately form as a dimer. However, for a trimer formation, if all proteins have only one free ssDNA, a single connection between two closely spaced alds will occur while the third connects no one. To avoid an unnecessary release step here, the middle protein must have two free ssDNA to link the proteins on both sides. On the other hand, if alds on the flank have two free ssDNA, it might form dual connection with the middle protein and leave the third protein alone. For the purpose of forming a linear trimer in one step, a design of the middle protein has two free ssDNA and the rest have one ssDNA was decided (Figure 4A).

Since two legs of the bilateral proteins should be locked on the origami surface, we studied the specific locations of two attachment strands. Two legs would bind with two attachment strands from nearby helixes, while the distances along the 4HB are 0, 8, and 16bp, which means the total distances of two legs in three designs are 2.5, 3.7, and 5.9nm (Figure 4B). It is possible that two attachment strands can bind two individual proteins instead of one, but the agarose gel result showed that only one protein was attached to the 4HB in all three cases (Figure 4C). Despite the fact that all three designs can be used, 0bp one can provide more flexibility for the protein to move and connect.

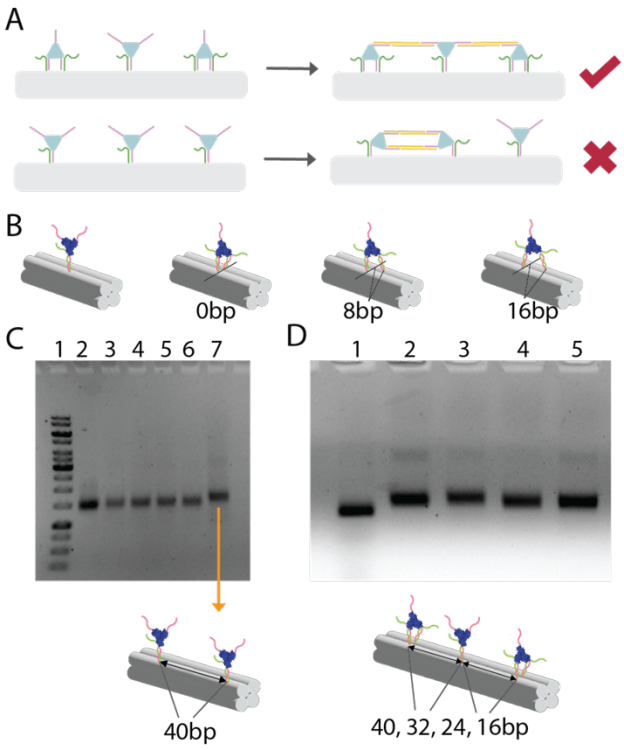

Figure 4. Attachment strands for 3 ald-ssDNA on 4HB design. (a) Two arrangements of three ald-ssDNA attached on the origami. From the top to the below, the middle protein has one leg locked and the flank two have two legs locked; all three proteins have one leg locked. (b) One leg attaches to one helix, and two legs bind from nearby helixes, while the distances along the 4HB are 0, 8, and 16bp. (c) Agarose gel of 4HB dimer with one or two ald-ssDNA attached at ends. Lane 1: 1kb ladder; lane 2: bare 4HB dimer; lane 3: 1 ald 1 leg; lane 4: 1 ald 2legs (0bp); lane 5: 1 ald 2legs (8bp); lane 6: 1 ald 2legs (16bp); lane 7: 2 ald 1leg (40bp between two ald). (d) Agarose gel of 4HB dimer binding with three ald-ssDNA at ends with four distances between proteins.

Distances between alds along the 4HB should be far enough to prevent mis binding which one leg of side protein may be attached to the middle proteins spot. On the other hand, they should be close enough for the connector(45nt) to hybridize with. Four distances (40, 32, 24, 16bp) from the attachment spot have been tested. After 48h incubation for three-protein binding, we run an agarose gel to analyze the binding efficiency. The lower bands of 24bp and 16bp groups suggested that mis binding discussed above happened to decrease the actual protein number on the origami (Figure 4D). Although both 40bp and 32bp are shorter than connectors, the

biomolecular simulation suggested that 40bp is too long for dual connection of linear trimer proteins[21]. Summarizing these results, 32bp was selected as the final distance between two proteins.

1.3.6 Connect & Release Linear Trimer and Triangle

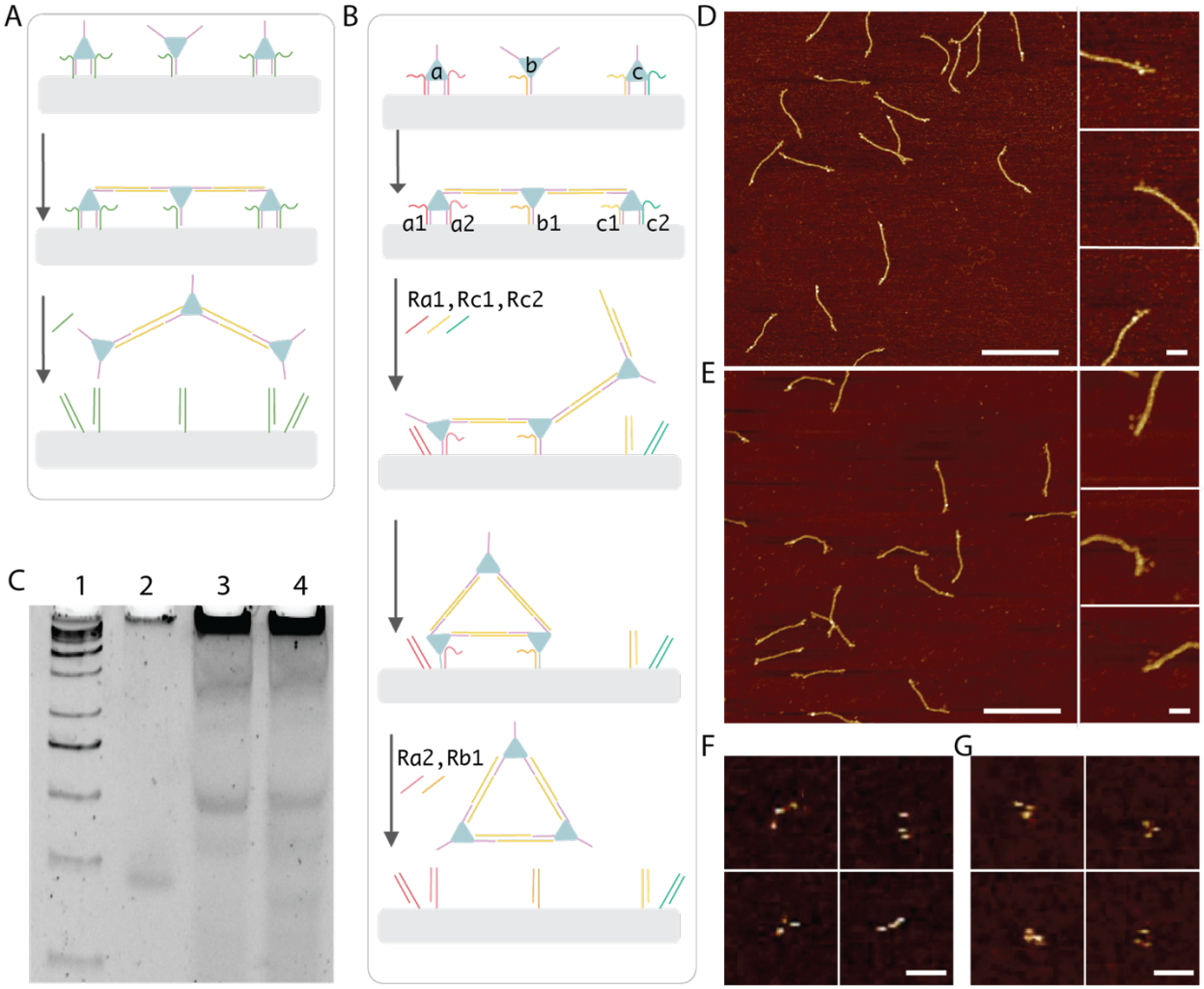

Figure 5. Ald trimer assembly. (A) Pathway of linear trimer assembly. (B) Pathway of triangle assembly. (C) Native PAGE gel of ald trimers released from 4HB dimer. Lane 1: Ultra low range DNA ladder; lane 2: ald-ssDNA; lane 3: linear trimer released from 4HB dimer; lane 4: triangle released from 4HB dimer. (D) AFM image of 3 ald attached at both ends of 4HB dimer. Scale bar: 50nm. (E) AFM image of ald triangle formed at 4HB ends. Scale bar: Zoom out 400nm, zoom in 50nm. (F) Recovered linear trimer. Scale bar: 50nm. (G) Recovered Triangle. Scale bar: 50nm.

When it comes to trimer, two isomers arise, a linear trimer and a triangle. Here we attempt to use DNA origami platform to assemble these two isomers through two different pathways. The pathway of linear trimer assembly is almost the same as the dimer (Figure 5A). Attach three ald-ssDNA to 4HB dimer ends in the manner we decided before and purify the complex by agarose gel. The AFM image can tell that three proteins successfully attached (Figure 5D). Go through the protocol as: 10 eq connector, 25°C overnight; 40 eq blocker, 25°C 1h; 25 eq releasing strands, 25°C 3h. Then we saw a linear trimer band in the PAGE gel (Figure 3C). The product was recovered in the elution buffer and verified by AFM image (Figure 5F). With the successful experience of linear ald products, we moved to stepwise release and connection to produce the ald triangle. For the purpose of realizing stepwise release, differences among attachment strands and releasing strands are required (Figure 5B). After a linear trimer on the 4HB forms, release one leg of the left protein (***a1***) and both legs of the right protein (***c1, c2***). ***Ald c*** moves around and finally binds with the ***ald a*** through the connector left in the environment. Thus, a triangle forms on the 4HB and can be released by other releasing strands (Figure 5A). The process for the ald triangle formation is quite similar to the linear trimer. One additional step is to add 5 equiv of releasing strands ***Ra1, Rc1,*** *and* ***Rc2*** for the formation of Triangle, waiting at least 16h for release and connection. In the AFM image, we can see many 4HB dimers have triangles formed on them (Figure 5E). The blocker is following and the other releasing strands, ***Ra2*** and ***Rb1***, are added then to release the ald Triangle. The triangle has the same mobility as the linear trimer in the PAGE gel (Figure 3C), which may cause impurity in the recovered product. Still, a satisfactory amount of ald triangles was found in the AFM image (Figure 5G). The recovery rates for linear trimer are 77.9%, and Triangle is 44.7%.

1.3.7 Connect & Release Linear Tetramer, Square and Shape Y

The ald Triangle demonstrates the feasibility of our methods. Unlike a triangle is the only 2D isomer of the trimer, the tetramer has more possibilities. Based on this concept, we plan to assemble two 2D tetramers, Square and shape Y, guided by DNA nanostructure. Before a 2D tetramer can be formed, a linear tetramer should first be assembled on the 4HB. To bind four proteins together, 1 ssDNA from ***a*** and ***d*** and 2 ssDNA from ***b*** and ***c*** should be involved. However, ***b*** and ***c*** cannot have 2 free ssDNA to begin with, or ***b*** and ***c*** may double bind, preventing the formation of linear tetramers. When arranging four ald on the 4HB, ***a, c,*** and ***d*** have two legs locked and ***b*** has only one leg locked. Two connections form after adding connectors. In one situation, ***a, b,*** and ***c*** are connected as a linear trimer, while d stands alone. In another case, ***a*** and ***b, c*** and ***d*** are linked as two dimers, and an ssDNA of ***b*** is not connected to anyone. For both situations, releasing one leg of ***c*** can help it connect with the remaining ssDNA and form a linear tetramer. At this step, adding all other six releasing strands would lead to a linear ald tetramer (Figure 6A). Two strategies will be implemented to achieve the goal of assembling two 2D tetramers. With the linear tetramer on the 4HB, releasing ***a1, a2, d1, d2***, then ***a*** and ***d*** will be linked to form a Square. Then releasing ***b1*** and ***c1***, the Square is obtained. For shape Y, ***b1, d1***, and ***d2*** will be released first. After ***b*** connects with ***d***, shape Y forms and ***a1, a2, c1*** can be released (Figure 6B).

The 4HB dimer for tetramer formation and 4 ald-ssDNA attachment to the 4HB dimer process is the same as ald dimer and trimer. After the 4HB dimer with 4 ald at ends was purified, AFM images were taken to verify that four alds were successfully attached. It is more difficult to observe all 4 alds than 2 or 3 since more proteins might be hidden behind or overlay. Nonetheless, we

found some 4 ald on one 4HB end example (Figure 6C). With this sample, 10 equiv of connector was added to the sample and leave at 25°C overnight. Then add 5 equiv of releasing strands ***Rc2,*** waiting 16h for linear tetramer formation. To release linear tetramer, add 40 equiv

blocker and sat for 1h, then add 5 equiv of releasing strands ***Ra1, Ra2, Rb1, Rc1, Rd1*** and ***Rd2*** for 3h. To further form Square and shape Y, add ***Ra1, Ra2, Rd1, Rd2*** for Square and R***b1, Rd1, Rd2*** for shape Y, wait another 16h. In AFM images, we can tell that Square and shape Y formed on the 4HB dimer (Figure 6D, 6E). The Square needs ***Rb1*** and ***Rc1*** while shape Y needs ***Ra1, Ra2*** and ***Rc1*** to incubate for 3h after 40 equiv blocker for 1h. The native PAGE gel showed that all three tetramers have similar mobility (Figure 6F). Therefore, we can only tell the difference between these three results by AFM images of the product (Figure 7G, H, I). Recovery rates for them are linear tetramer 44.8%, Square 35.2%, and shape Y 33.2%.

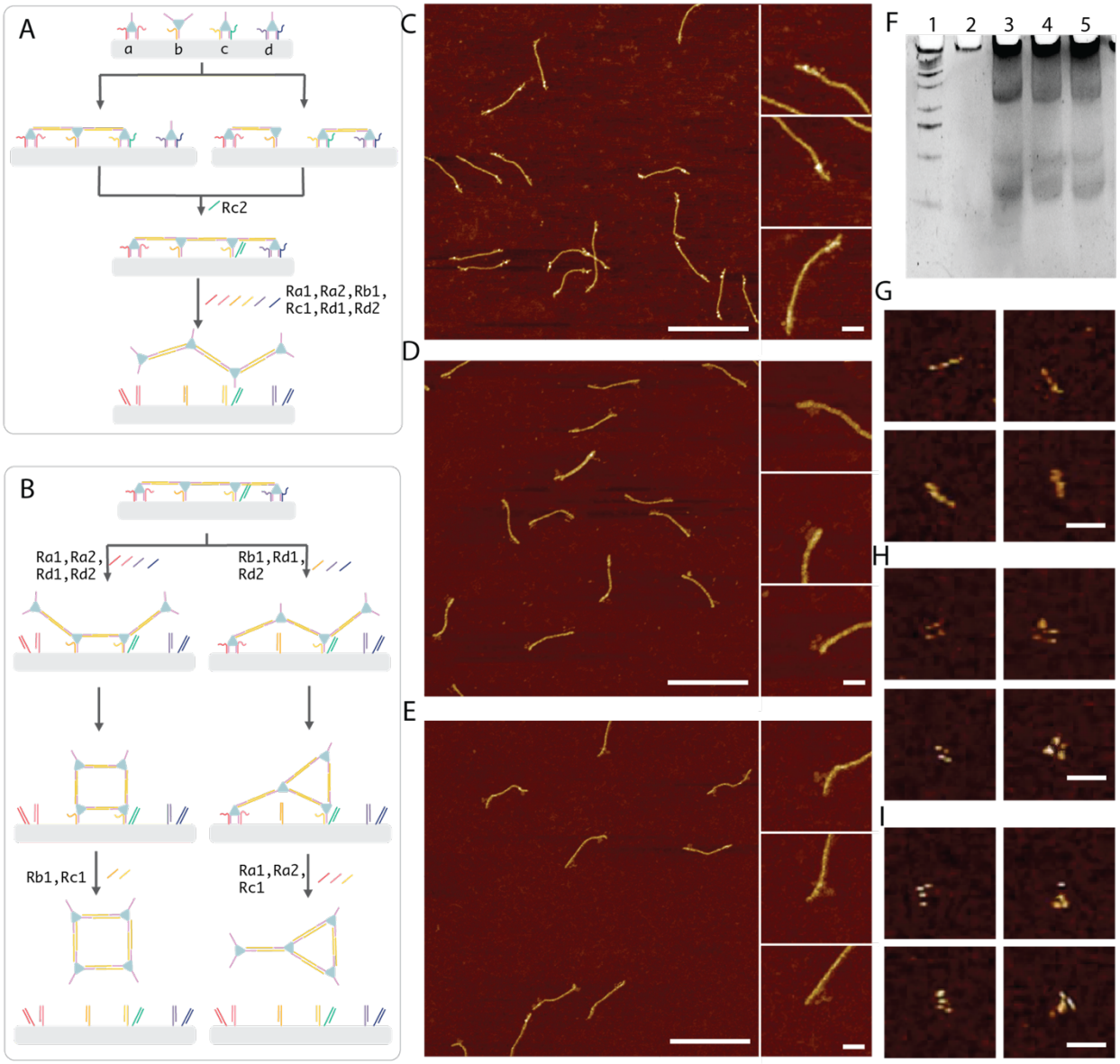

Figure 6. Ald linear tetramer, Square, shape Y assembly. (A) Pathway of linear tetramer assembly. (B) Pathway of Square and shape Y assembly. (C) 4 ald attached at both ends of 4HB dimer. (D) AFM image of Square formed at 4HB ends. (E) AFM image of shape Y formed at 4HB ends. Scale bar: Zoom out 400nm, zoom in 50nm. (F) Native PAGE gel of linear tetramer, Square, shape Y released from 4HB dimer. Lane 1: Ultra low range DNA ladder; lane 2: ald-ssDNA; lane 3: linear tetramer released from 4HB dimer; lane 4: Square released from 4HB dimer; lane 5: shape Y released from 4HB dimer. (G) Recovered linear tetramer. (H) Recovered Square. (I) Recovered shape Y. Scale bar: 50nm.

1.4 Conclusions

To summarize, we have developed an approach that uses DNA origami as a platform, protein-ssDNA as an element to perform strand replacement and connection sequentially, and ultimately achieve isomeric protein oligomers. Only one type of protein-ssDNA conjugate was used here, and three ssDNA bound to the protein share the same sequence. The connector was determined by the character of the protein-ssDNA conjugate. Material restriction increases the difficulty of pathway design. Nevertheless, we successfully conjugated isomers in trimer and tetramer.

This work breaks the prejudice that protein-DNA is mostly used in number-uncertain, supramolecular structure construction, demonstrating that non-existed isomeric protein oligomer can be created through DNA-DNA interaction. Inspired by the existing designed pathway, elevated controlled assembly pathways can be brought up. Take the tetramer as an example, if the ssDNA of ald c has different sequences, two legs can be free for connection, and a linear tetramer can be formed in only one connection step (Supplementary Information Figure S12). Also, protein complexes formed on a 1D origami in this work. A greater topological opportunity will be provided if a move to more complicated DNA nanostructures is made. A 3D structure with more complexity can be achieved then. Ald is not the only protein that can be conjugated to ssDNA and assemble as homomultimeric protein complexes later. Our approach allows for the generation of heteromultimeric protein complexes if other proteins are involved. And this can greatly expand the range of new protein complex designs.

Protein complexes developed in this work perform no function but only exist as a nanomaterial. Broad applicability will be found if functional proteins are used as building blocks via this approach. Scientists normally formulate unnatural protein complexes by means of certain

existing protein-protein interactions while the mode of protein connection is highly restricted to them. Our approach breaks this restriction and will allow the creation of entirely new protein complexes. They will lead to many applications such as multienzyme complexes performing a composite biocatalytic reaction, nanopores in biomembrane, and other biomolecular nanostructures.

1.5 Materials and Methods

1.5.1 Materials and supplies

Materials. The single-stranded DNA scaffold (pscaf1800) was extracted from plasmid with the method developed by Douglas[20]. Chemically synthesized DNA short strands were purchased from IDT (www.idtdna.com) and were used without further purification. All other reagents were purchased from Sigma-Aldrich.

DNA origami design and folding. The DNA origami was designed with the software CaDNAno (http://cadnano.org/). For DNA Origami folding, 10 nM scaffold together with a tenfold excess of each staple strand was mixed in 1×TE (10 mM Tris, 1 mM EDTA; pH 8.0) buffer with 10 mM $MgCl_2$. In the annealing process the folding mixture was heated at 80°C and slowly cooled down from 65°Cto 25°C at the rate of -1°C/5min. Afterwards, the folded DNA origami was purified through Agarose gel electrophoresis.

Agarose gel electrophoresis. DNA origami samples were subjected to agarose gel electrophoresis at 75V for 2-3 hours in an ice water bath. Gels were prepared with 0.5 ×TBE buffer containing 10 mM $MgCl_2$ and 0.005% (v/v) Ethidium Bromide.

Native PAGE gel electrophoresis. DNA oligos and protein samples were subjected to 8% native PAGE gel electrophoresis at 80V for 2-3 hours in the room temperature. Gels were prepared with 0.5 ×TBE buffer containing 10 mM $MgCl_2$, and were stained by 1×Sybr Gold after gel running.

AFM imaging. Take 2 μL samples and deposit onto freshly cleaved mica. Fill the sample area with 80 μL1×TE buffer with 10 mM $MgCl_2$. The samples were imaged on a Multimode VIII system (Bruker) in liquid using commercial tips (SNL-10, Bruker).

Sequence of pscaf1800

AATAGTGGACTCTTGTTCCAAACTGGAACAACACTCAACCCTATCTCGGGCTATTCTTTTGATTTATAAG
GGATTTTGCCGATTTCGGGGTACCTACGAAGAGTTCCAGCAGGGATTCCAAGAAATGGCCAATGAAGATT
GGATCACCTTTCGCACTAAGACCTACTTGTTTGAGGAGTGCCTGATGAATTGGCACGACCGCCTCAGGAA
AGTGGAGGAGCATTCTGTGATGACTGTCAAGCTCCAATCTGAGGTGGGCAAATATAAGATTGTTATCCCT
ATCTAGAAGTACGTCCGCGGAGAACACCTGCCACCCGATCACTGGCTGGATCTGTTACGCTTGCTGGGTC
TGCCTCGCGGCACATCTCTGGAGAAACTGCTGTTCGGTGACCTGCTGAGAGTTGCCGATACCATCGTGGC
CAAGGCTGCTAACCTGAAAGATCTGAACTCACGCGGCCAGGGTGAAGTGACCATCCGCGAATAACTCAGG
GAACTGGATTTGTGGGGCGTGGGTGCTGTGTTCACACTGATCGGCTATGAGGACTCCCAGAGCCGCACCT

AGAAGCTGATCAAGGATTGGAAGGAGCTCGTCAACCAGGTGGGCGACAATATATGCCTCCTGCAGTCCTT
GAAGGACTCACCATACTATAAAGGCTTTGAAGACAAGGTCAGCATCTGGGCAAGGAAACTCGCCGAACTG
GACGATAATTTGCAGAACCTCAACCATATTCGCAGAAAGTGGGTTTACCTCGAACCATACTTTGGTCGCG
GAGCCCTGCCCAAAGAGCAGACCAGATTCAACAGGGTGGGCGAAGATTTCCGCAGCATCATGACATATAT
CAAGAAGGACAATCGCGTCACGCCCTTGACTACCCACGCAGGCATTCTAAACTCACTGCTGACCATCCTG
GACCAATTGCAGAGATGCCAGCGCAGCCTCAACGAGTTCCTGGAGGCGAAGCGCAGCGCCTTCCCTCGCT
TTAACTTCATCGGAGACGATGACCTGCGCGAGATCTTGGGCCAGTCAACCAATTAATCCGTGATTCAGTC
TCACCTCAAGAAGCTGTTTGCTGGTATCAACTCTGGCTGTTTCGATGAGAAGTCTAAGCACTATACTGCA
ATGAAGTCCTTGGAGGGGCAAGTTGTGCCATTCAAGAATAACGTACCCTTGTCCAATAACGTCGAAACCT
GGCTGAACGATCTGGCCCTGGAGATGAAGAAGACCCTGGAGGCGCTGCTGAAGGAGTGCGTGACAACTAG
ACGCAGCTCTCAGGGAGCTGTGGGCCCTTCTCTGTTCCCATCACAGATCTAGTGCTTGGCCGAACAGATC
AAGTTTACCGAAGATGTGGAGAACGCAATTAAAGATCACTCCCTGCACCAGATTGAGTAACAGCTGGTGA
ACAAATTGGAGCAGTATACTAACATCGACACATCTTCCGTAGACCCAGGTAACACAGAGTCCGGTATTCT
GGAGCTGAAACTGAAAGCACTGATTCTCGACGGATCCACGCGCCCTGTAGCGGCGCATTAAGCGCGGCGG
GTGTGGTGGTTACGCGCAGCGTGACCGCTACACTTGCCAGCGCCCTAGCGCCCGCTCCTTTCGCTTTCTT
CCCTTCCTTTCTCGCCACGTTCGCCGGCTTTCCCCGTCAAGCTCTAAATCGGGGGCTCCCTTTAGGGTTC
CGATTTAGTGCTTTACGGCACCTCGACCCCAAAAAACTTGATTTGGGTGATGGTTCACGTAGTGGGCCAT
CGCCCTGATAGACGGTTTTTCGCCCTTTGACGTTGGAGTCCACGTTCTTT

Table S1. Bare 4HB staples

3′ End	Sequence
0[16]	GTAAAGCAAAGGGAGCGCAAGCGT
0[48]	ACCCAAATAAGCCGGCTTTCTCCA
0[80]	CACCTCAGATTGGAGCCGATGGTATCGGCAAC
0[112]	TGGACTCCCAAGTGTACTTTCAGG
0[144]	TAACCACCACACCCGCGGTCACTT
0[152]	CAATTCATCAGGCACTTCGCGGAT
0[176]	GAATAGCCCGCGTGGACACAAATC
0[200]	CCGAAATCTTTCAGCTAGCCGATCAGTGTGAA
0[240]	CCTTCCAAAGCGAGGGTTAATTGGTTGACTGGCCCAAGATCTGGGTCTCAGCTTCT
0[264]	GAGACTGATACTGCTCACCTGGTTGACGAGCT

0[304]	TAGTATGGTTGGTCCATCTCATCGAAACAGCCAGAGTTGAAATCTGGTTCAAGGAC
0[328]	GTATAGTGTCTCCACAGTCTTCAAAGCCTTTA
0[368]	CAAATTATTTGTCCTTACGTTATTCTTGAATGGCACAACTGCCAAGCATCGGCGAG
0[392]	GTTATTGGAGGGCCCATATGGTTGAGGTTCTG
1[55]	TAGAGCTTGACGGGGACAAGTTTTGGACGTACTTCTAGAT
1[79]	TCTCAGCAGGTCACCGCAATCTTATATTTGCC
1[119]	GGCGCTAGGGCGCTGGAACGTCAACATCACAGAATGCTCC
1[143]	AGTTTGGAACAAGAGTGGTCGTGC
1[175]	CGCGCTTAATGCGCCGCTACAGGGCGAGATAGAAGTAGGT
1[247]	CCGGACTCTGTGTTACCTCGCGCAGGTCATCGTCTCCGAT
1[311]	TCACCAGCTGTTACTCTACCAGCAGAGGCTGCGCTGGCAT
1[375]	AAACTTGATCTGTTCGTGCCCCTCTGGGTAGTCAAGGGCG
1[439]	TGAGAGCTGCGTCTAGCAGATCGTCGCCCACCCTGTTGAA
2[24]	GAGATGTGCCGCGAGGTTCTCCGCTTGGGGTCGAGGTGCC
2[56]	CACTACGTGAACCATC
2[72]	AAACCGTCTATCAGGGCGATGGCC
2[96]	TTAGCAGCCTTGGCCATTGACAGTAGGGCGAA
2[120]	CACCCTGGCCGCGTGACCTGAGGCCCACTATTAAAGAACG
2[152]	CAGTTCCCTGAGTTATCCTCAAACGGTTGAGTGTTGTTCC
2[184]	CACAGCACATCCAATCCCCTTATAAATCAAAA
2[216]	AGGTGCGGCTCTGGGACTGCTGGAACTCTTCGTAGGTACC
2[280]	TGCAGGAGGCATATATAACTCGTTAACAGCTTCTTGAGGT
2[344]	TTTCCTTGCCCAGATGTGCCTGCGCAAGGACTTCATTGCA
2[408]	CGAGGTAAACCCACTTGAAATCTTTCAGCCAGGTTTCGAC
3[31]	GATCGGGTGGCAGGTGCAGACCCACCCCGATT
3[79]	AGGGATAAAACAGCAGGAACGTGGCGAGAAAGGAAGGGAA
3[95]	GAAAGCGAAAGGAGCG
3[135]	TCCACTTTGTTCAGATGCGGTCACGCTGCGCG
3[207]	CTTAGTGCGAAAGGTGCCACGCCCTCCGTCGAGAATCAGTGCTTTCAG

3[223]	GGCAAAATTTCATTGGCCATTTCTTGGAATCCGTCCTCATCCAGAATA
3[271]	GAAGTTAATCCTTGATACGGAAGATGTGTCGATGTTAGTA
3[287]	ATCACGGAAAGGCGCTGCGCTTCGCCTCCAGGTGTCGCCCCAATTTGT
3[335]	CTCTGCAATGAGTCCTGCAGGGAGTGATCTTTAATTGCGT
3[351]	CTTAGACTGGATGGTCAGCAGTGAGTTTAGAACTGACCTTTCTTCGGT
3[399]	TGACGCGACGTCCAGTCTAGATCTGTGATGGGAACAGAGA
3[415]	ACAAGGGTCTTGATATATGTCATGATGCTGCGTCTGCGAACAGCTCCC

Table S2. Sticky ends strands sequence

sticky 0	GACTATAGTCCAGGGCTCCGCGACCAAAGTATGG
sticky 1	TCTGGTCTGCTCTTTGAAGTCAGGCA
sticky 2	ATGGCGCCATTCCAGGGTCTTCTTCATCTCCAGG
sticky 3	TTGTCACGCACTCCTTCAGCAGCGTGCCTGACTT

Table S3. Attachment staples and releasing strands (Ra1-Rd2) sequences

a1	CACCTCAGATTGGAGCCGATGGTATCGGCAACTTACCTGACGGAACTCACCGCGCCCCAGCGGGCTAGG
a2	TCTCAGCAGGTCACCGCAATCTTATATTTGCCTTACCTGACGGAACTCAGCACGGCGCCGGAGCCTGCC
b1	TGGACTCCCAAGTGTACTTTCAGGTTACCTGACGGAACTCACCCAGGCGCCCGGGGCGGCG
c1	TAACCACCACACCCGCGGTCACTTTTACCTGACGGAACTCATCCGCTACGACTTCCGGGTC
c2	AGTTTGGAACAAGAGTGGTCGTGCTTACCTGACGGAACTCACGGCGTGTCCGCGCTCGCGC
d1	GAATAGCCCGCGTGGACACAAATCTTACCTGACGGAACTCACATACGCGCGCAAGGCCGGG
d2	CGCGCTTAATGCGCCGCTACAGGGCGAGATAGAAGTAGGTTTACCTGACGGAACTCACCGGTGCGTAGCATGGTCAC
d1 fill	GAATAGCCCGCGTGGACACAAATC

d2 fill	CGCGCTTAATGCGCCGCTACAGGGCGAGATAGAAGTAGGT
Ra1	CCTAGCCCGCTGGGGCGCGGTGAGTTCCGT
Ra2	GGCAGGCTCCGGCGCCGTGCTGAGTTCCGT
Rb1	CGCCGCCCCGGGCGCCTGGGTGAGTTCCGT
Rc1	GACCCGGAAGTCGTAGCGGATGAGTTCCGT
Rc2	GCGCGAGCGCGGACACGCCGTGAGTTCCGT
Rd1	CCCGGCCTTGCGCGCGTATGTGAGTTCCGT
Rd2	GTGACCATGCTACGCACCGGTGAGTTCCGT

Table S4. Connector strands sequences

connector 1a	TTAAGAACCTCTCCG**GAGCAGACCTGACGGAACTCA**
connector 1b	CGGAGAGGTTCTTAA**GAGCAGACCTGACGGAACTCA**
connector 2a	TTAAGAACCTCTCCGTCGTCTGGTATAG**GAGCAGACCTGACGGAACTCA**
connector 2b	CTATACCAGACGACGGAGAGGTTCTTAA**GAGCAGACCTGACGGAACTCA**
connector 3a	AAGAACCTCTCCGTCGTCTGGTATAGATGTGAATGATG**GAGCAGACCTGACGGAACTCA**
connector 3b	CATCATTCACATCTATACCAGACGACGGAGAGGTTCTT**GAGCAGACCTGACGGAACTCA**
connector 4a	TTAAGAACCTCTCCG**ACCTGACGGAACTCA**
connector 4b	CGGAGAGGTTCTTAA**ACCTGACGGAACTCA**
connector 5a	TCGGCGCGATAGGCCGTTAGAG**ACCTGACGGAACTCA**
connector 5b	CTCTAACGGCCTATCGCGCCGA**ACCTGACGGAACTCA**

The original sequence of ssDNA on the ald-ssDNA was 5’ TGAGTTCCGTCAGGTCTGCTCT, after decreasing the length from 21nt to 15nt, the sequence was changed to 5’ TGAGTTCCGTCAGGT. The blocker sequence is same as the ssDNA.

1.5.2 Protein expression, modification and characterization

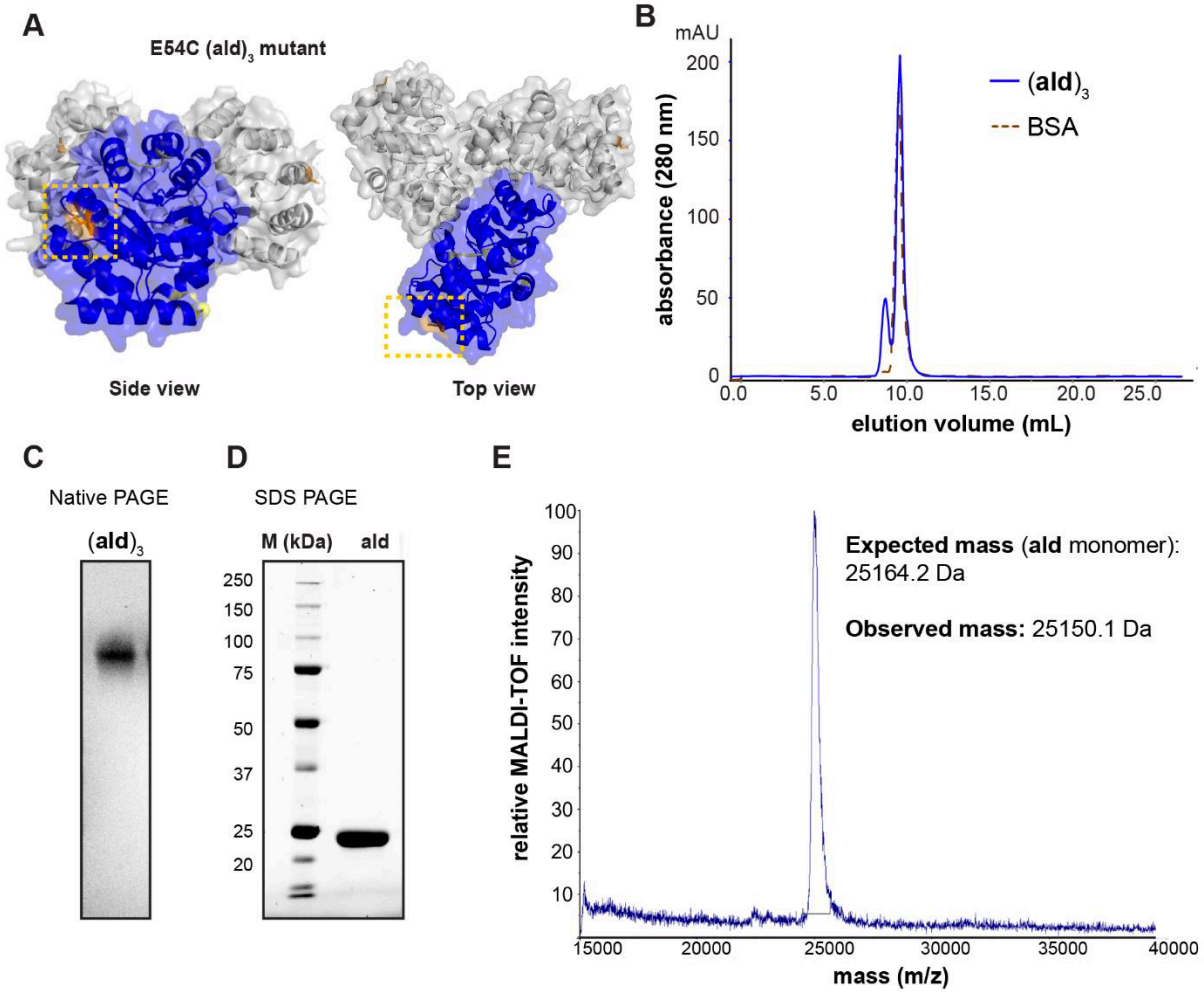

Figure S1. Purification and characterization of aldolase. A) Surface representation of the aldolase trimer: blue indicates one monomer, orange denotes position 54 (mutated to cysteine), and yellow indicates native disulfide bonds. B) Size exclusion chromatogram of the purified trimer. BSA is used as a control given its similar size to the assembled trimer. C) Native PAGE and D) Denaturing SDS-PAGE analysis of the purified aldolase protein. E) MALDI-TOF/TOF mass spectrum of the purified protein.

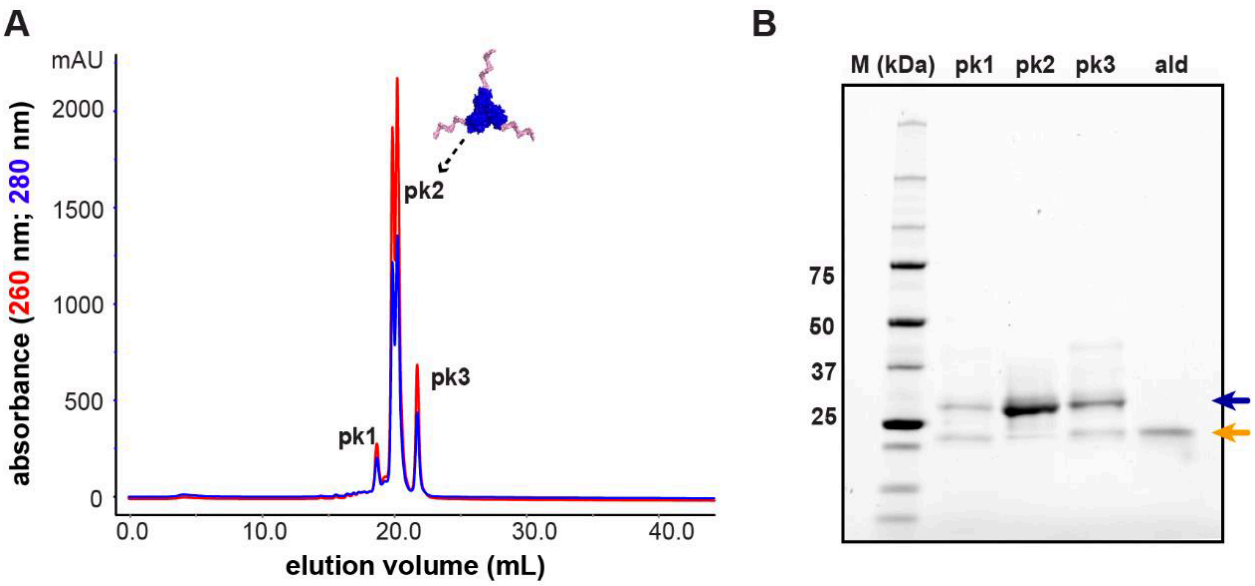

Figure S2: Aldolase-DNA conjugation with SPDP-linked DNA. A) The aldolase-DNA conjugate was purified via anion exchange chromatography. Pk1, 2, and 3 indicate the three sample peaks collected. **B)** SDS-PAGE analysis of the three collected peaks, using wild-type aldolase (**ald**) as a reference. The orange arrow indicates unmodified **ald** and the blue arrow the (**ald**-DNA) conjugate. Pk 2 contains >95% purity of the desired (**ald**-DNA)$_3$ conjugate, and was used for subsequent experiments.

1.5.3 4HB origami and sticky ends for dimerization design

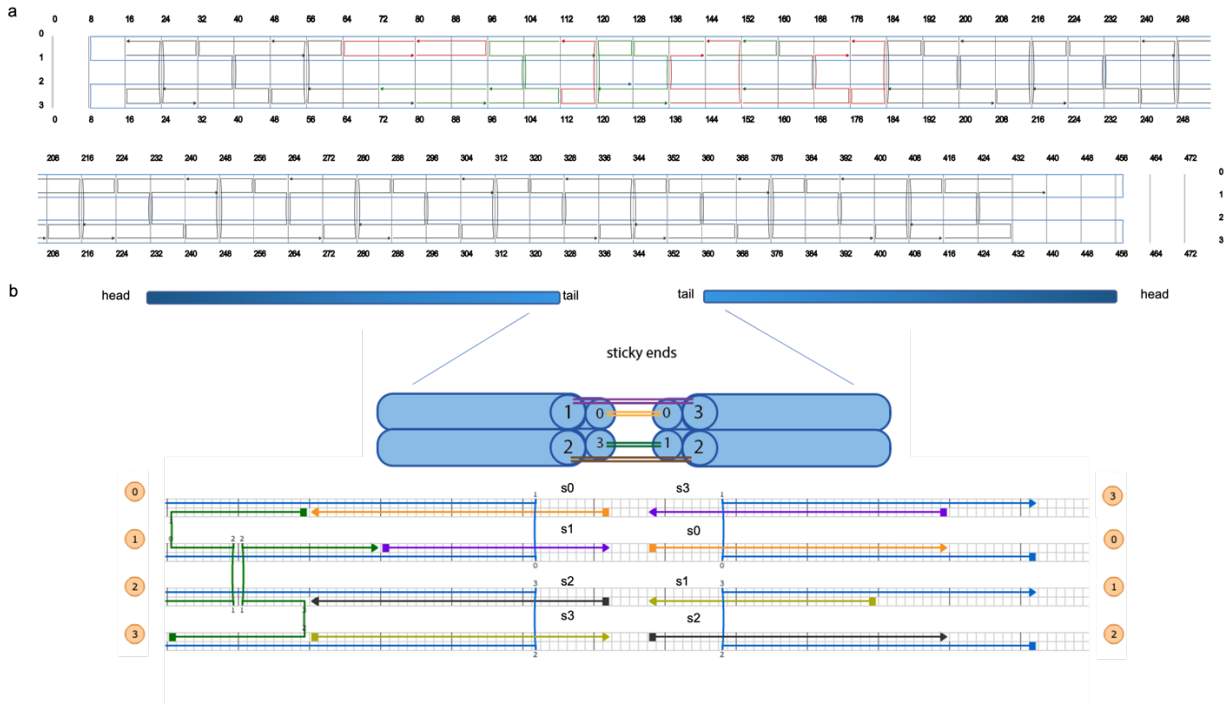

Figure S3. 4HB origami design and sicky ends design. (a) Staple details of scaffold routing and staples of 4HB in the CaDNAno file. Red strands are attachment strands need to be modified. (b) Four sticky end strands at the tail of 4HB (see sequences information in Table S2). Sticky ends are 10nt long. S1 is complementary to s3, s0 and s2 are palindromic and complementary to themselves.

1.5.4 Random protein connection & Blocker deactivation of the extra connector

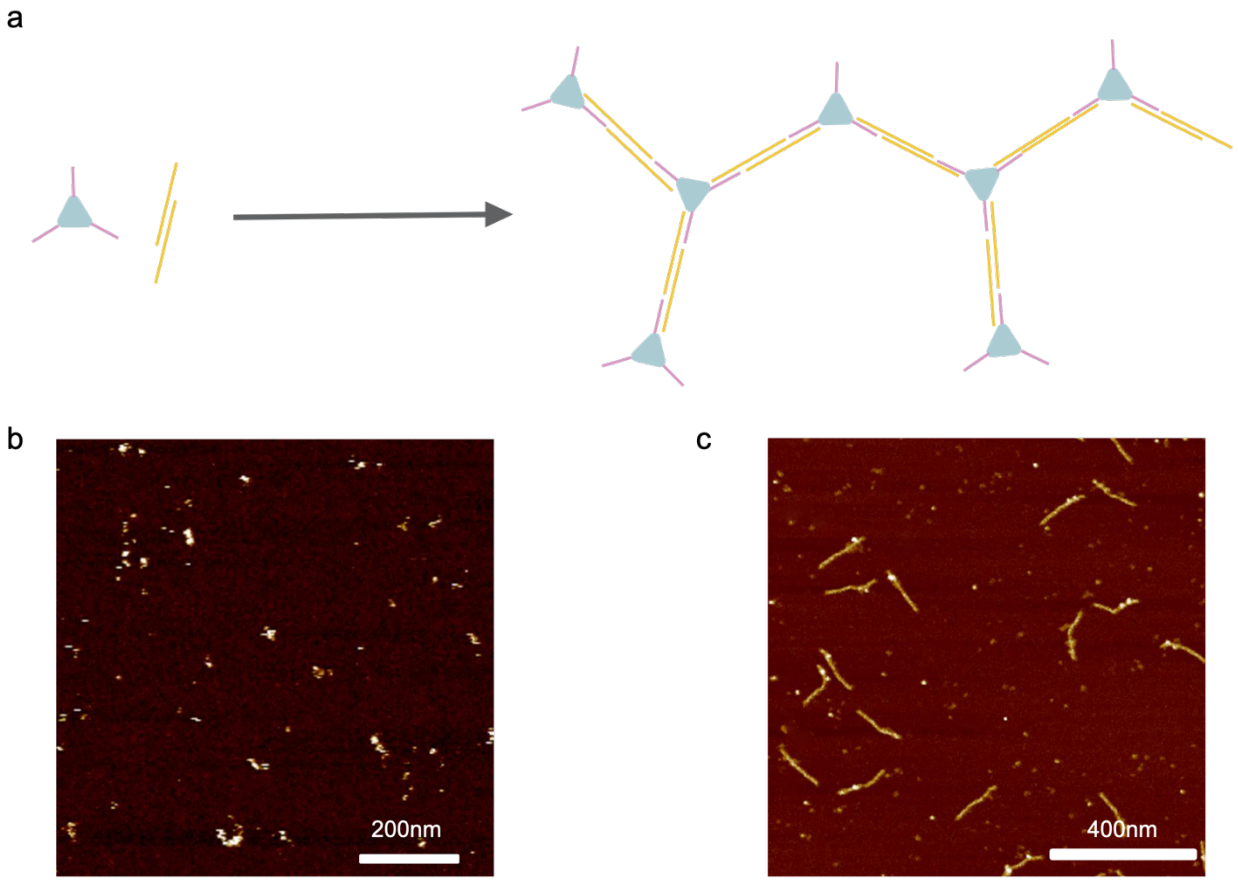

Figure S4. Random protein connection. (a) Illustration of ald-ssDNA + connector random connection. (b) AFM images of ald-ssDNA + 1.5eq connectors connected after 2h. (c) AFM image of agarose gel purified 4HB monomer attached with 2 ald.

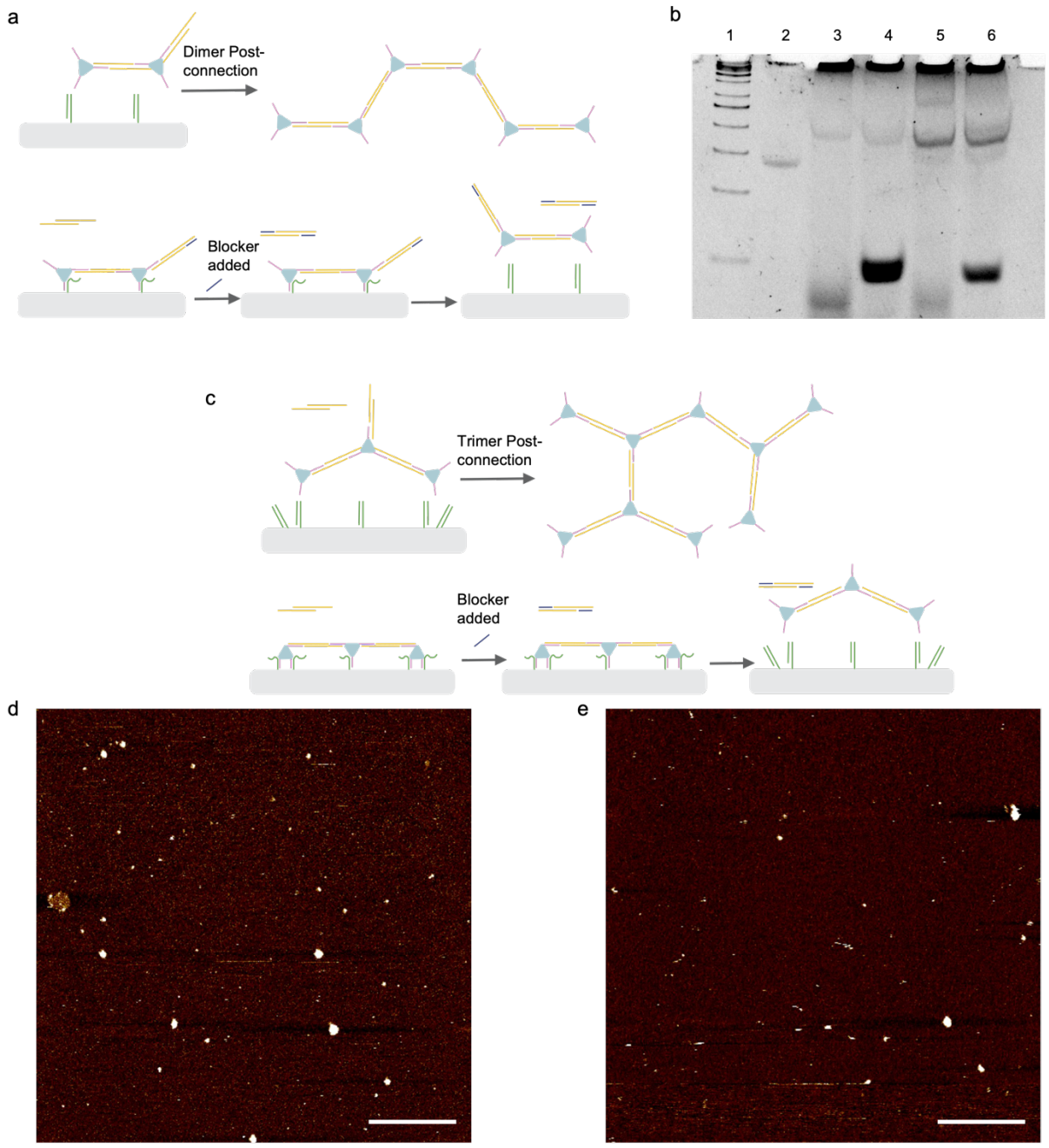

Figure S5. Blocker deactivation of the extra connector. (a) Dimer post-connection without blocker & the way blocker deactivates connector. (b) Native PAGE gel of ald dimer and linear trimer released from 4HB with and without blocker. Lane 1: Ultra low range DNA ladder; lane 2: ald-ssDNA; lane 3: ald dimer released without blocker added; lane 4: ald dimer released after blocker added; lane 5: linear trimer released without blocker added; lane 6: linear trimer released after blocker added. (c) Linear trimer post-connection without blocker & the way blocker deactivates connector.

1.5.5 Connector ratio test, protein distances test, and protein multimer gel result

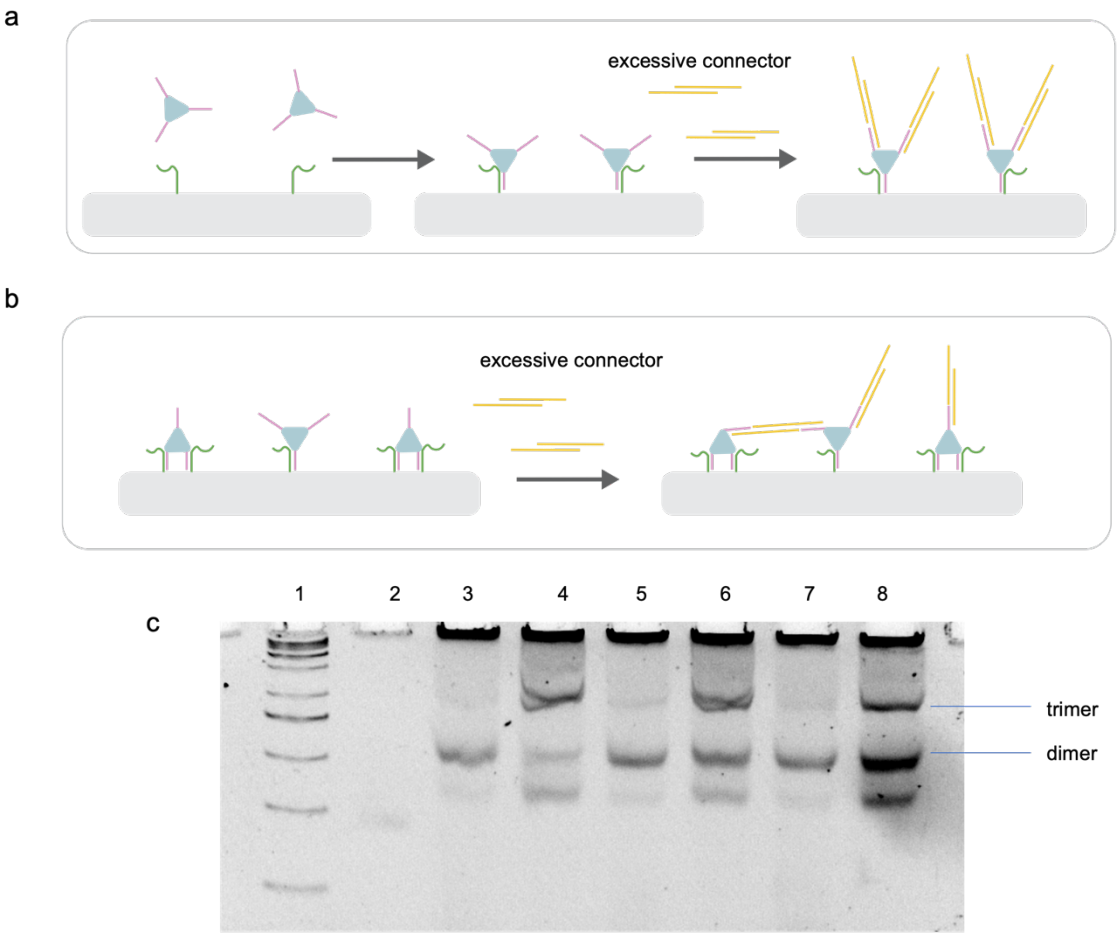

Figure S6. Connector ratio test to avoid connection block by excessive connectors. (a) The way excessive connectors block dimer formation. (b) The way excessive connectors block linear dimer formation. (c) Native PAGE gel of connector ratio test. Lane 1: Ultra low range DNA ladder; lane 2: ald-ssDNA; lane 3: 5eq connectors for dimer formation; lane 4: 10eq connectors for linear trimer formation; lane 5: 10eq connectors for dimer formation; lane 6: 20eq connectors for linear trimer formation; lane 7: 15eq connectors for dimer formation; lane 8: 30eq connectors for linear trimer formation.

Discussion: Basically, the dimer yields have no change from 5 to 15 eq connectors, but for linear trimer, by-products dimer and monomer + connector amounts increase a lot when more connectors existed. Thus, we decided to use 5 eq connectors per connection. That is to say, 5eq connectors for dimer, 10eq for trimer, 10eq for tetramer since only two connectors were needed in the first step, and 8 eq connectors was left for later connection.

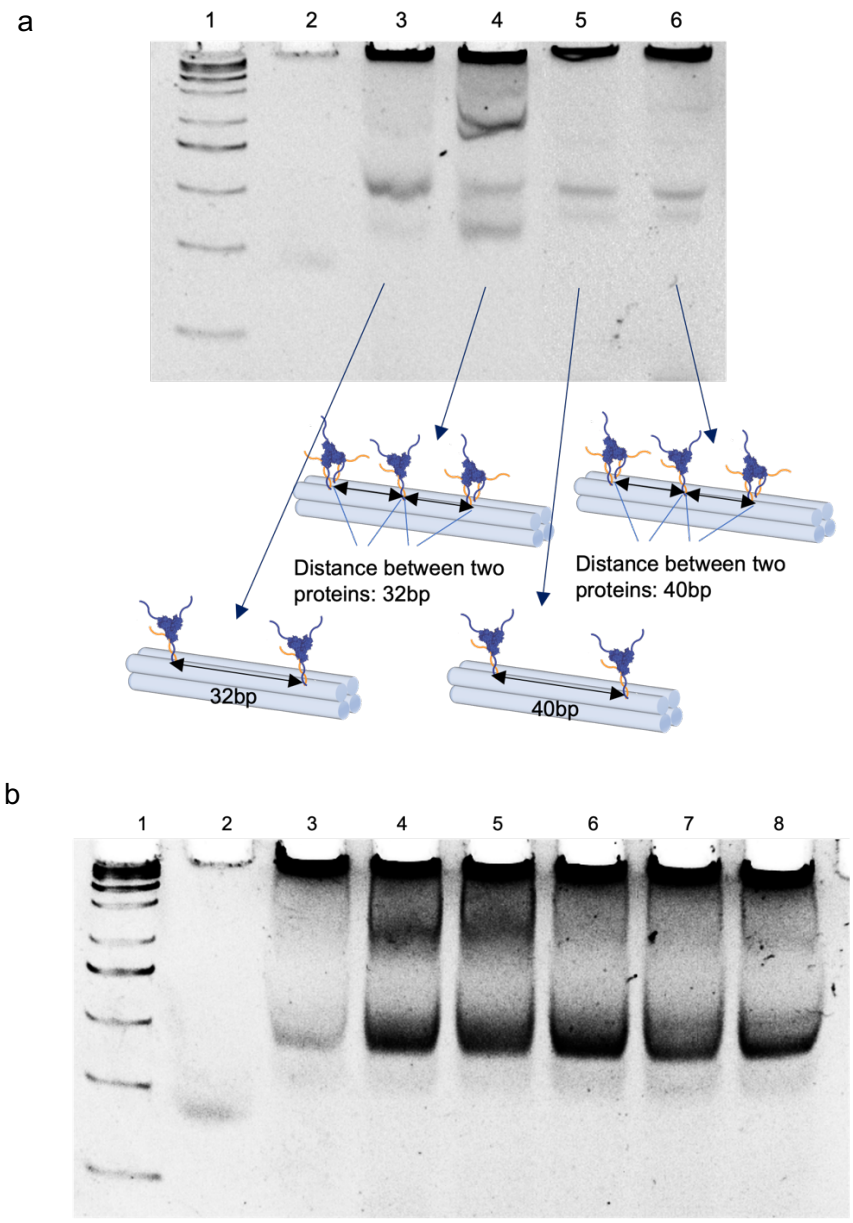

Figure S7. Linear trimer formation comparing protein distances and all protein multimers PAGE gel result. (a) Native PAGE gel of dimer and linear trimer connection comparing the distance of proteins between 32bp and 40bp. Lane 1: Ultra low range DNA ladder; lane 2: bare 4HB; lane 3: 4HB attached 2 ald with 32bp distance; lane 4: 4HB attached with 3 ald with 32bp distance; lane 5: 4HB attached 2 ald with 40bp distance; lane 6: 4HB attached with 3 ald with 40bp distance. (b) Native PAGE gel of all protein products released. Lane 1: Ultra low range DNA ladder; lane 2: free ald; lane 3: ald dimer released; lane 4: linear trimer released; lane 5: Triangle released; lane 6: linear tetramer released; lane 7: Square released; lane 8: Shape Y released.

1.5.6 Protein multimer yield calculation

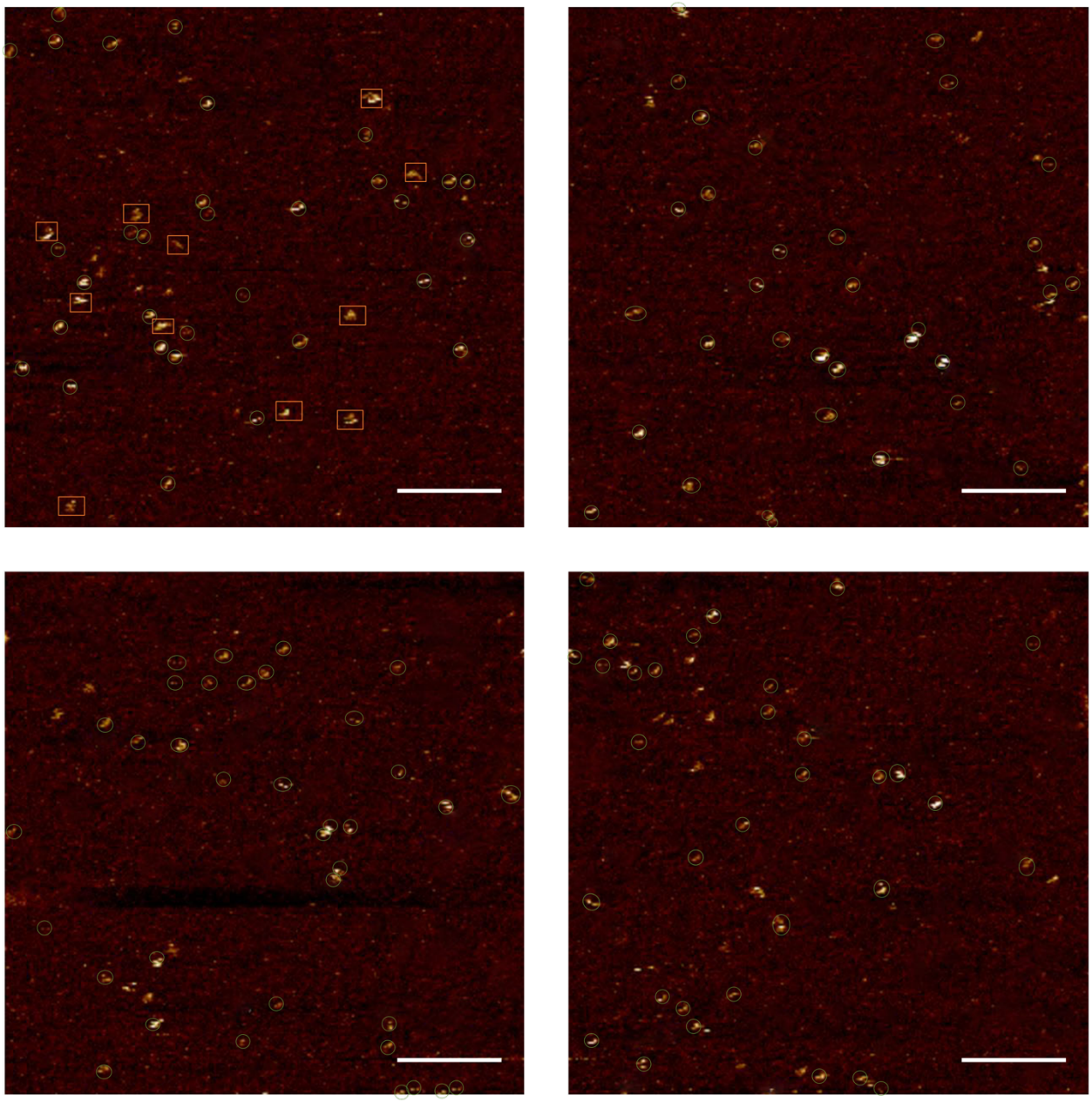

Figure S8. Wide-field AFM images of recovered ald dimer. Ald dimers are in green circles. In the left up penal, protein aggregation was indicated by orange boxes. Other aggregation would not be pointed out. Scale bars: 200nm

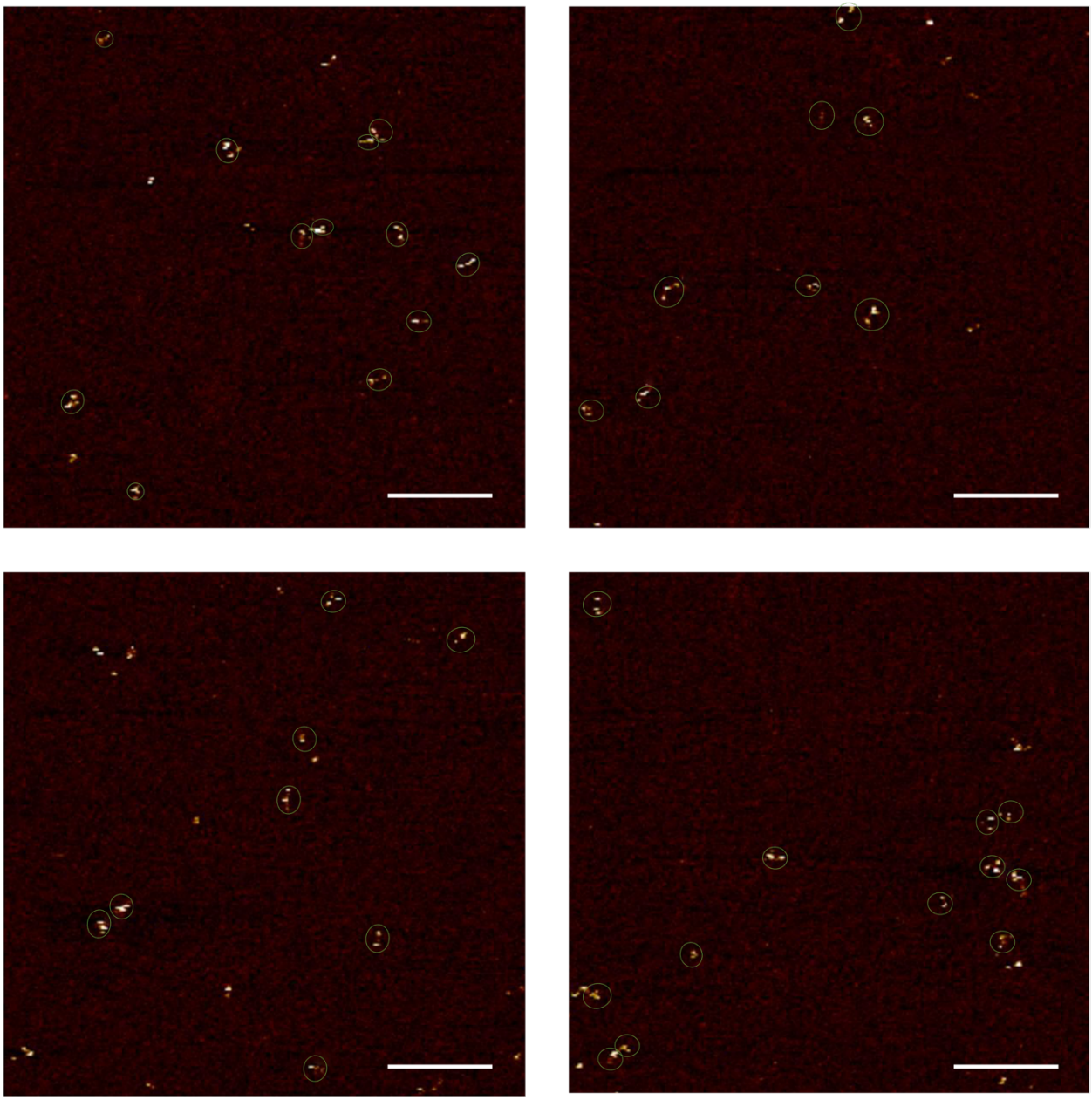

Figure S9. Wide-field AFM images of recovered linear trimer. Linear trimers are in green circles. Scale bars: 200nm

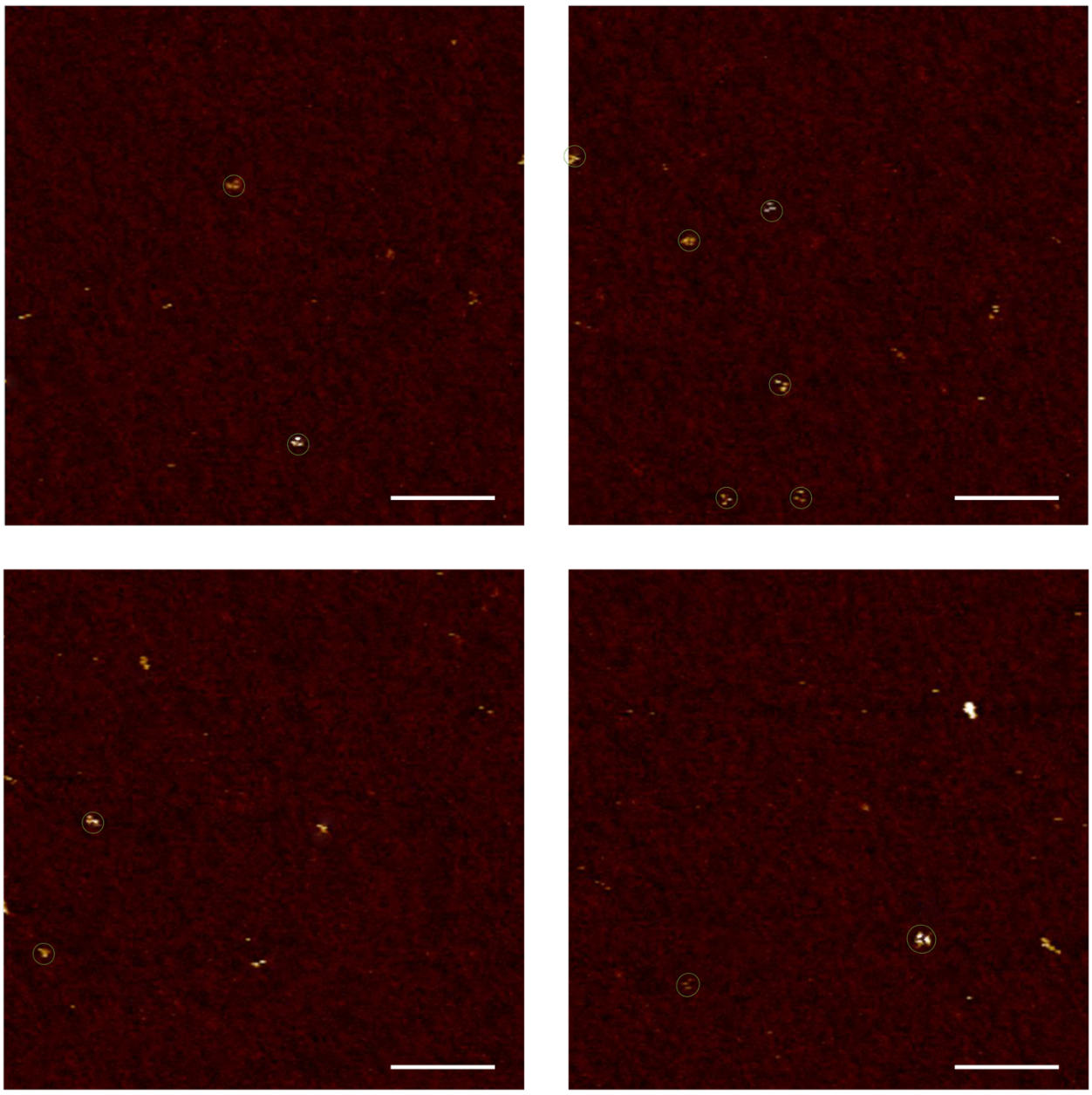

Figure S10. Wide-field AFM images of recovered Triangle. Triangles are in green circles. Scale bars: 200nm

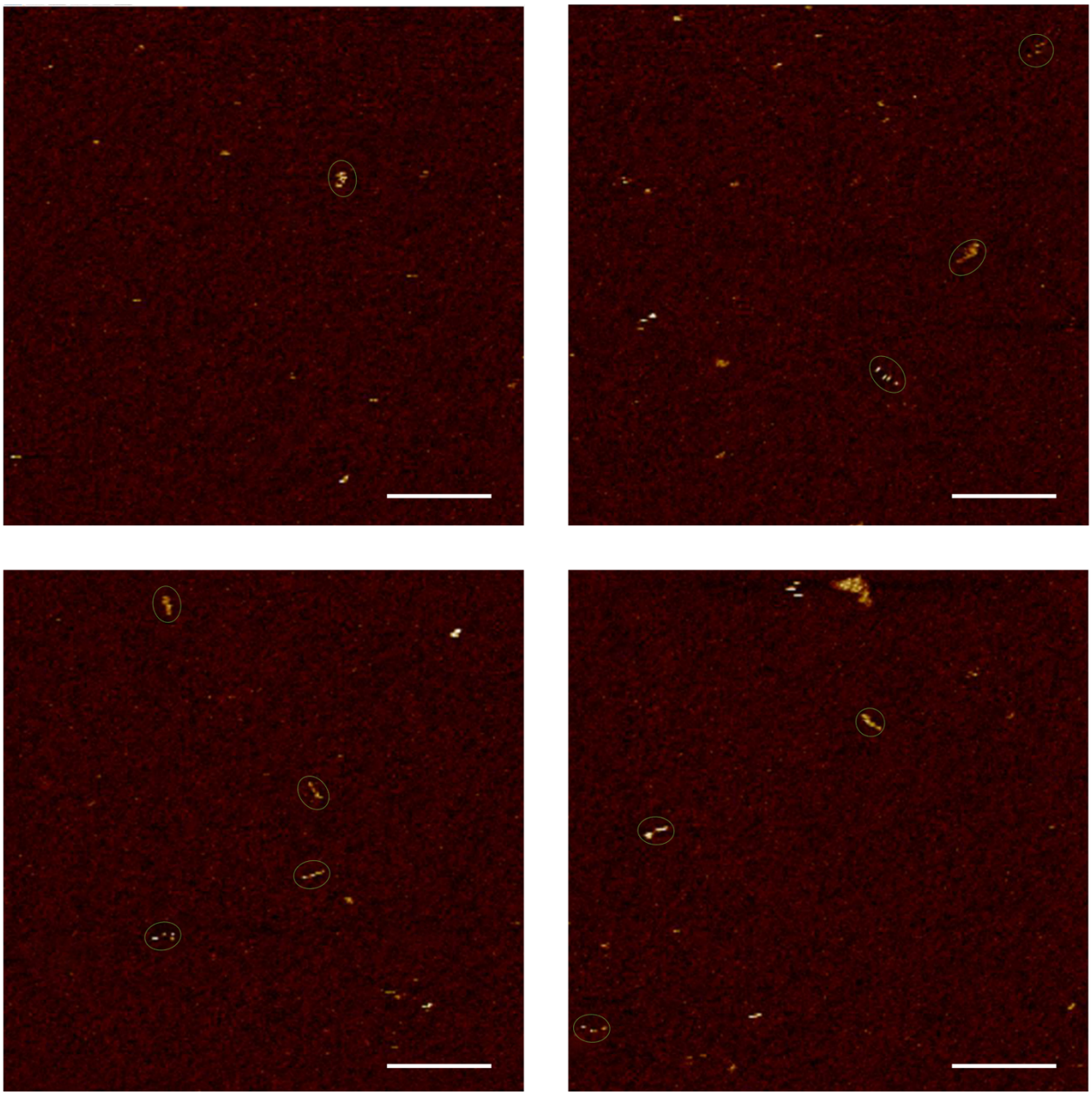

Figure S11. Wide-field AFM images of recovered linear tetramer. Linear tetramers are in green circles. Scale bars: 200nm

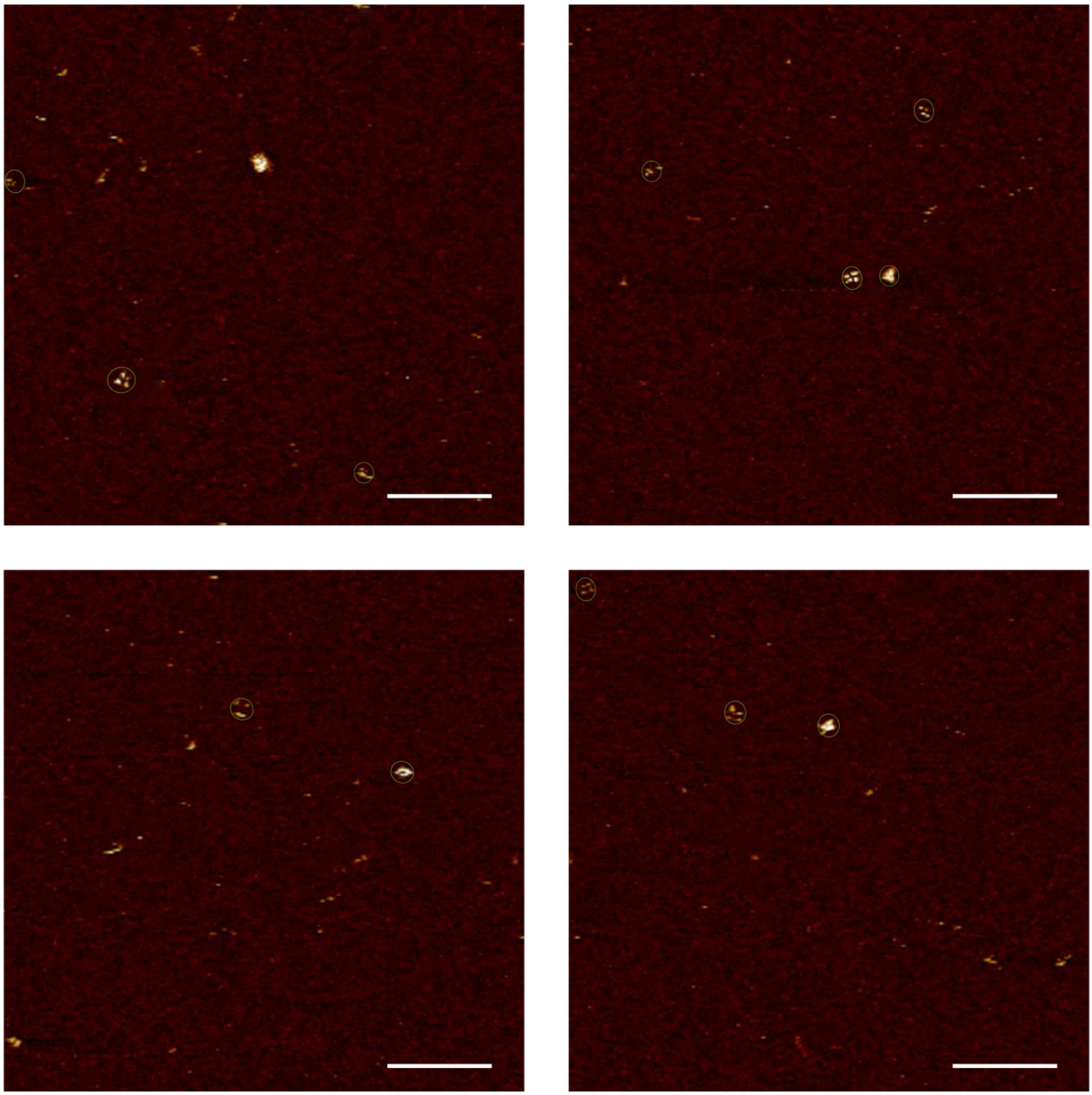

Figure S12. Wide-field AFM images of recovered Square. Squares are in green circles. Scale bars: 200nm

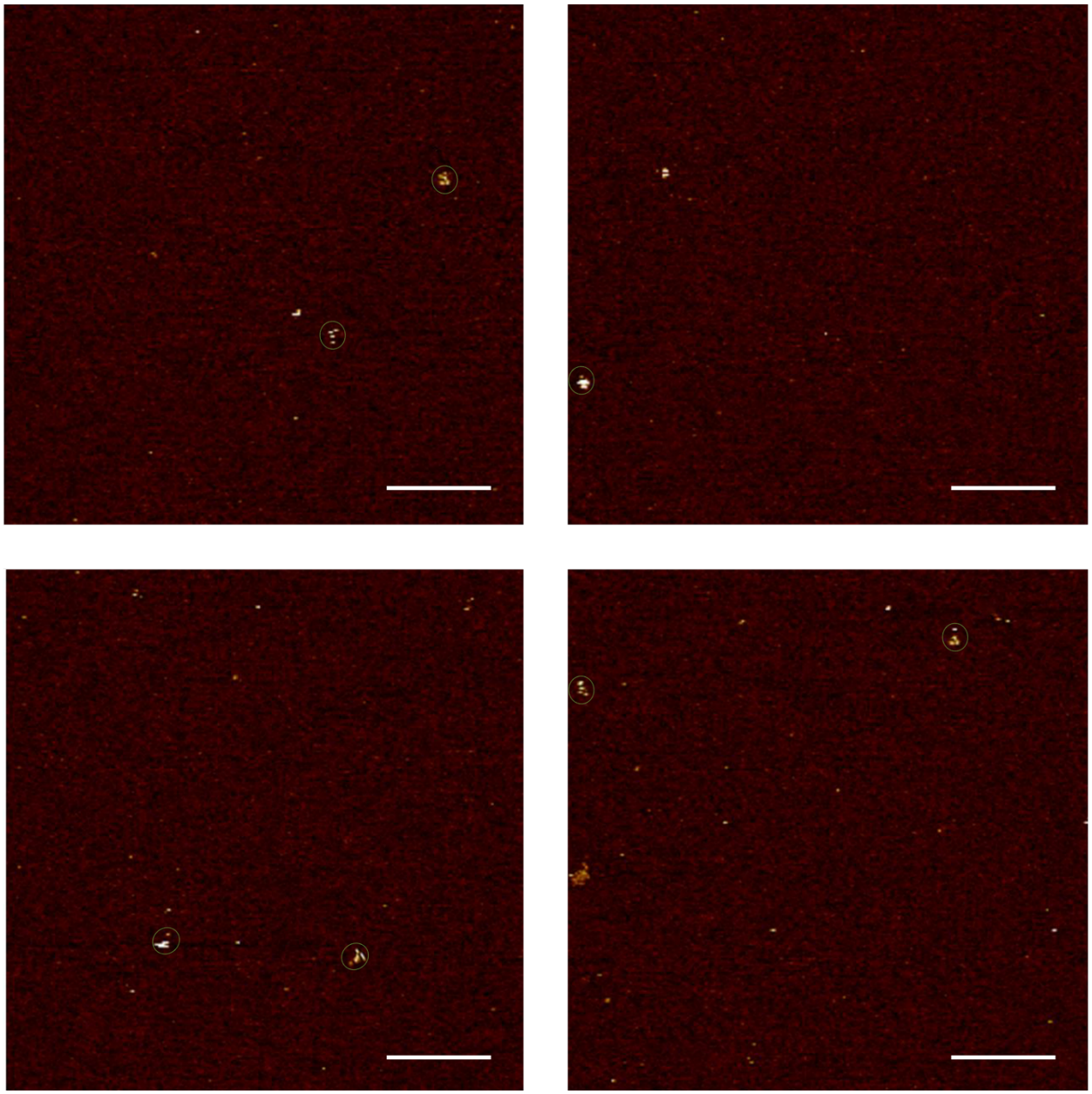

Figure S13. Wide-field AFM images of recovered shape Y. Shape Y are in green circles. Scale bars: 200nm

Table S5. Multimer yield calculation

Yield (%)	Image 1	Image 2	Image 3	Image 4	Average	Standard deviation
Dimer	84.5	81	86.7	83.1	84.4	2.77
Linear trimer	75	77.4	82.8	76.6	77.9	3.36
Triangle	56.3	57.7	33.3	31.6	44.7	14.2
Linear tetramer	19	46.2	64	50	44.8	18.8
Square	28.6	43.2	22.8	46.2	35.2	11.3
Shape Y	38.1	33.3	34.8	26.7	33.2	4.81

1.5.7 Distance between alds calculation

The distance between proteins was measured from center to center. Theoretically, the distance should be DNA length + protein dimension, which is 21nm. However, the DNA between proteins is not continues but has two kinks. Thus, most of the actual distances are shorter than we hypothesized. For some proteins hard to see spaces between others, we treated them as protein aggregates instead of products connected by DNA. Thus, we measured the protein distances in AFM images from Section S6 manually and calculated the average distances for each product. There is a manual measurement error, and we only take these distances to be integers. The actual distances are from 12nm to 22nm.

Table S6. Average distance between proteins in all ald multimers

	Dimer	Linear trimer	Triangle	Linear tetramer	Square	Shape Y	All shapes
Distances counted	132	80	36	33	48	28	357
Average distance (nm)	17.31	17.36	17.36	16.67	17.35	17.8	17.31

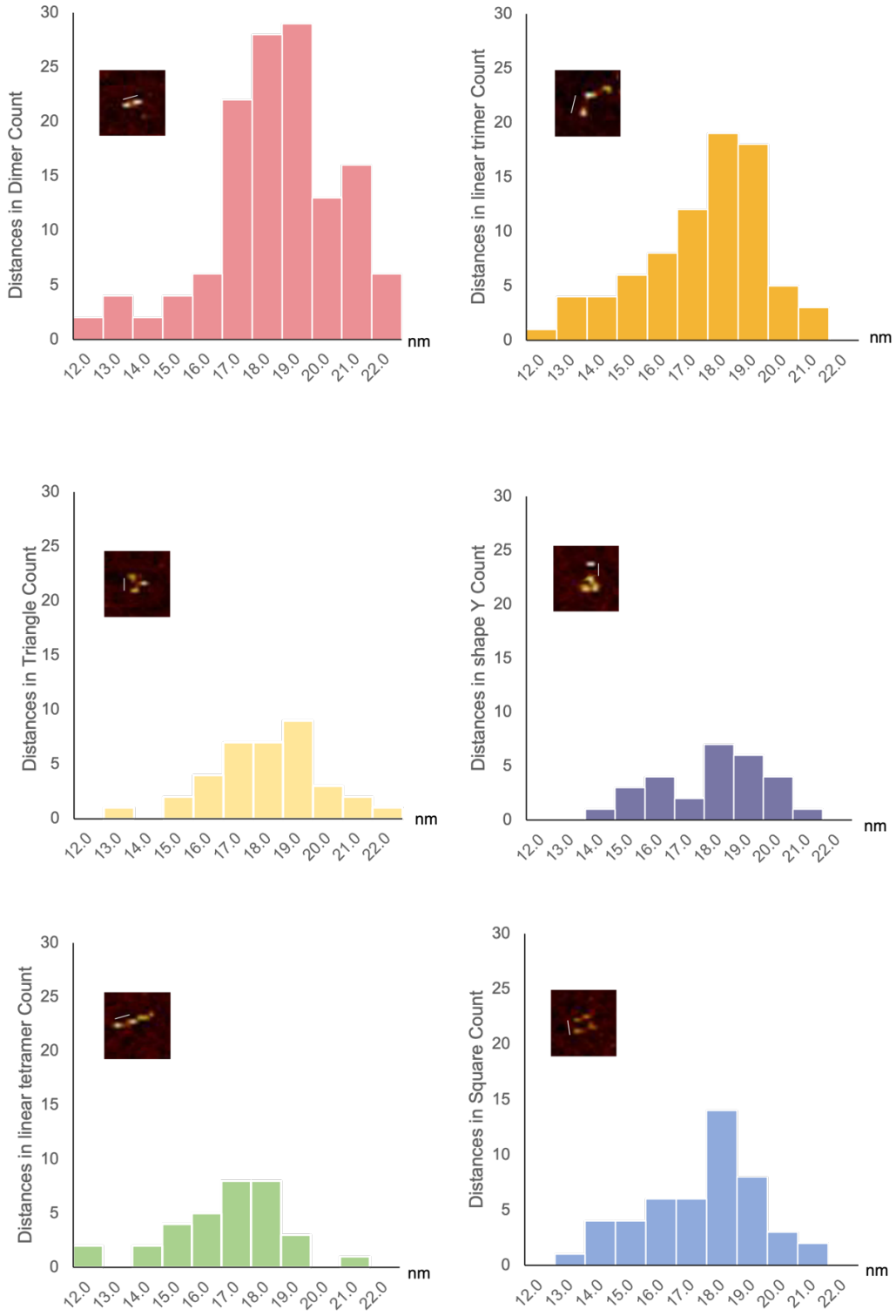

Figure S14. Count the number of distances (from 12nm to 22nm) between alds in ald dimer (Figure S7), linear trimer (Figure S8), Triangle (Figure S9), linear tetramer (Figure S10), Square (Figure S11), shape Y (Figure S12).

1.5.8 Pathway of linear tetramer formed in only one connection step

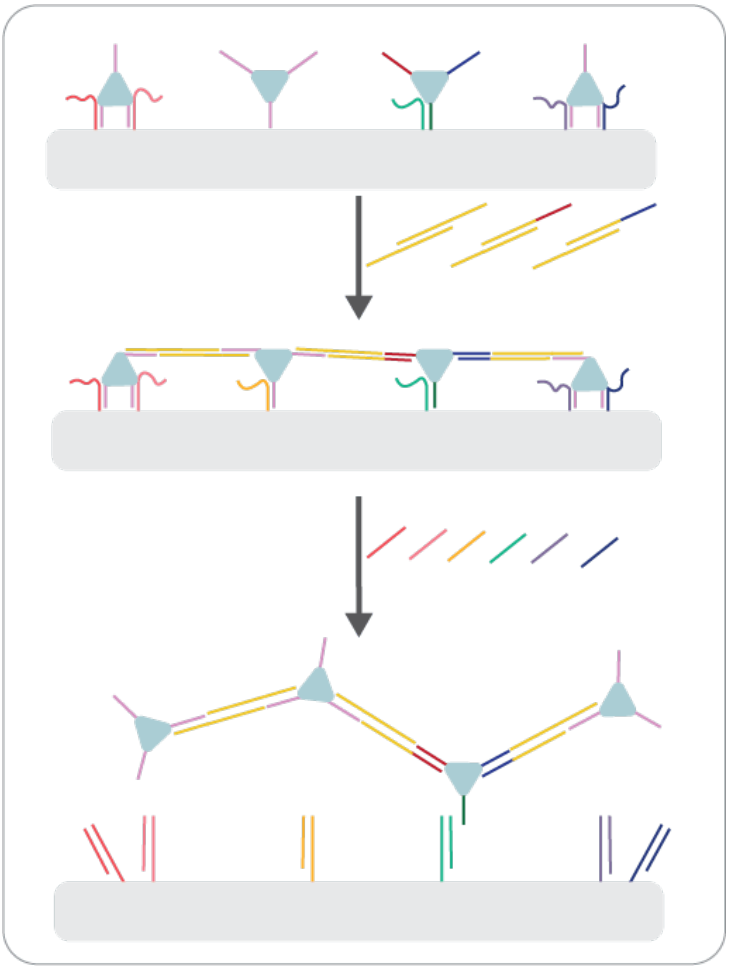

Figure S15. Pathway of linear tetramer formed in only one connection step. Ald c has three different ssDNA and one of them was attached to the origami. Three different connectors are added to the ald-4HB and connect four ald in one step.

1.6 References

1. Gotti, C.; Sensini, A.; Zucchelli, A.; Carloni, R.; Focarete, M. L., Hierarchical fibrous structures for muscle-inspired soft-actuators: A review. *Applied Materials Today* **2020,** *20*, 100772.

2. Guo, W.; Tian, Y.; Jiang, L., Asymmetric Ion Transport through Ion-Channel-Mimetic Solid-State Nanopores. *Accounts of Chemical Research* **2013,** *46* (12), 2834-2846.

3. Qu, J.; Cao, S.; Wei, Q.; Zhang, H.; Wang, R.; Kang, W.; Ma, T.; Zhang, L.; Liu, T.; Wing-Ngor Au, S.; Sun, F.; Xia, J., Synthetic Multienzyme Complexes, Catalytic Nanomachineries for Cascade Biosynthesis In Vivo. *ACS Nano* **2019,** *13* (9), 9895-9906.

4. Luo, Q.; Hou, C.; Bai, Y.; Wang, R.; Liu, J., Protein Assembly: Versatile Approaches to Construct Highly Ordered Nanostructures. *Chemical Reviews* **2016,** *116* (22), 13571-13632.

5. Wilson, C. J.; Bommarius, A. S.; Champion, J. A.; Chernoff, Y. O.; Lynn, D. G.; Paravastu, A. K.; Liang, C.; Hsieh, M.-C.; Heemstra, J. M., Biomolecular Assemblies: Moving from Observation to Predictive Design. *Chemical Reviews* **2018,** *118* (24), 11519-11574.

6. Dobson, C. M., Protein folding and misfolding. *Nature* **2003,** *426* (6968), 884-890.

7. Marsh, J. A.; Hernández, H.; Hall, Z.; Ahnert, S. E.; Perica, T.; Robinson, C. V.; Teichmann, S. A., Protein complexes are under evolutionary selection to assemble via ordered pathways. *Cell* **2013,** *153* (2), 461-70.

8. Jones, S.; Thornton, J. M., Principles of protein-protein interactions. *Proceedings of the National Academy of Sciences* **1996,** *93* (1), 13-20.

9. Westermarck, J.; Ivaska, J.; Corthals, G. L., Identification of protein interactions involved in cellular signaling. *Mol Cell Proteomics* **2013,** *12* (7), 1752-63.

10. Luscombe, N. M.; Austin, S. E.; Berman, H. M.; Thornton, J. M., An overview of the structures of protein-DNA complexes. *Genome Biology* **2000,** *1* (1), reviews001.1.

11. Kalodimos, C. G.; Biris, N.; Bonvin, A. M. J. J.; Levandoski, M. M.; Guennuegues, M.; Boelens, R.; Kaptein, R., Structure and Flexibility Adaptation in Nonspecific and Specific Protein-DNA Complexes. *Science* **2004,** *305* (5682), 386-389.

12. Dickey, T. H.; Altschuler, S. E.; Wuttke, D. S., Single-stranded DNA-binding proteins: multiple domains for multiple functions. *Structure* **2013,** *21* (7), 1074-84.

13. McMillan, J. R.; Mirkin, C. A., DNA-Functionalized, Bivalent Proteins. *Journal of the American Chemical Society* **2018,** *140* (22), 6776-6779.

14. McMillan, J. R.; Hayes, O. G.; Winegar, P. H.; Mirkin, C. A., Protein Materials Engineering with DNA. *Acc Chem Res* **2019,** *52* (7), 1939-1948.

15. Winegar, P. H.; Hayes, O. G.; McMillan, J. R.; Figg, C. A.; Focia, P. J.; Mirkin, C. A., DNA-Directed Protein Packing within Single Crystals. *Chem* **2020,** *6* (4), 1007-1017.

16. Partridge, B. E.; Winegar, P. H.; Han, Z.; Mirkin, C. A., Redefining Protein Interfaces within Protein Single Crystals with DNA. *J Am Chem Soc* **2021,** *143* (23), 8925-8934.

17. Mavridis, I. M.; Hatada, M. H.; Tulinsky, A.; Lebioda, L., Structure of 2-keto-3-deoxy-6-phosphogluconate aldolase at 2 . 8 A resolution. *J Mol Biol* **1982,** *162* (2), 419-44.

18. Fullerton, S. W.; Griffiths, J. S.; Merkel, A. B.; Cheriyan, M.; Wymer, N. J.; Hutchins, M. J.; Fierke, C. A.; Toone, E. J.; Naismith, J. H., Mechanism of the Class I KDPG aldolase. *Bioorg Med Chem* **2006,** *14* (9), 3002-10.

19. Xu, Y.; Jiang, S.; Simmons, C. R.; Narayanan, R. P.; Zhang, F.; Aziz, A. M.; Yan, H.; Stephanopoulos, N., Tunable Nanoscale Cages from Self-Assembling DNA and Protein Building Blocks. *ACS Nano* **2019,** *13* (3), 3545-3554.

20. Nafisi, P. M.; Aksel, T.; Douglas, S. M., Construction of a novel phagemid to produce custom DNA origami scaffolds. *Synthetic Biology* **2018,** *3* (1).

21. Poppleton, E.; Romero, R.; Mallya, A.; Rovigatti, L.; Sulc, P., OxDNA.org: a public webserver for coarse-grained simulations of DNA and RNA nanostructures. *Nucleic Acids Res* **2021,** *49* (W1), W491-W498.

Chapter 2. Programmable site-specific functionalization of DNA origami with polynucleotide brushes

Adapted from Yunqi Yang#, Qinyi Lu#, Dr. Chao-Min Huang, Hongji Qian, Yunlong Zhang, Dr. Sonal Deshpande, Prof. Dr. Gaurav Arya, Prof. Dr. Yonggang Ke, Prof. Dr. Stefan Zauscher. *Angew. Chemie.,* **2021** 60(43) Adapted with permission.

2.1.Abstract

Combining surface-initiated, TdT (terminal deoxynucleotidyl transferase) catalyzed enzymatic polymerization (SI-TcEP) with precisely engineered DNA origami nanostructures (DONs) presents an innovative pathway for the generation of stable, polynucleotide brush-functionalized origami nanostructures. We demonstrate that SI-TcEP can site-specifically pattern DONs with brushes containing both natural and non-natural nucleotides. The brush functionalization can be precisely controlled in terms of the location of initiation sites on the origami core and the brush height and composition. Coarse-grained simulations predict the conformation of the brush-functionalized DONs that agree well with the experimentally observed morphologies. We find that polynucleotide brush-functionalization increases the nuclease resistance of DONs significantly, and that this stability can be spatially programmed through the site-specific growth of polynucleotide brushes. The ability to site-specifically decorate DONs with brushes of natural and non-natural nucleotides provides access to a large range of functionalized DON architectures that would allow for further supramolecular assembly, and for potential applications in smart nanoscale delivery systems.

2.2 Introduction

Over the last two decades, research in DNA nanotechnology has seen astonishing growth and has yielded exquisite DNA-based nanostructures that span a broad range of sizes and complexity.[1] DNA origami nanostructures (DONs) have been widely investigated for biomedical applications,

such as biosensing,[2] *in-vivo* imaging,[3] and drug and gene delivery,[4] due to their inherent biocompatibility, exquisite control over nanoscale geometry, mechanical properties, and suitability for site-specific functionalization.[5] However, the utility of DONs in biological environments is often compromised by their instability under denaturation conditions and damage by nuclease digestion.[6] These are particularly important factors that need to be considered for drug delivery applications where DONs have been investigated as nanoparticle-based delivery platforms to overcome the drawbacks of traditional small-molecule therapeutics (*e.g.,* poor solubility, quick excretion by the renal system, and biodegradation).[7] A strategy to mitigate instability issues is to "coat" DONs with functional groups that shield the origami core from the biological environment. To this end, a variety of approaches have been developed to cover DONs with lipid bilayers,[8] proteins,[9] peptides,[10] polymers,[11] and peptoids.[12] In most of these approaches, the adsorption of the protecting moieties is driven by hydrophobicity or electrostatic interactions between positively charged molecules and the negatively charged DONs. While these protection methods improve the overall stability of DONs under specific conditions, the non-covalent binding between the protecting moieties and the DON surface can still be easily disrupted by mechanical forces and changes in the surrounding environment. Moreover, current methods are unable to produce tunable and site-specific functionalization of DONs with (bio)polymeric brush layers, which is crucial for taking full advantage of the inherent programmability of DONs for biomedical and other emerging applications. To the best of our knowledge, only one study has so far reported the formation of nanopatterned synthetic polymers on the surface of DNA origami by *in-situ*, atom-transfer radical polymerization, though the average height of these polymers is only ~1 nm, which is insufficient for the protection of the DNA origami cores.[13]

Recently, we developed a new biomimetic method—TdT (terminal deoxynucleotidyl transferase) catalyzed enzymatic polymerization (TcEP)—to synthesize high molecular weight (MW), single-stranded DNA (ssDNA) homo- and block-co-polynucleotides with low polydispersity.[14] TcEP uses the template-independent polymerase TdT to sequentially add 3'-deoxyribonucleoside 5'-triphosphates (dNTPs) to an oligonucleotide primer.[15] We showed that TdT can polymerize both natural and non-natural nucleotides into single-stranded DNA (ssDNA),[16] which enables the introduction of various functionalities into polynucleotide chains, including clickable groups, fluorescent dyes, hydrophobic groups, and cytotoxic moieties.

Here, we report on the design, synthesis, and characterization of stable and adaptive polynucleotide-functionalized DNA origami nanostructures (pn-DONs) through the synergistic combination of surface-initiated polynucleotide brush synthesis using TcEP with precisely engineered DNA origami.[17] Importantly, we show that these structures can be readily designed using existing origami design tools and their morphologies accurately predicted using coarse-grained molecular dynamics simulations. Our experimental results show that we have precise control over not only the shape of the origami core, but also the location, height, and functional composition (natural *vs.* non-natural nucleotides) of the polynucleotide brush. Furthermore, we show that pn-DONs have significantly higher nuclease resistance compared to unprotected DNA origami, and that this stability can be spatially programmed by site-specific design of the TcEP initiation sites on the surface of DONs. The resulting adaptive pn-DON degradation could be harnessed for DNA-based drug delivery vehicles to facilitate cellular uptake.

2.3 Results and Discussion

Our approach for creating pn-DONs is summarized in **Figure 1**. From the vast array of possible 3D DNA nanostructures, we choose rod-shaped 16-helix bundle (16HB) and 6-helix bundle (6HB) origami because of their simple geometry and the ease with which their lengths and widths can be tuned (**Figures 1A** and **S1–S4**). The DNA nanorods were assembled by mixing and annealing the scaffold DNA strands with staple DNA strands in buffer solutions (see **Methods**). A 16HB origami nanorod (130 nm long, 10 nm wide, square cross-section) has 144 evenly distributed staple 3' ends on its surface, whereas a 6HB origami nanorod (400 nm long, 6 nm wide, hexagon cross-section) has 162 staple 3' ends on its surface. By using selected staple strands with 3'-oligo(dT) overhangs, TdT catalyzed enzymatic polymerization can be programmed to site-specifically initiate DNA brush growth on the surface of DNA origami nanorods (**Figures 1B** and **S2**). Since the monomer to initiator (M/I) concentration ratio determines the degree of polymerization,[14b] we are able to synthesize a uniform polynucleotide brush layer onto the 3'-overhang-modified regions of the nanorods (**Figure 1C**). For brevity, we term the oligo(dT) modified DONs as 16HB-S^{a}_{b} or 6HB-S^{a}_{b}, where *a* specifies the number of modified surfaces and *b* specifies the fraction of a surface that is modified. Furthermore, we term the polynucleotide functionalized DONs as 16HB-S^{a}_{b}-pn_{c} or 6HB-S^{a}_{b}-pn_{c}, where *c* reflects the expected number of bases in the poly(dT) brush.

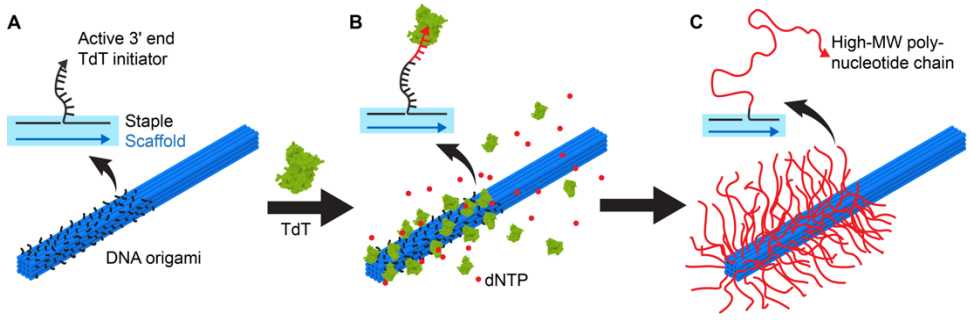

Figure 1. Schematic showing the programmable initiation of polynucleotide brush growth by surface-initiated TdT-catalyzed enzymatic polymerization (SI-TcEP). (A) DNA origami partially modified with 3' oligo(dT) initiators on the surface. **(B)** Polynucleotide brush growth by SI-TcEP using TdT. **(C)** DNA origami site-specifically modified with polynucleotide brushes on the surface after SI-TcEP reaction.

For a typical SI-TcEP reaction, we mixed DONs, dTTP, and TdT together in the TdT reaction buffer and incubated the mixture at 37℃ overnight. The resulting pn-DONs were purified by centrifugal filtration and characterized by agarose gel electrophoresis, and, after deposition onto a mica surface, by tapping mode atomic force microscopy (AFM) in air. To control the molecular weight (height) of the DNA brush modification, we systematically varied the feed ratio (M/I) of monomer (*i.e.*, dTTP) to initiator (*i.e.,* oligo(dT) extensions on the surface of DONs) on the fully decorated 16HB (16HB-$S^4_{1/1}$).[14b] Gel electrophoresis showed that the degree of polymerization increased with increasing M/I (**Figures 2A** and **S5A**). AFM imaging showed that fully decorated DONs were covered with a dense polynucleotide brush corona (**Figures 2B** and **S6)**. The brush height estimated from AFM image analysis increased almost linearly with M/I ratio, *i.e.*, brush MW (**Figure S5B**). We also studied the effect of SI-TcEP reaction time (2 h, 6 h, 24 h) on polynucleotide brush growth at a constant M/I = 500. Our results suggest that the surface-initiated polymerization reaction is fast, approaching completion already after 2 hours (**Figure S7**).

To elucidate details of the polynucleotide brush conformation on the surface of DONs we carried out oxDNA coarse-grained molecular dynamics simulations[18] of the structures in solution and after deposition onto a surface (**Figures 2D**, **S8**–**S11**). The simulations reveal that pn-DONs are stable over the entire time of the simulation (>150 μs), and that the polynucleotide chains adopt

a moderately stretched conformation in solution, likely due to their relatively high surface grafting density (distance between chain initiation sites << chain size) and weak electrostatic repulsion between their negatively charged backbones. The brush segment density plotted as function of distance r from the origami surface suggests that the chains exhibit classic cylindrical brush behavior, with the segment density decaying as $\sim r^{-0.65}$ (**Figure S10**).[19] Chain stretching increases when the structures are confined in 2D to mimic the surface-adsorbed state visualized by AFM (**Figure S11**). The predicted brush heights of the surface-confined structures agree remarkably well with those obtained from analyses of AFM images (compare yellow and green bars in **Figure 2C**). This agreement suggests that the predicted brush heights in solution (blue bars in **Figure 2C**) should then likely provide a reasonable estimate of the "true" height of the brush on the origami surface.

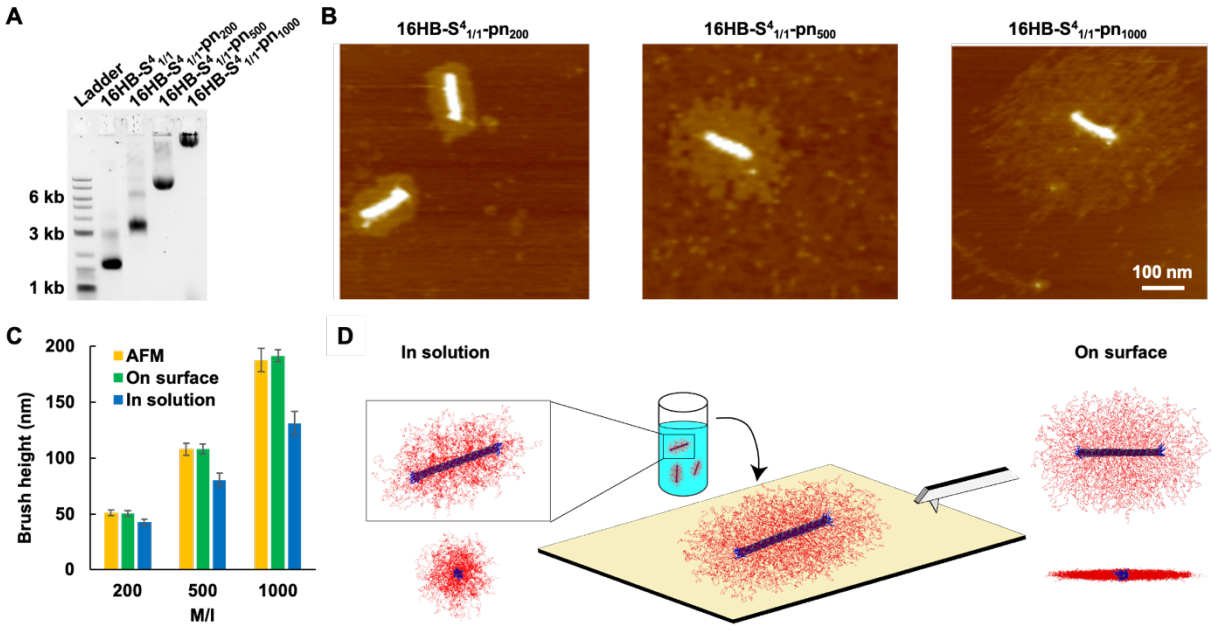

Figure 2. Formation of 16HB pn-DONs with controllable brush height. (A) Agarose gel image and **(B)** AFM images showing the controllable length of poly(dT) corona on 16HB-$S^4_{1/1}$ with different feed ratios (M/I = 200, 500, and 1000). **(C)** Bar graph comparing the brush heights of 16HB-$S^4_{1/1}$-pn_{200}, 16HB-$S^4_{1/1}$-pn_{500}, and 16HB-$S^4_{1/1}$-pn_{1000} obtained from AFM image analysis with those predicted by 2D (on surface) and 3D (in solution) oxDNA simulations. **(D)** Simulation results of 16HB-$S^4_{1/1}$-pn_{500} (top and side view) showing the morphology difference between structures in solution and on surface.

We show next that site-specific polynucleotide brush growth can be achieved by designing DONs with oligo initiator extensions only at specific locations on the DON surface. The gel image in **Figure 3A** shows the change in MW after SI-TcEP of three DONs with different patterns of initiation sites (16HB-$S^1_{1/1}$, 16HB-$S^4_{1/2}$, and 16HB-$S^4_{1/1}$). Before SI-TcEP, the mobility of DONs on the gel is quite similar, likely because the MW differences due to the different number of oligo(dT) extensions (8 nt) on the DON surfaces are small. After SI-TcEP (M/I = 500), however, the resulting pn-DONs have distinctly different MWs due to the different number of poly(dT) chains emanating from the surfaces. For example, for the 16HB-$S^1_{1/1}$-pn_{500}, the poly(dT) brush exists only on one DON surface (**Figure S2**). However, due to the random orientation of pn-DONs on the mica surface during drop casting, the AFM image is unable to properly show this single surface modification effect clearly (**Figure 3B**). Nevertheless, compared to the 16HB-$S^4_{1/1}$-pn_{500}, the brush density on 16HB-$S^1_{1/1}$ is visibly much lower. The AFM image of the half-decorated DONs (16HB-$S^4_{1/2}$-pn500) shows a brush emanating from one half of the length of the origami core and extending to the other, undecorated half (**Figure 3B**). We attribute this effect to the flattening and spreading of the polynucleotide chains on the mica surface after drop-casting and drying. This behavior is also predicted by our simulations of pn-DONs on surfaces (**Figure 3C**).

Additional demonstrations of spatial programmability using 16HB-$S^4_{1/3}$ and 16HB-$S^4_{1/6}$ systems are shown in **Figure S12**.

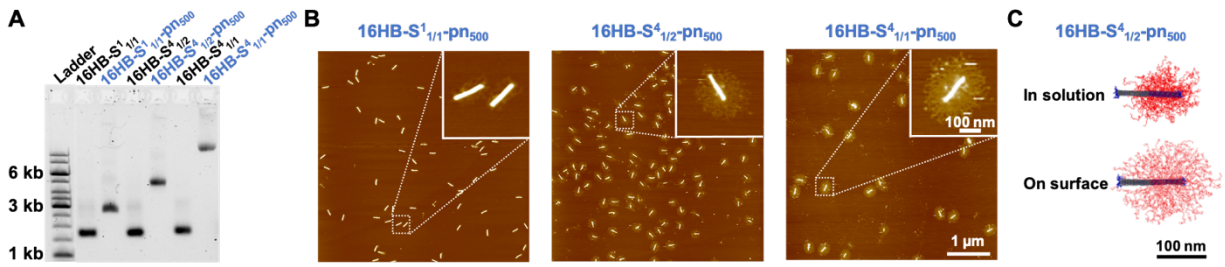

Figure 3. Site-specific modification of 16HBs with polynucleotide brushes. (A) Agarose gel electrophoresis image and **(B)** AFM images showing site-specific initiation of polynucleotide brush growth (M/I = 500) on 16HB. 16HB-$S^1_{1/1}$: 16HB with full-decorated poly(dT) extensions on 1 side (36 extensions); 16HB-$S^4_{1/2}$: 16HB with half-decorated poly(dT) extensions on all 4 sides (72 extensions); 16HB-$S^4_{1/1}$: 16HB with full-decorated poly(dT) extensions on all 4 sides (144 extensions). **(C)** oxDNA simulation of 16HB-$S^4_{1/2}$-pn_{500} in solution and on surface.

We verified the spatial programmability of brush growth using an entirely different DON core design, *i.e.*, the 6HB, which is much longer and thinner compared to the 16HB (**Figure 4**). We first designed and assembled 6HB origami with oligo(dT) initiation sites at different positions along the origami core (6HB-$S^6_{1/1}$, 6HB-$S^6_{13/27}$, 6HB-$S^6_{5/27+5/27}$, and 6HB-$S^6_{7/27}$), and then subjected the resulting DONs to SI-TcEP (M/I ratio = 500). **Figure 4B** shows excellent agreement between the pn-DON conformations predicted by our simulations and those observed in AFM images. Because 6HBs are significantly longer than 16HBs, one can distinguish pn-DONs with poly(dT) brush corona at different positions on 6HBs more clearly.

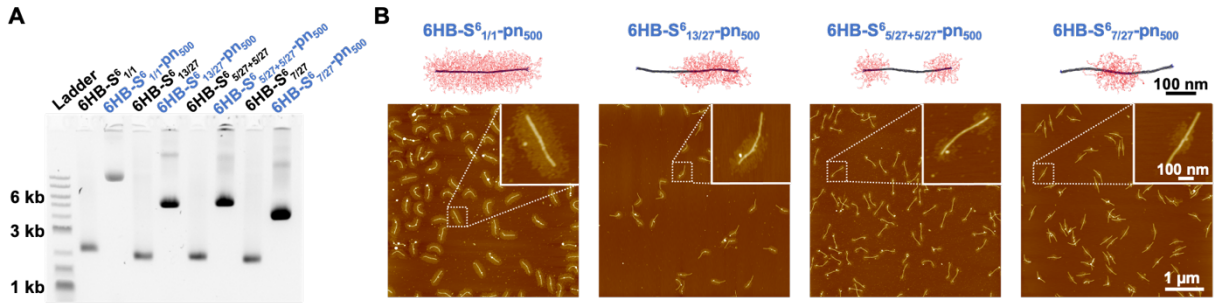

Figure 4. Site-specific modification of 6HBs with polynucleotide brushes. (A) Agarose gel electrophoresis image and **(B)** 2D (on surface) simulation results and AFM images showing site-specific initiation of polynucleotide brush growth (M/I = 500) on 6HB. 6HB-$S^6_{1/1}$: 6HB with full-decorated poly(dT) extensions (162 extensions); 6HB-$S^6_{13/27}$: 6HB with half-decorated poly(dT) extensions on one end (78 extensions); 6HB-$S^6_{5/27+5/27}$: 6HB with partial poly(dT) extensions on both ends (60 extensions); 6HB-$S^6_{7/27}$: 6HB with partial poly(dT) extensions in the middle (42 extensions).

It is known that a dense oligonucleotide brush layer is more resistant to nuclease degradation.[20] This also holds true for pn-DONs, as shown by our results in **Figure 5**. Specifically, we compared the stability of 16HB and 16HB-$S^4_{1/1}$-pn_{500} when subjected to digestion by the endonuclease DNase I. The gel and AFM images both confirm that fully covered 16HB-$S^4_{1/1}$-pn_{500} pn-DONs are significantly more stable against degradation by DNase I at physiological concentration (3.6 U/mL)[21] compared to the bare 16HBs at the same mass concentration (compare **Figure 5A** with **5B**). We attribute the downward movement of bands for 16HB-$S^4_{1/1}$-pn_{500} to the partial degradation of the polynucleotide brushes, which protect the origami cores; furthermore, we attribute the background noise appearing in the AFM images of pn-DONs to residual TdT enzymes remaining in solution after TcEP reaction.

In addition to DNase I, we also investigated the stability of the brush-protected origami against 10% FBS (16HB-$S^4_{1/1}$-pn_{250} and 16HB-$S^4_{1/1}$-pn_{500}). **Figure S13** shows that the brush height (*i.e.,* M/I) affects the degradation kinetics substantially. While both pn-DONs show distinct bands in the gel even after 20 hours of incubation, degradation proceeds slower for the origami decorated with longer brushes, as seen by the higher intensity of bands for 16HB-$S^4_{1/1}$-pn_{500} in **Figure S13C** compared to the bands for 16HB-$S^4_{1/1}$-pn_{250} in **Figure S13B**. The upward movement of bands for pn-DONs after incubation with 10% FBS is likely due to the interaction of proteins in FBS with the pn-DONs, leading to a different mobility when subjected to an electric field. This behavior is different from that observed when incubated with DNase I (**Figure 5A**).

Lastly, we evaluated the stability of 6HB pn-DONs against DNase I degradation. The gel and AFM images showed that unlike the 16HB pn-DONs, the 6HB DONs and pn-DONs were almost completely degraded already after incubation for 1 h (**Figure S14**). These results are consistent with the lower grafting density of polynucleotide brushes on 6HB cores and the smaller width of 6HB cores compared to 16HB cores (**Figures S2–S4**). Nevertheless, AFM images show that brush-modified 6HB pn-DONs are still more stable than unmodified ones. This is consistent with the agarose gel image which shows a distinct band for pn-DONs even after 30 min, while DONs lacking a brush layer form a smear in the first 10 min (**Figure S14**).

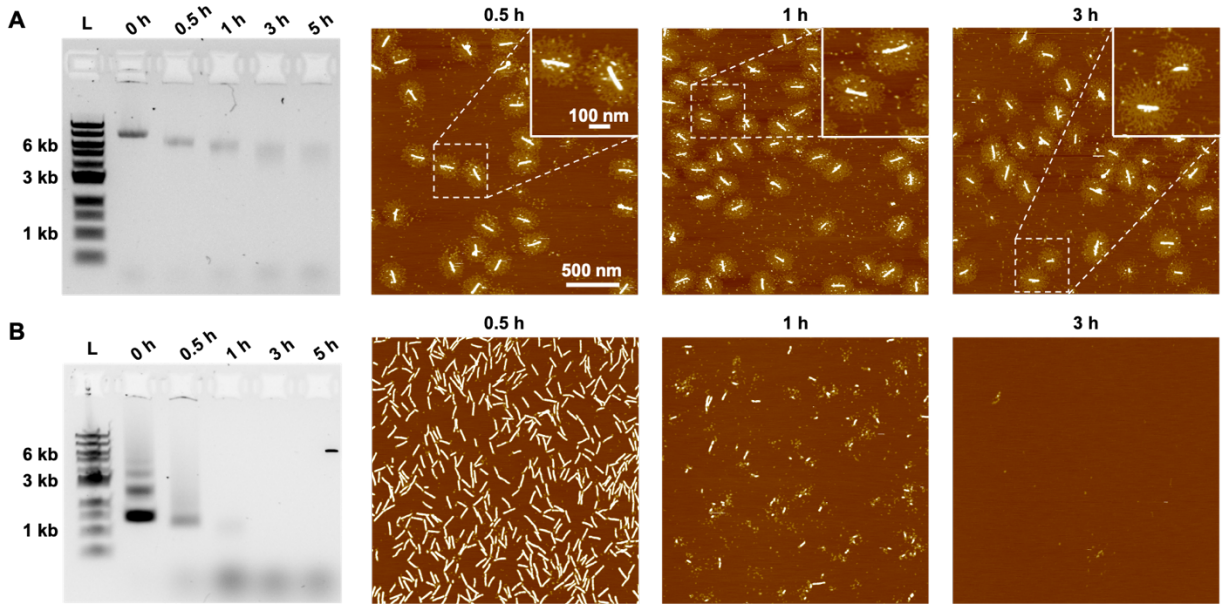

Figure 5. Nuclease stability of 16HB DONs with and without polynucleotide brushes. Agarose gel electrophoresis image and AFM images showing the stability of DNA origami (A) with (16HB-$S^4_{1/1}$-pn_{500}) and **(B)** without (16HB-$S^4_{1/1}$) poly(dT) brush decoration after incubation with 3.6 U/mL DNase I for different lengths of time.

Interestingly, the location for enzymatic attack on pn-DONs can be programmed by origami design. For example, after incubating the half-decorated 16HB (16HB-$S^4_{1/2}$-pn_{500}) with DNase I for 1 h, only the polynucleotide-covered segments of the origami core survive (**Figures 6B**, **S15**, and **S16**), as depicted schematically also in **Figure 6A**. By analyzing the areas of pn-DONs and the areas of their origami cores as a function of time from AFM images, we observed a peak shift in both cases, indicating that the brush corona acts as a sacrificial layer for the brush-protected segment of the origami core (**Figures 6D**, **S15B**, and **S15C)**. Thus, by deliberately introducing TcEP initiation sites on DONs, we can *a priori* determine which segments of origami will be degraded. This is an important attribute of our structures that has implications for drug delivery through the design of cleavable DONs.[22]

This phenomenon of selective protection is more apparent in the context of longer 6HB origami. We incubated dumbbell-shaped 6HBs (6HB-$S^{6}_{5/27+5/27}$-pn_{500}) which were decorated with a poly(dT) brush corona at both ends of the nanorods with DNase I (0.5 U/mL). AFM images showed that the dumbbell-shaped pn-DONs were cleaved in the center region of the nanorod which has no poly(dT) brush modification, as indicated with arrows in **Figure 6G**. However, the resulting shorter segments of brush-modified origami survived for a significantly longer time in presence of DNase I. This is also apparent from the gel image (**Figure 6F**), which shows that in addition to the band at the higher MW position (corresponding to the original sample), another band at the lower MW position (corresponding to the protected segments of the origami core) appeared after 30 min, and thereafter only the band with the lower MW survived after 60 min.

Finally, we studied the stability of protected and unprotected origami in physiologically relevant buffer conditions. This is important because DONs are typically only stable at sufficiently high concentrations of divalent cations (*e.g.,* 10 mM Mg^{2+} for 16HB and 6HB), which far exceed those in physiological conditions. AFM images showed that after incubating DONs (16HB) and pn-DONs (16HB-$S^{4}_{1/1}$-pn_{200} and 16HB-$S^{4}_{1/1}$-pn_{500}) in 1X DPBS with only 0.9 mM Ca^{2+} and 0.5 mM Mg^{2+} for 24 hours, both DONs and pn-DONs with short brushes (M/I = 200) disassembled (**Figures S17D** and **S17E**). However, pn-DONs with long polynucleotide brushes (M/I = 500) maintained their integrity even after 24 hours incubation (**Figure S17F**). This was corroborated by gel images of DONs and pn-DONs with shorter brushes (M/I = 200) (**Figures S17A** and **S17B**), which showed a larger extent of staple dissociation—as seen by the increase of band intensity at lower positions (<500 bp)—than pn-DONs with longer brushes. The observed upward shift in the

bands for 16HB samples after incubation arises from the disassembly of origami, which results in increased size and thus slower migration in the agarose gel. On the other hand, the downward shift in the bands for both pn-DON samples (16HB-$S^{4}_{1/1}$-pn_{200} and 16HB-$S^{4}_{1/1}$-pn_{500}) suggests a loss of poly(dT) strands during disassembly, which leads to overall lower MW but still fully intact pn-DON structures which migrate faster in the agarose gel.

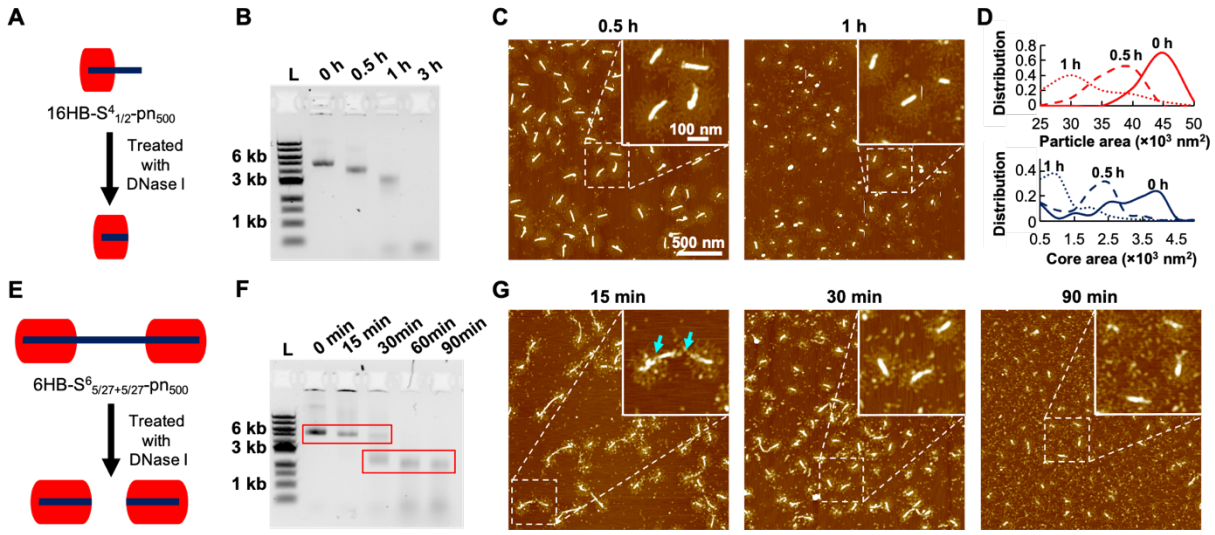

Figure 6. Controllable partial digestion of pn-DONs. (A) Schematic, **(B)** agarose gel electrophoresis image, **(C)** AFM images, and **(D)** size distribution of pn-DON particles and their origami cores showing the process of partial digestion of 16HB-$S^{4}_{1/2}$-pn_{500} by 3.6 U/mL DNase I. **(E)** Schematic, **(F)** agarose gel electrophoresis image, and **(G)** AFM images showing the process of partial digestion of 6HB-$S^{6}_{5/27+5/27}$-pn_{500} by 0.5 U/mL DNase I.

So far, as proof-of-concept, we have used natural nucleotide (dTTP) monomers for the polymerization reactions. However, as shown in **Figure S18**, we confirmed that TdT is able to polymerize 5-Fluoro-dUTP (5F-dUTP), a non-natural cytostatic nucleotide. This observation underscores the potential of pn-DONs for drug-delivery applications. Our approach can be applied even more broadly to also encompass chemically functionalized nucleotide analogues that could be harnessed for post-polymerization reactions, such as azide-alkyne cycloaddition "click" reactions. To this end, we showed that 5-Ethynyl-dUTP (5E-dUTP) and 5-(3-Aminoallyl)-dUTP (aa-dUTP) can be polymerized by SI-TcEP (**Figures S18** and **S19**). Specifically, we obtained pn-DONs with random co-polynucleotide brushes of dTTP (80%) and aa-dUTP (20%), and showed that the amine groups in the brushes can react with sulfo-Cy5 NHS to give Cy5 signals in the gel (**Figure S19**). Therefore, by introducing clickable groups into polynucleotide brushes, our approach can be used for generating a broad range of site-specific chemical modifications on DNA origami, including incorporation of dyes, hydrophobic groups, and biotin.

2.4 Conclusion

In summary, our research on the synergistic combination of surface initiated enzymatic polynucleotide brush synthesis with precisely engineered DNA origami is new and presents, guided by molecular simulations, an innovative pathway for the generation of tunable, stable polynucleotide brush-functionalized origami nano- and meso-structures. Specifically, we have devised a strategy that harnesses the broad polymerization capability of TdT to synthesize DNA nanostructures by site-specifically programming the surface-initiated growth of polynucleotide brushes on the surface of DNA origami. We found that fully brush-decorated pn-DONs can be stable for many hours in presence of nucleases and physiologically relevant buffer conditions. We showed that site-specific, partial brush decoration will direct nuclease

degradation primarily to unprotected areas of the origami core, thus providing a route to generate smart, cleavable pn-DONs. Finally, the ability of TdT to polymerize a broad range of nucleotide analogues enables the synthesis of a broad range of polynucleotide brush-modified DNA origami which are poised to find applications ranging from drug delivery and biosensing to the generation of microreactors by supramolecular self-assembly.

2.5 Acknowledgements

S.Z. thanks the NIH for support through grant R21 EB026590-03. Y.K. Acknowledges the support of DOE grant DE-SC0020996, and NSF grants DMR-1654485 and ECCS-1807568. G.A. also acknowledges the support of DOE grant DE-SC0020996. Computational resources were provided by the Duke Computing Cluster (DCC) and the Extreme Science and Engineering Discovery Environment (XSEDE) Program supported by NSF grant ACI-1053575.

Y.Y. and Q.L. contributed equally to this work.

2.6 Keywords

surface-initiated polymerization, molecular dynamics simulations, nuclease resistance, DNA nanotechnology, drug delivery

2.7 Materials and Methods

2.7.1 Materials

All DNA strands, including scaffold p7560 (used in 16HB), p7308 (used in 6HB) and staple strands, were purchased from Integrated DNA Technologies. dTTP, HCl, 5 M NaOH, SYBR Safe DNA Gel Stain, and GeneRuler 1kb DNA ladderwere ordered from Thermo Fisher Scientific. 5' F-dUTP and 5' Ethynyl-dUTP were purchased from Jena Biosciences. Terminal deoxynucleotidyl transferase (TdT) was ordered from Promega (one unit of TdT corresponds to approximately 0.46 μM). 2.5 mM CoCl2 solution, 10X TdT reaction buffer, PEG8000, 20X TE buffer, Quick-Load Purple 1 kb DNA Ladder, and DNase I were bought from New England Biolabs. Magnesium acetate, sodium chloride, Trizma, 10X tris- borate EDTA buffer (pH 8.3), 10X DPBS (with Mg^{2+} and Ca^{2+}), 10X PBS, Ethidium Bromide, nuclease-free water, and 0.5 mL Microcon Centrifugal Filter Units were purchased from Millipore Sigma. SeaKem Gold Agarose was purchasedfrom Lonza. Freeze 'N Squeeze DNA Gel Extraction Spin Columns were bought from Bio-Rad. AFM TappingMode™ silicon cantilevers (kf = 40 N/m, freq = 311-357 kHz, RTip < 10 nm) were ordered from Bruker. Uranyl formate powder and CF400-CU EM grids were purchased from Electron Microscopy Sciences. 0.2 μm syringe filters were bought fromVWR International.

2.7.2 DNA Origami Preparation, modification and Characterization

Design, Synthesis, and Characterization of DNA Origami: DNA origami nanorods were designed with caDNAno[1] software and computer codes written by the Ke lab. We employed modeling and simulation software tools (*i.e.,* oxDNA,[2] and CanDo[3]) to predict the 3D shapes, conformational properties, and the stability of our nanorod design. Simulationswere

used to eliminate nanorod designs with obvious shape distortion and high degree of internal stress. After satisfactory designs of nanorods were identified, we generated the staple DNA sequences by using either caDNAno orin-house computer codes. For the DNA nanorod assembly we followed established experimental protocols.[4] Notably, we also added 8 dTTP to the 3' ends of certain sets of staple strands to generate 3' oligo(dT) overhangs, serving as site-specific initiation sites on the surface of DNA nanorods. Before annealing, scaffold strand and staple strands weremixed in 200 μL tubes in annealing buffer (50 mM Tris, 10 mM Mg^{2+}, pH adjusted to 8.0 using HCl). The final concentration of scaffold strands and individual staple strands were 30 nM and 150 nM, respectively. Then the tube wasplaced in a thermocycler (S1000 Thermal Cycler, Bio-Rad) and the sample underwent the following annealing process:

Step 1: Hold at 85 ℃ for 10 min.

Step 2: Lower to 60 ℃ and then decrease to 25 ℃ in increments of

1 ℃ every 30 min.

Step 3: Hold at 20 ℃ until further use.

Unless specifically indicated, this annealing process was used for all samples. After assembly, the DNA nanorods weresubjected to careful characterization by agarose gel electrophoresis, TEM, and tapping mode AFM, to verify nanorod yield and morphology. Subsequently, we purified the DNA nanorods by PEG precipitation or agarose gel purification into 1X TdT reaction buffer (50 mM potassium acetate, 20 mM tris-acetate, 10 mM magnesium acetate, pH=7.9). The dimensions (width and length) of DNA nanorods were analyzed from TEM images using ImageJ. To this end we selected20 nanorods from the image of each sample set and calculated their average dimensions to confirm the correctly folded structure of the DNA origami.

PEG Precipitation: Unpurified DNA samples were mixed with Precipitation Buffer (15%

PEG8000, 1X TE, 505 mM NaCl, 10 mM MgCl2) at a 1:1 ratio. The mixture was centrifuged at 16,000 rcf for 20-25 minutes under 4 ℃. The supernatant was then removed and the pellet was resuspended in 1X TdT reaction buffer. Finally, the concentration of a sample was measured using a spectrophotometer (Nanodrop 1000, Thermo Scientific).

We used this purification method for unmodified DNA origami only.

Agarose Gel Purification: Samples were characterized and/or purified with a 0.75% agarose gel in 0.5X TBE with 10mM Mg^{2+} as the running buffer (45 mM Tris, 45 mM boric acid, 1 mM EDTA, and 10 mM Mg^{2+}, pH=8.0) for 90 min at 60V and at 4 ℃. Gels were pre-stained with 1X Ethidium Bromide or SYBR Safe DNA Gel Stain for visualization. We imaged the gels using a Bio-Rad Gel Doc EZ Imager. Corresponding DNA bands were cut using a razor blade, put in Freeze 'N Squeeze DNA Gel Extraction Spin Columns, and kept at -20 ℃ for 30 min. The columns were then centrifugedat 13,000 rcf for 3 min, and the flow through of each column was collected. Gel purified samples were buffer-exchanged into 1X TdT reaction buffer before TcEP reactions using 30 kD Microcon Centrifugal Filters or by PEG precipitation. The concentration of the recovered samples was measured using a spectrophotometer (Nanodrop 1000, Thermo Scientific).

Gel purification could effectively remove the enzymes (*i.e.* TdT) in solution, but the yield of gel recovery was generally lower (<30%), limiting the amount of materials we could use for subsequent reactions (*e.g.,* DNase I assays). Therefore,we used this purification method for the observation of pn-DON structures only, when no subsequent reactions were needed.

Centrifugal Filtration: We used 30 kD Microcon Centrifugal Filter Units (Millipore) to remove unreacted monomers from the SI-TcEP reaction products. Typically, we centrifuged

the units at ~4,000 rcf for 15 min for three times before recovery. Centrifugal filtration could not remove the enzymes, as observed in the background of some AFM images. However, because of the higher yield of this method, we used it when subsequent reactions were needed (*e.g.,* DNase I assays)for economic reasons.

Transmission Electron Microscopy (TEM) Imaging: 20-30 ng sample solutions were deposited onto charged, carbonfilm-coated copper EM grids and incubated for 30 s after which excess solvent was blotted and removed with filter paper.8 μL 1% uranyl formate (UF) solution was used for negative staining and excess liquid was blotted and removed with filter paper after 20 s incubation time. We imaged the samples using a Hitachi HT-7700 120 kV Tungsten TEM with AMTCCD camera. We note that i) the number of nanostructures shown in the TEM images does not represent the actual yield, and that ii) the brightness of the figures solely depends on the staining and imaging technique. To prepare the 1%UF solution, we dissolved 10 mg UF powder in 1 mL DI water and heated to the point at which only insoluble sediments remained at the bottom. We then added 1 μL of 5 M NaOH to the solution, mixed the solution well, and filtered the mixture through a 0.2 μm syringe filter with a cellulose acetate membrane. Finally, we collected the filtrate. We chargedthe copper EM grids using a Pelco easiGlow Glow Discharge Cleaning System.

Surface-Initiated Enzymatic Synthesis of Homopolynucleotide Brushes: *Homopolynucleotide brushes* (*e.g.*, poly(dTTP), poly(5F-dUTP), and poly(5' Ethynyl-dUTP)) were synthesized by surface-initiated TdT-catalyzed enzymaticpolymerization (SI-TcEP) using different M:I ratios to obtain different brush lengths (*i.e.,* MWs).[5] The initiator

concentration (*i.e.*, the number of staples with 3' oligo(dT) overhangs on the origami surface) in these reactions was determined by the concentration of origami multiplied by the number of overhangs per origami. The reaction mixtures contained 1 U/μL TdT in 1X TdT reaction buffer and different concentrations of dTTP monomers, while holding the initiator concentration constant at 0.5 μM oligo(dT).[6] All the enzymatic polymerizations were carried out overnight at 37 ℃, and the reaction products were purified using Microcon Centrifugal Filter Units (Millipore) to remove unreacted monomers. To remove enzymes in solution, we used agarose gel purification method.

Characterization of DNA Brush-functionalized Origami: We used 0.75% agarose gel electrophoresis to characterize the change of molecular weight after SI-TcEP of polynucleotides.[7] Specifically, we ran the reaction products at 60 V for90 min at 4 ℃ in a refrigerator through a 0.75%-1% agarose gel in 0.5X TBE buffer supplemented with 10 mM Mg^{2+}. To characterize the morphology of the polynucleotide-functionalized origami, we placed a drop of solution with ~40 ng of the sample containing 10 mM MgCl2 onto a freshly cleaved mica surface. After 5 min incubation, we rinsed the substratewith Milli-Q H2O and dried the surface in a stream of N2. We then acquired TappingMode™ AFM images in ambient condition with a MultiMode AFM with Nanoscope V controller (Bruker), using TappingMode™ silicon cantilevers. The resulting images were analyzed using the NanoScope Analysis software package (Bruker) and ImageJ (NIH). We determined the average brush height from about 20 height measurements for each sample set (**Figure 2C**). To check for bias in the procedure, two persons carried out this analysis independently. Similar results were obtained.

Nuclease Degradation Assay: 16 HB origami samples (50 ng/uL) were incubated with 3.6 U/mL DNase I or 10% FBSbefore and after SI-TcEP reactions at 37 ℃ for different lengths of time (*e.g.,* 1 h, 3 h, 6 h, 24 h).[8] Different DNase I concentrations were used for 6HB, as indicated in the captions.[9] At each time point, 5 μL of the reaction mixture wasremoved and stored at -20 ℃. The aliquots collected from different time points were characterized using agarose gel electrophoresis and TappingMode™ AFM imaging. To determine the degradation, we measured the projected area of half-modified 16HB (16HB-$S^4$1/2-pn500) samples on AFM images using ImageJ. For each sample, we selected 40 data points to plot the size distribution profiles (**Figure 6D**). Furthermore, we determined the area of the origami core of half-modified 16HB (16HB-$S^4$1/2-pn500) on AFM images using NanoScope Analysis software by thresholding the height of thecore (**Figure 6D**). To check for bias in the procedure, two persons carried out these analyses independently. Similar results were obtained.

Magnesium Ion Depletion Assay: Origami samples (~100 ng/μL) before and after SI-TcEP reactions were transferredto 1X DPBS (containing 0.5 mM Mg^{2+} and 0.9 mM Ca^{2+}) by buffer exchange using the 30 kD Microcon Centrifugal Filter Units.[8] Next, the samples were incubated in 1X DPBS at 37 ℃ for different lengths of time (1 h, 4.5 h, 24 h). The aliquots collected from different time points were characterized using agarose gel electrophoresis and TappingMode™ AFM imaging.

2.7.3 Computational Section

***Coarse-grained MD Simulations*:** The caDNAno designs for the 16HB and 6HB cores were converted to oxDNA topology and configuration files using tacoxDNA.[10] An in-house MATLAB script was used for adding in the staple extensions and polynucleotide chains of desired lengths at locations stipulated by the desired brush pattern. We used non-overlapping, stretched-out, Hilbert curves for the initial configuration of the chains to facilitate their relaxation duringsimulation. The new resulting set of oxDNA topology and configuration files containing staple extensions and chains were then used for simulating the pn-DONs. The protocol for relaxing each structure was adapted from our previous study, where the structures were relaxed by replacing the DNA backbone potential with linear springs and gradually increasing their spring constants while applying mutual traps between paired scaffold and staple bases to avoid dissociations (~10^5 MD time steps on CPUs).[11] Then, a short MD simulation with mutual traps was conducted using theoxDNA2 force field for 10^6time steps. Following this, we performed another ~10^7time steps of MD simulation with no mutual traps (~2×10^8time steps for structures with chains longer than 200 nucleotides). Lastly, we conducted ~10^8time steps of MD simulation (production run), where configurations (trajectories) were collected for later analysis. We utilized a time step of 6.06 fs for all solution-state simulations and a timestep of 3.03 fs for all surface-deposited state simulations. Thus, the total length of the simulations was 606 ns and 303 ns, respectively, which corresponds to time scales of ~200 □s and ~100 □s accounting for the 330-fold mobility speed-up due to coarse graining.[12] All stages of thesimulations (except the relaxation step) used an Anderson-like thermostat to maintain the temperature at 30 ℃, a monovalent salt concentration of 0.5 M, and GPUs for acceleration. For comparing simulation results of brush width against AFM imaging, we applied external forces to the pn-DONs through judicious use of repulsion planes to confine the structures into a quasi-2D configuration. In particular, the repulsion planes were separated by 34 nm and their stiffness constants were set to 0.0103 pN/nm. Our previous study showed

that such confined origami structures yield better agreement with AFM images than those simulated in solution (**Figure S11**).

2.7.4 Supporting Figures

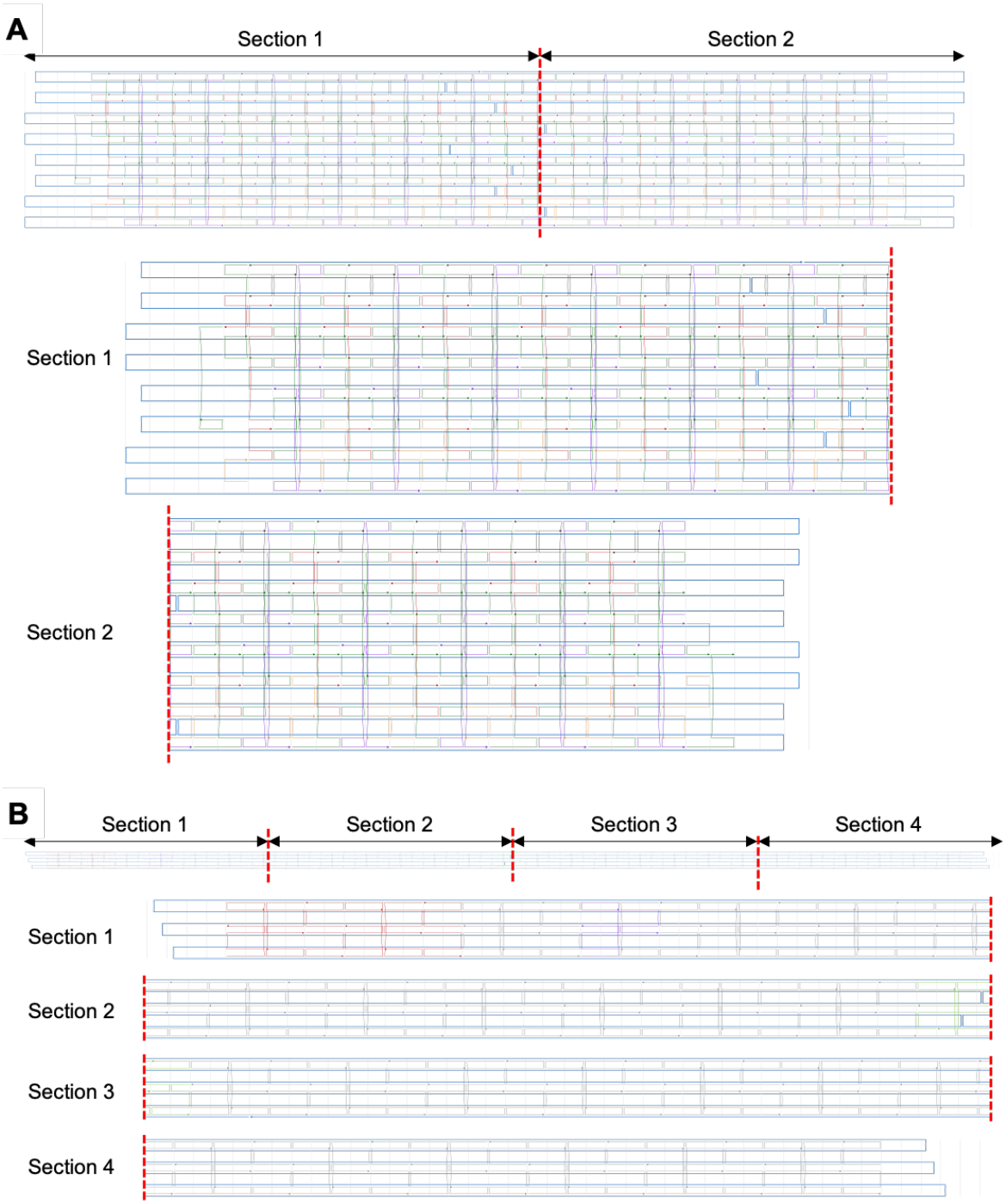

Figure S1. Design diagram of 16HB and 6HB using caDNAno. **(A)** 16HB design. **(B)** 6HB design. 3' ends on theoutside surface can be modified with oligo(dT)8 extensions.

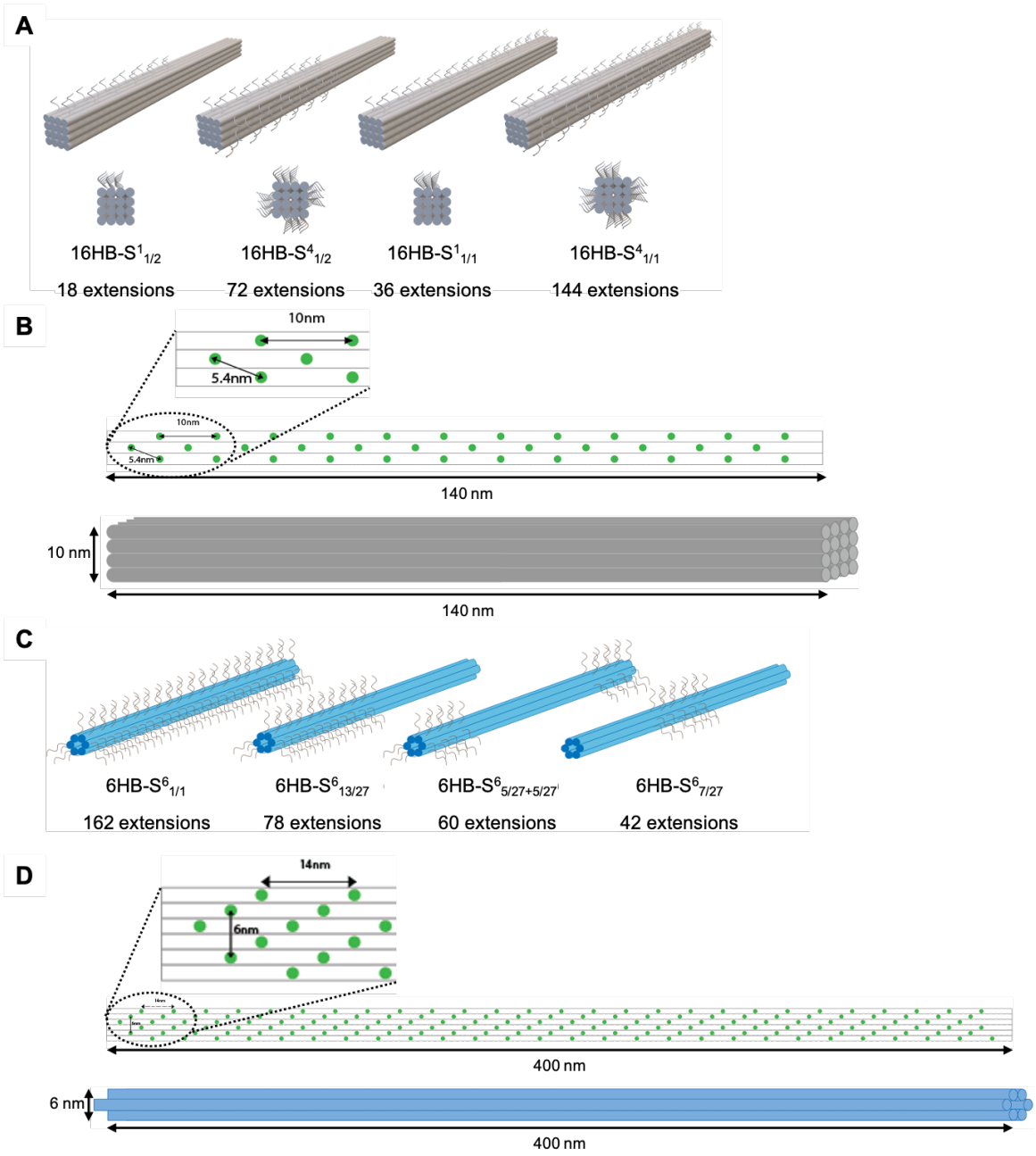

Figure S2. Locations of oligo(dT)8 extension sites and poly(dT) brushes on 16HB and 6HB.

(A) Poly(dT) brushes on 16HB, from left to right: 16HB-$S^1$1/2, 16HB-$S^4$1/2, 16HB-$S^1$1/1, and 16HB-$S^4$1/1. **(B)** Side view of one surface (top) and 3Dschematic (bottom) of 16HB. The length of the bundles is 140nm and the width is 10 nm. Oligo(dT)8 extension sites are represented with green dots, and the distances between them are labeled. **(C)** Poly(dT) brushes on 6HB, from left to right: 6HB-$S^6$1/1, 6HB-$S^6$13/27, 6HB-$S^6$5/27+5/27, and 6HB-$S^6$7/27. **(D)** Unfolded graph (top) and 3D schematic (bottom) of 6HB. The length of the bundles is 400nm and the width is 6 nm. Oligo(dT)8 extension sites are represented with green dots,and the distances between them are labeled.

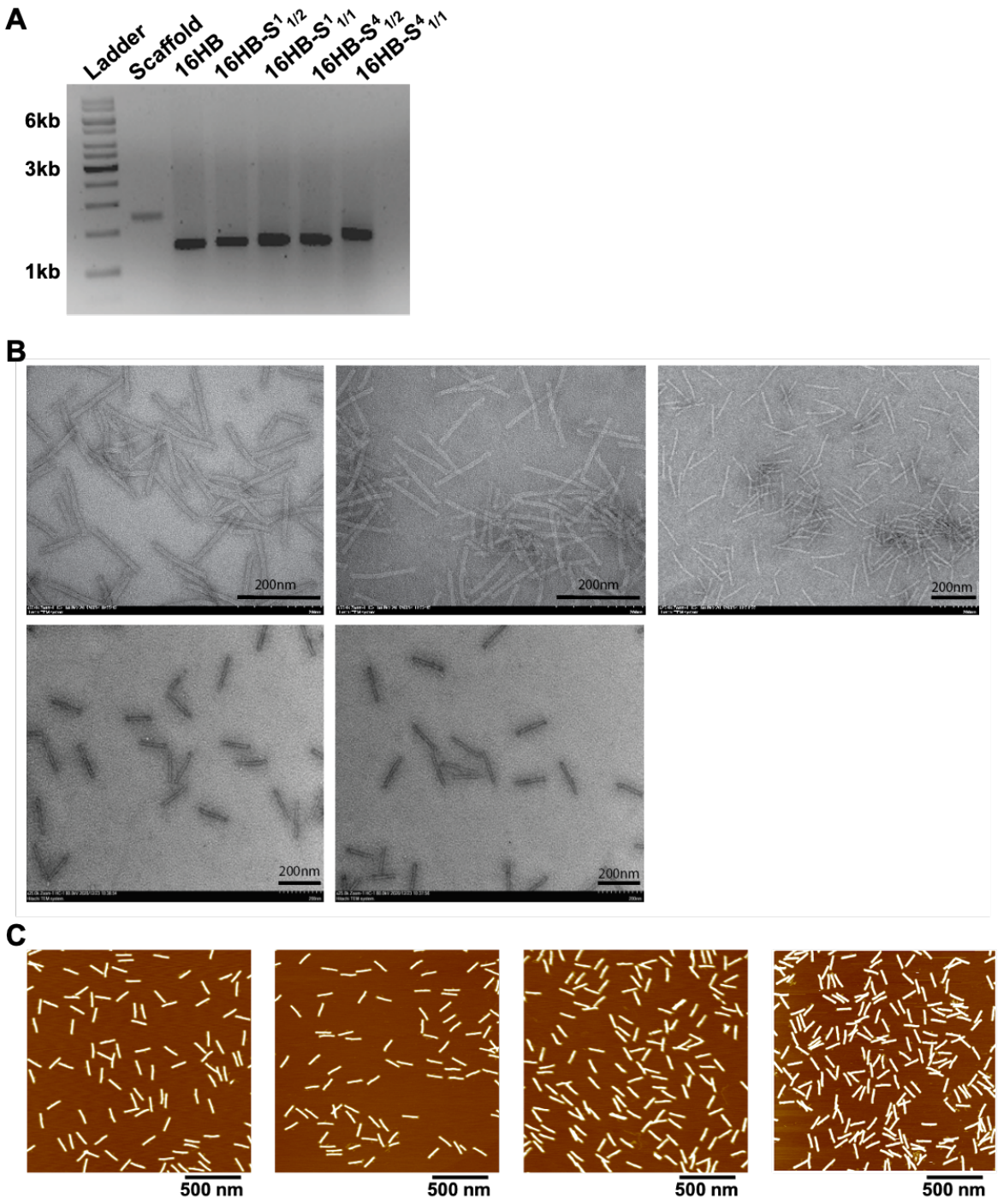

Figure S3. 16HB characterization. **(A)** Agarose gel image (Scaffold, 16HB, 16HB-S[1]1/2, 16HB-S[1]1/1, 16HB-S[4]1/2, and16HB-S[4]1/1). **(B)** TEM images (16HB, 16HB-S[1]1/2, 16HB-S[1]1/1, 16HB-S[4]1/2, and 16HB-S[4]1/1). **(C)** AFM images (16HB, 16HB-S[1]1/1, 16HB-S[4]1/2, and 16HB-S[4]1/1).

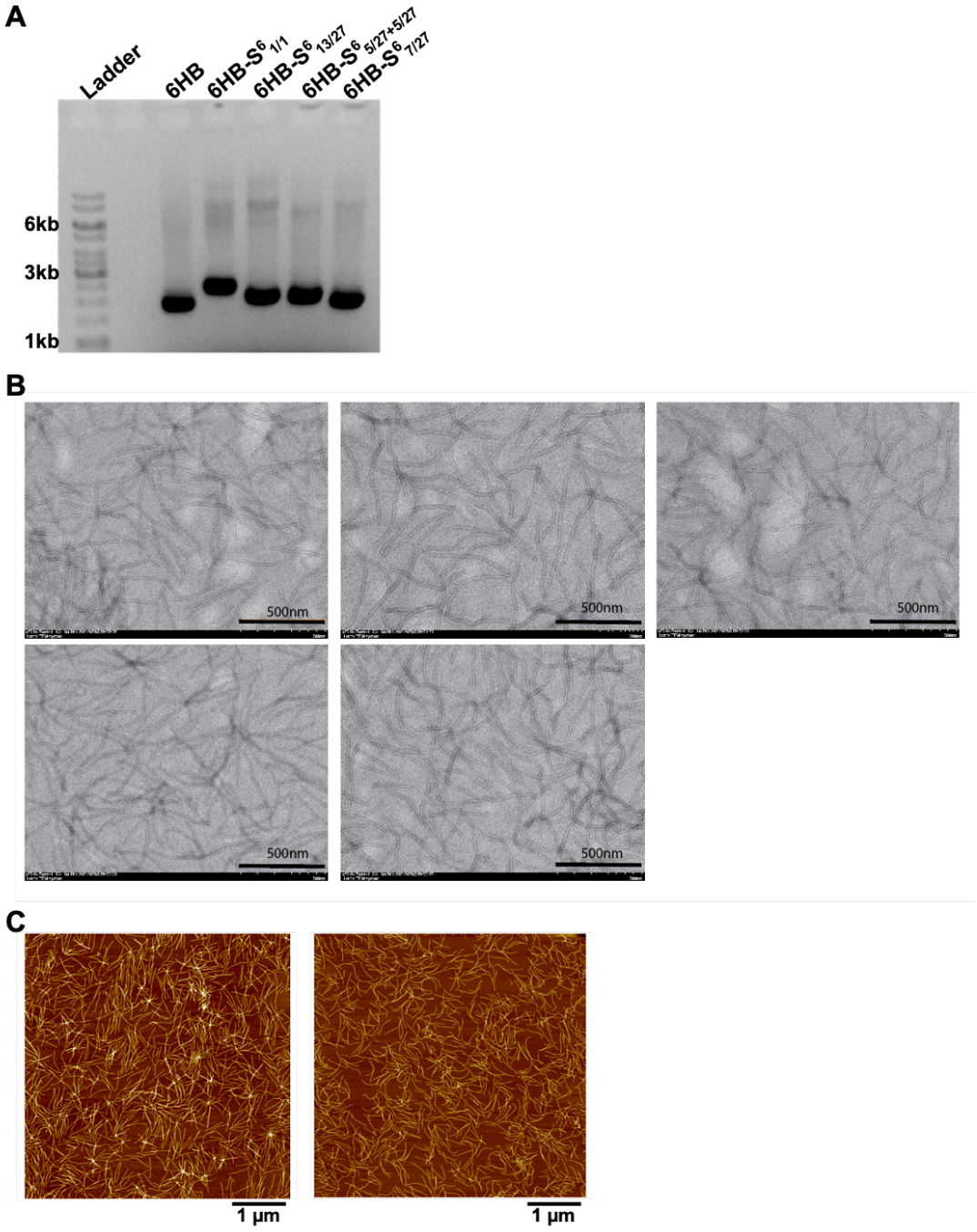

Figure S4. 6HB characterization. **(A)** Agarose gel image (6HB, 6HB-S^{6}1/1, 6HB-S^{6}13/27, 6HB-S^{6}5/27+5/27, and 6HB-S^{6}7/27). **(B)** TEM images (6HB, 6HB-S^{6}1/1, 6HB-S^{6}13/27, 6HB-S^{6}5/27+5/27, and 6HB-S^{6}7/27). **(C)** AFM images (6HB and 6HB-S^{6}1/1).

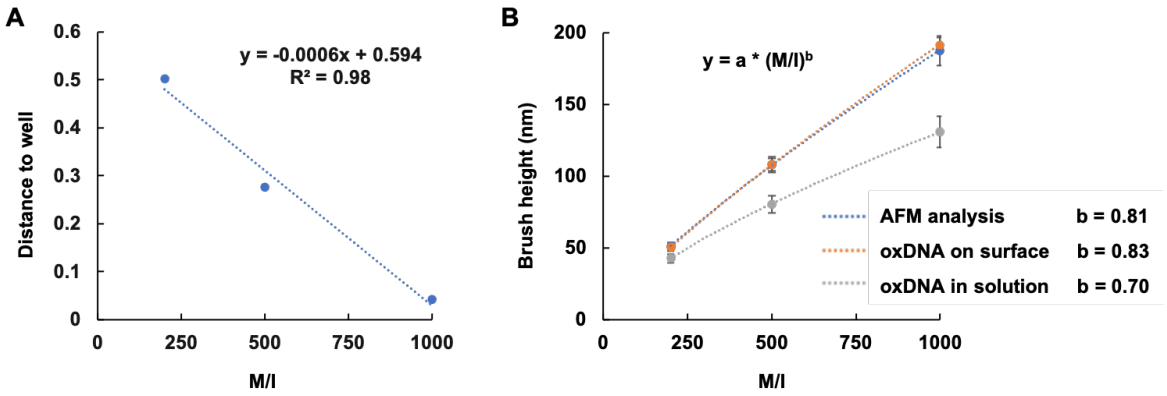

Figure S5. (A) Migration distance on the gel (analysis of **Figure 2A** using ImageJ) as a function of M/I (degree of polymerization) and corresponding linear fit. **(B)** Power law fits of brush height (corona thickness) as a function of M/I. Data obtained by AFM image analysis and by MD simulations on surface and in solution (see also **Figure 2C**).

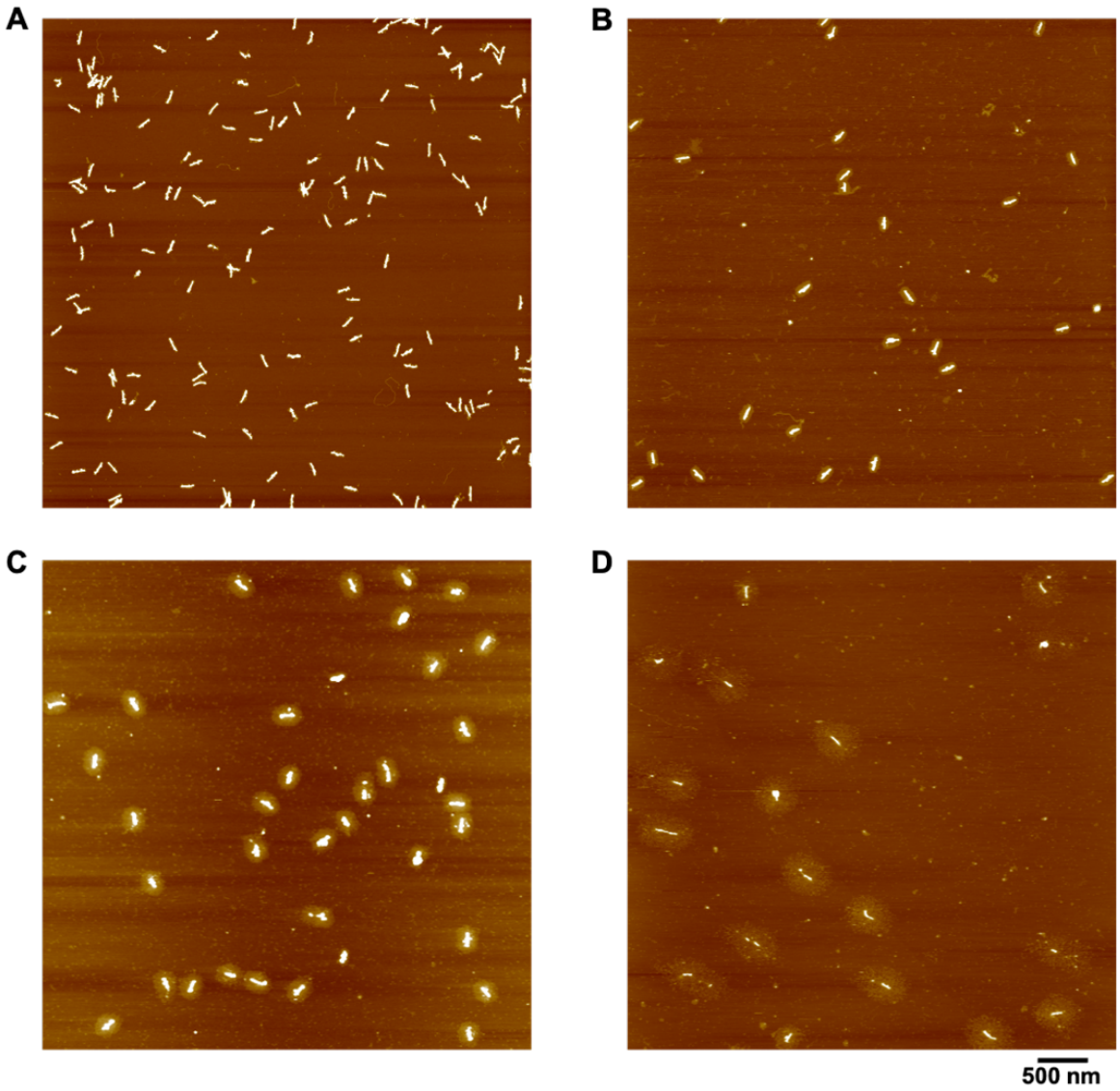

Figure S6. AFM images showing that poly(dT) brush height on 16HB-S[4]1/1 is controllable by the M/I feed ratio. **(A)** M/I = 50, **(B)** M/I = 200, **(C)** M/I = 500, and **(D)** M/I = 1000.

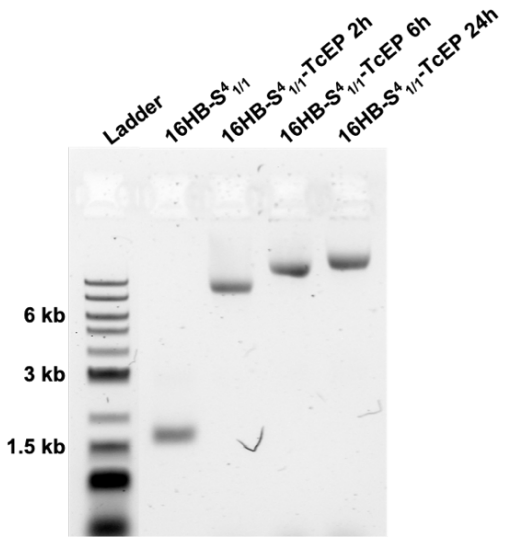

Figure S7. Agarose gel image showing the effect of SI-TcEP time (2 h, 6 h, and 24 h) on the migration distance of fullydecorated 16HB (16HB-$S^4$1/1) at constant M/I = 500.

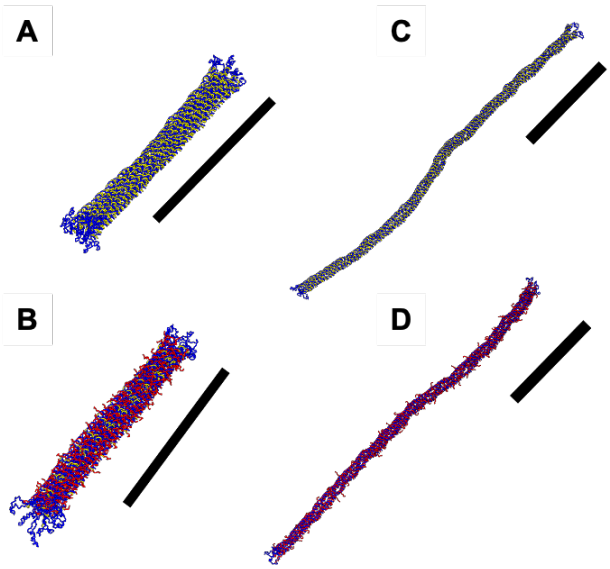

Figure S8. oxDNA simulations of 16HB and 6HB with and without oligo(dT)8 extensions at 3' ends of staples. **(A, B)**: 16HB; **(C, D)**: 6HB. The top row shows that DNA origami structures were folded using staples without oligo(dT)8 extensions (yellow). The bottom row shows the fully decorated cases for 16HB and 6HB, where the red strands have oligo(dT)8 extensions at 3' ends (144 staples with extensions for 16HB and 162 staples with extensions for 6HB).

Comparison of **(B)** and (**D)** also shows that the oligonucleotide initiator density is much lower for the 6HB. Scale bars are all 100 nm.

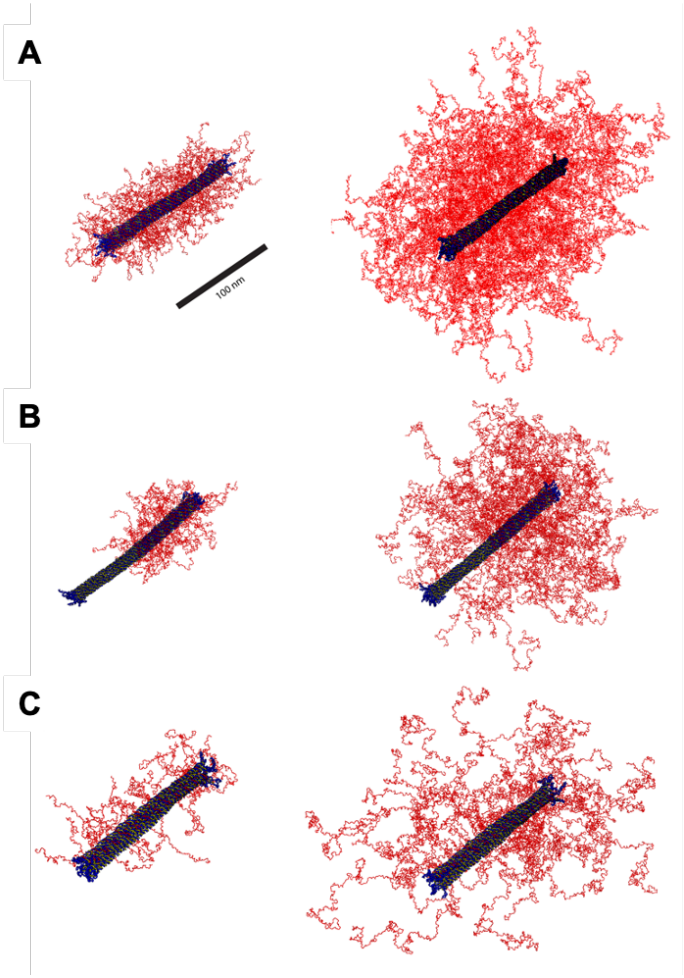

Figure S9. oxDNA simulations of 16HBs decorated with three different polynucleotide brush patterns in solution. **(A)** Fully decorated on 144 stands (16HB-$S^4$1/1); **(B)** decorated on one half with 72 strands (16HB-$S^4$1/2); **(C)** decorated on one face with 36 strands (16HB-$S^1$1/1). The left column shows pn-DONs with poly(dT)200 brushes and the right column shows pn-DONs with poly(dT)1000 brushes.

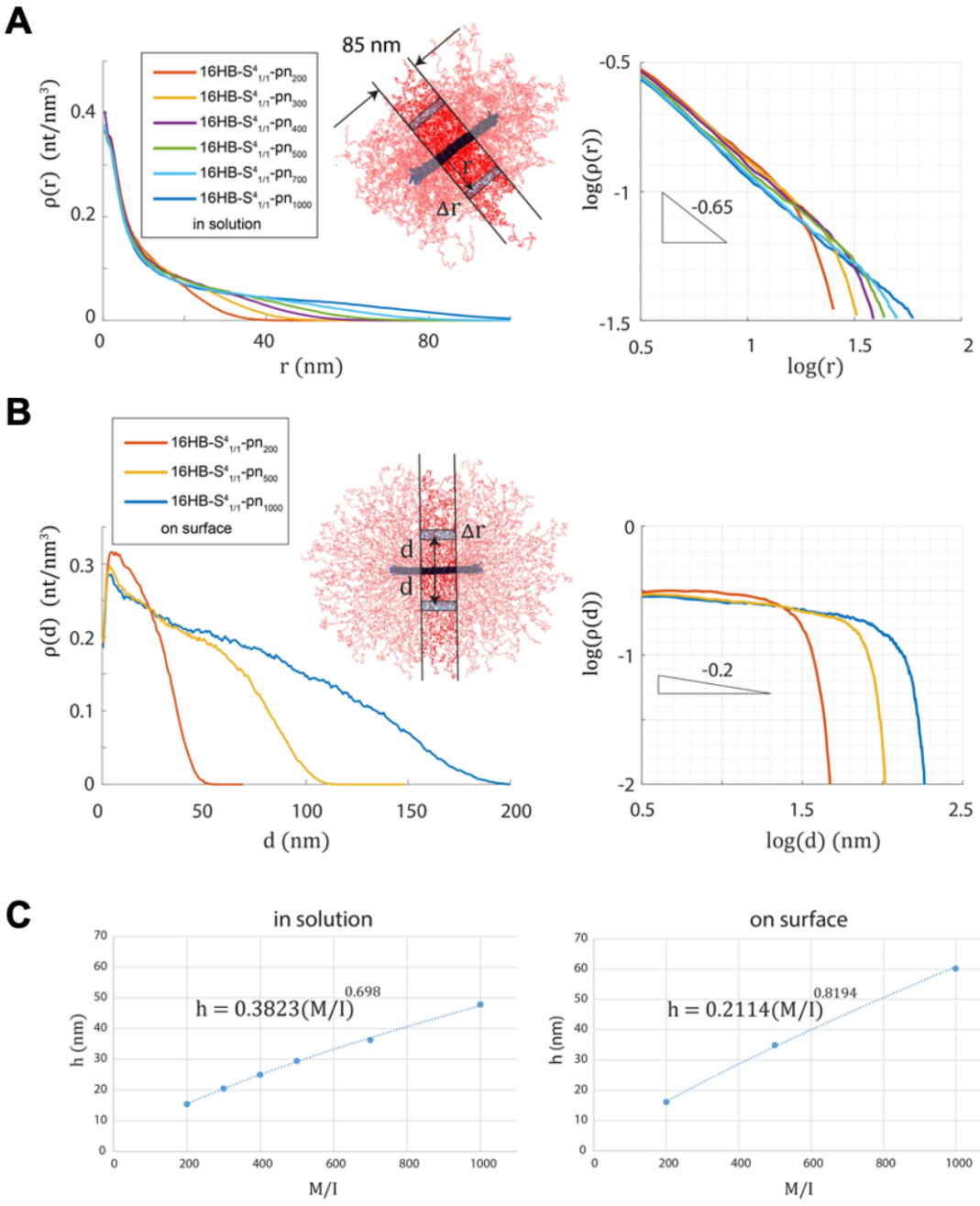

Figure S10. Segment density profiles and brush heights of polynucleotide brushes on fully decorated 16HB-based pn-DONs in solution and on surface. **(A)** Density profiles $\rho(r)$ in solution plotted as a function of distance r from the surface of the origami cores. The density was calculated as $\rho(r) = \langle n(r)\rangle/(2\pi r\Delta r\Delta l)$, where $\langle n(r)\rangle$ is the number of nucleotides (averaged over the simulation trajectory) residing within a cylindrical shell of mean radius r, thickness Δr =0.8 nm, and length Δl = 85 nm centered longitudinally to avoid ends effects, and $2\pi r\Delta r\Delta l$ is the volume of the cylindrical shell. **(B)** Density profiles $\rho(d)$ on surface plotted as a function of distance d from the surface of the origamicores. Due to the quasi-2D geometry, $\rho(d)$ was calculated using planar shells of thickness $\Delta r = 0.8$ nm, length $\Delta l = 85$

nm, and of breadth compatible with the origami thickness (t = 10 nm). The log-log plots in **(A)** and **(B)** show the scaling of ρ with respect to r or d. Note that the segment density for the on-surface case decays with a very small scaling approaching zero. This suggests that on the surface the polynucleotide chains are stretched further away fromthe origami cores, which is also reflected in the larger average brush height. **(C)** Average brush height h plotted as a function of the M/I ratio. The dotted lines represent the power law fits to the data.

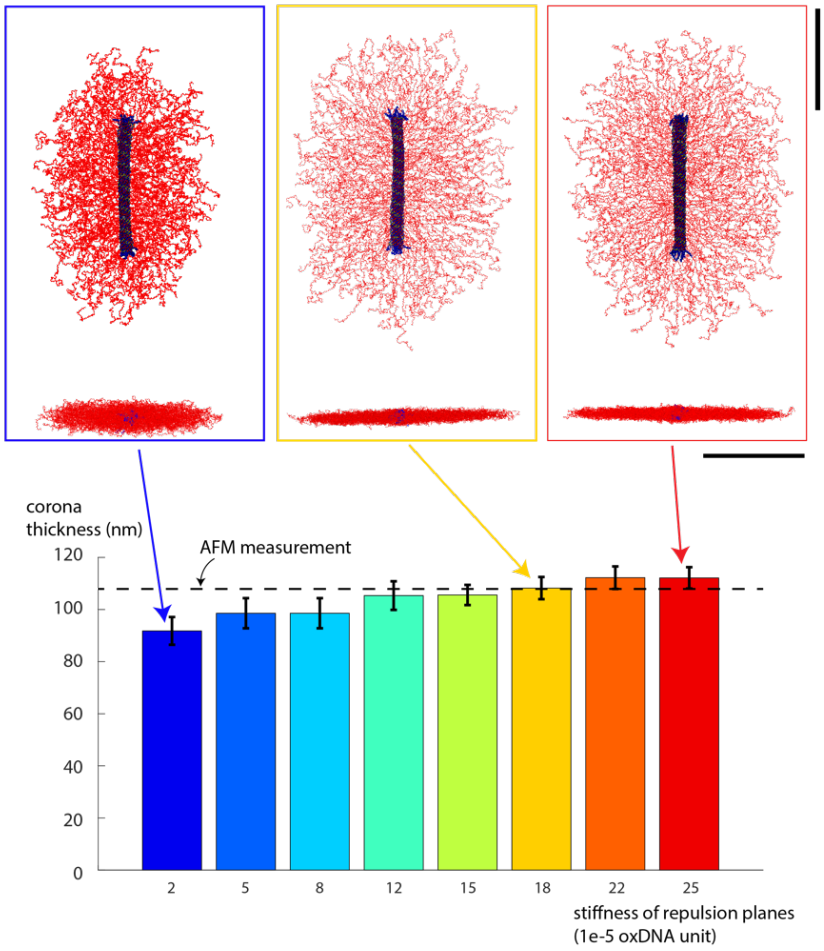

Figure S11. The interaction of single-stranded polynucleotide chains with the mica surface during deposition and dryingof pn-DONs causes significant flattening of the structure (primarily the brushes), as visible in the AFM images. This brush conformation is clearly different from that observed and simulated in solution using oxDNA. To compare AFM images with simulation results, we applied a set of repulsion planes separated by 34 nm (similar to our earlier study[13])to confine the 16HB-S^{4}1/1-pn500 structure within a quasi-2D space. The results show (from left to right) that increasing the stiffness of the repulsion

planes increases the flattening of the structure. Calibrating with the conformational data obtained from AFM measurements of the 16HB-S^{4}1/1-pn500, we selected a stiffness of 18 × 10^{-5} oxDNA stiffness unit (1oxDNA stiffness unit = 57.18 (pN/nm)) for the repulsion planes, used also for all other cases in this study. Scale bars are 100 nm.

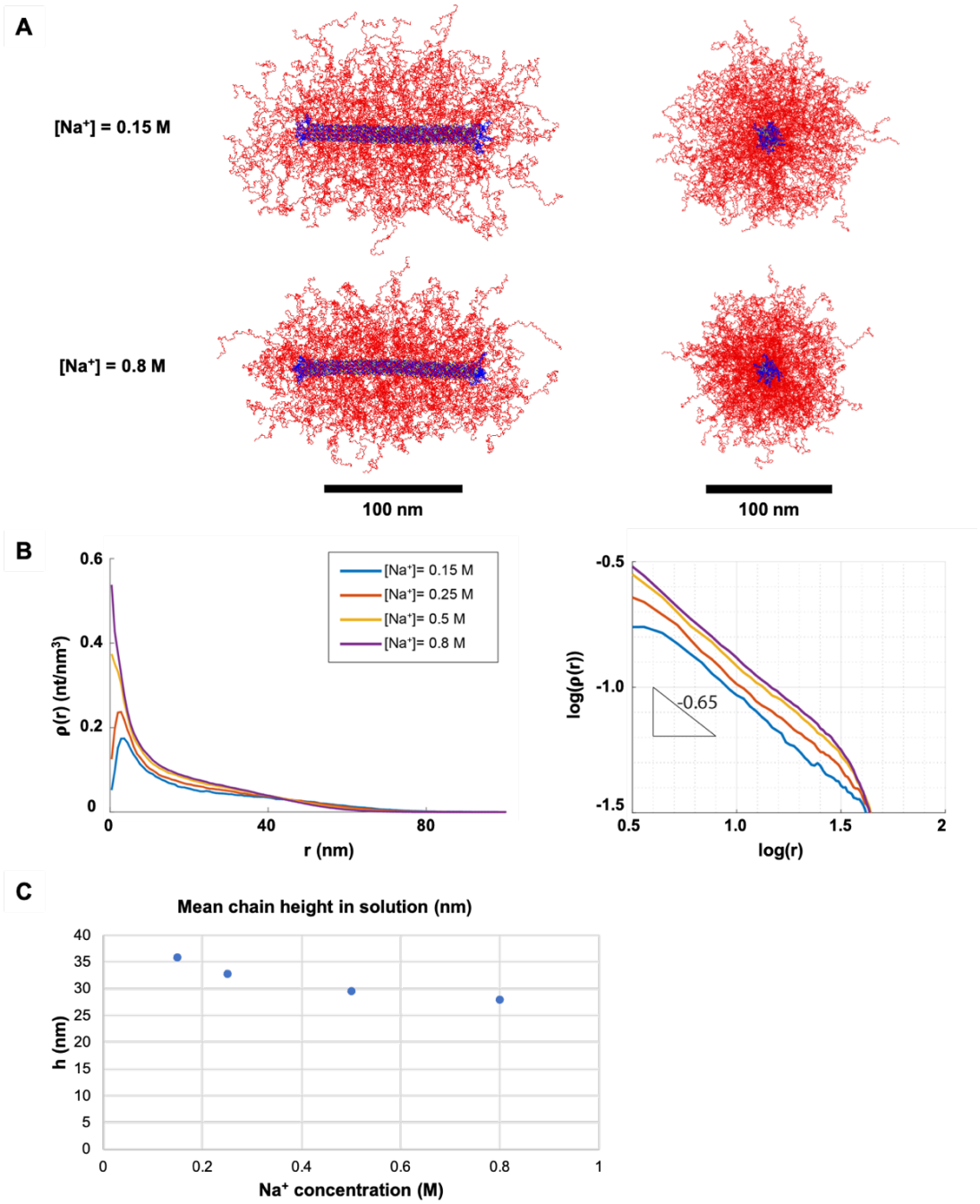

Figure S12. Segment density profiles and brush heights of polynucleotide brushes on 16HB-S^{4}1/1-pn500 in solution at different Na^+ concentrations. **(A)** Side view (left) and front view (right) of oxDNA simulations for 16HB-S^{4}1/1-pn500 at Na^+concentration of 0.15 M (top)

and 0.8 M (bottom). **(B)** Density profiles $\rho(r)$ in solution plotted as a function of distance r from the surface of the origami cores (see **Figure S10A** for more details). The log-log plot shows the scaling of ρ withrespect to r. **(C)** Average brush height h plotted as a function of Na^+ concentration.

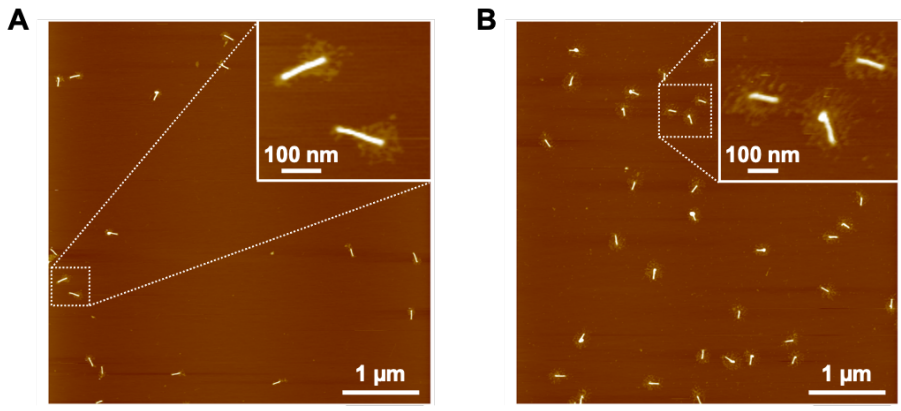

Figure S13. AFM images for **(A)** 16HB-S^{4}1/6-pn500 and **(B)** 16HB-S^{4}1/3-pn500.

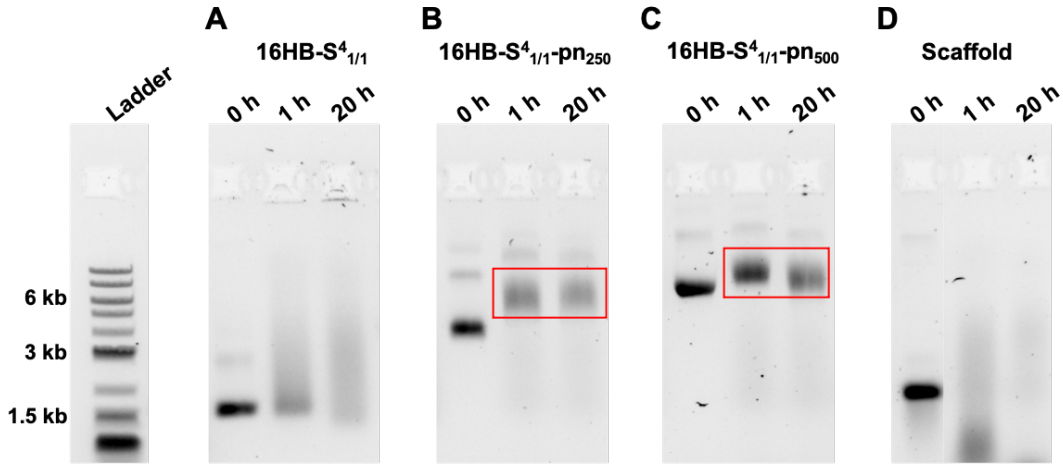

Figure S14. Agarose gel electrophoresis images showing the nuclease stability of 16HB DNA origami without and withpoly(dT) brush corona upon incubation with 10% FBS for different lengths of time. **(A)** 16HB without poly(dT) brush corona. **(B)** Fully decorated 16HB (M/I = 250). **(C)** Fully decorated 16HB (M/I = 500). **(D)** Scaffold of 16HB. The assay was supplemented with 10 mM Mg^{2+} to maintain the stability of the origami core.

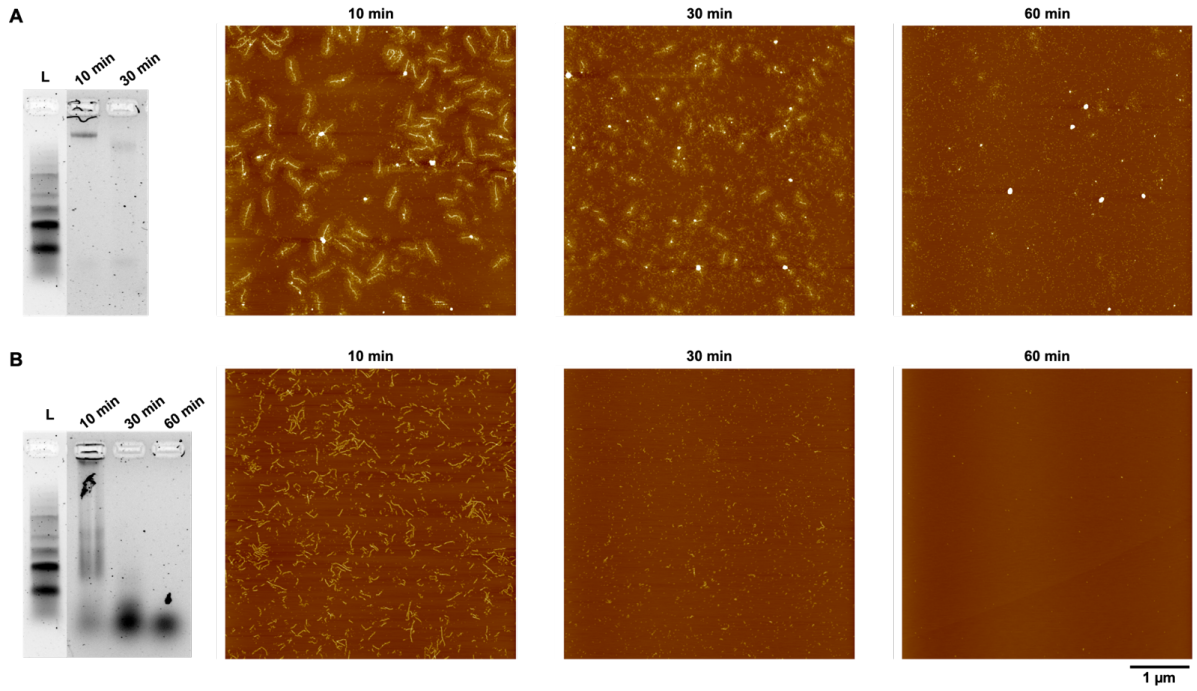

Figure S15. Gel electrophoresis and AFM images showing the stability of 6HBs with **(A)** and without **(B)** poly(dT) brushcorona (M/I = 500) upon incubation with 3.6 U/mL DNase I for different lengths of time. The assay was supplemented with 10 mM Mg^{2+} to maintain the stability of the origami core.

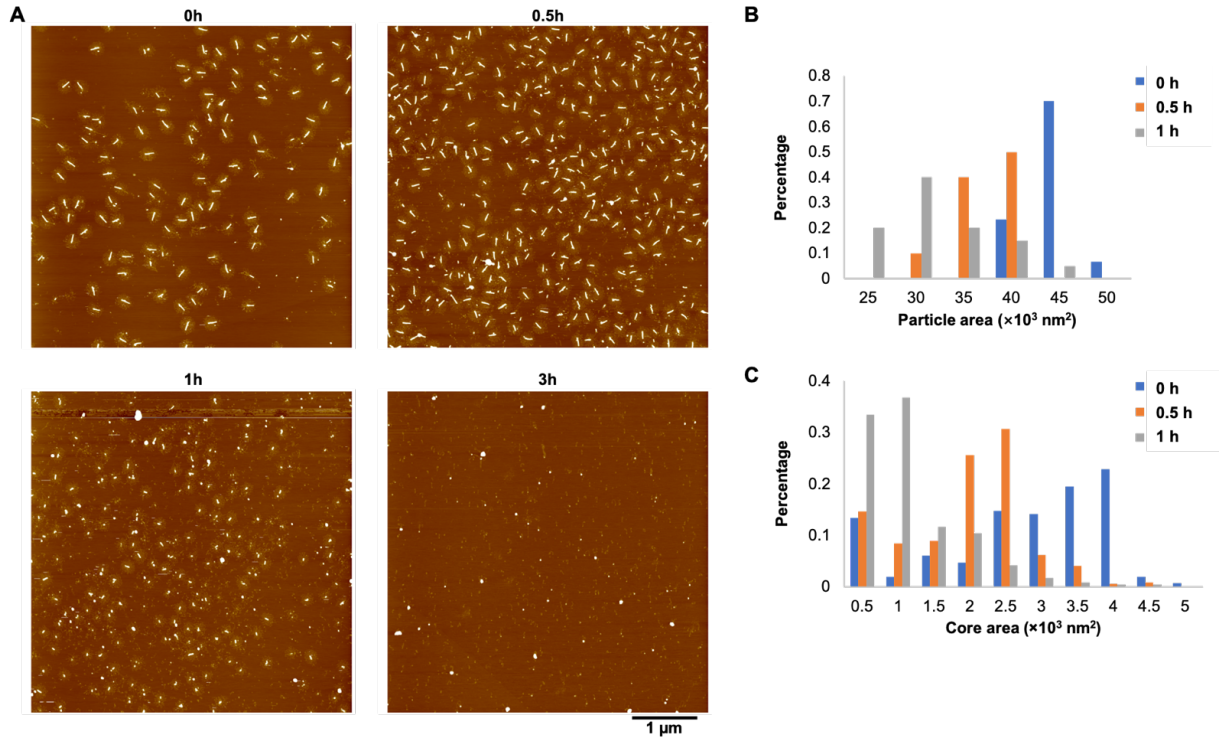

Figure S16. (A) AFM images showing the stability of half-modified 16HB-S^{4}1/2-pn500 (M/I = 500) upon incubation with 3.6 U/mL DNase I for different lengths of time. AFM image analysis of **(B)** the area of pn-DON particles and **(C)** the areaof origami cores at different time points. The assay was supplemented with 10 mM Mg^{2+} to maintain the stability of the origami core.

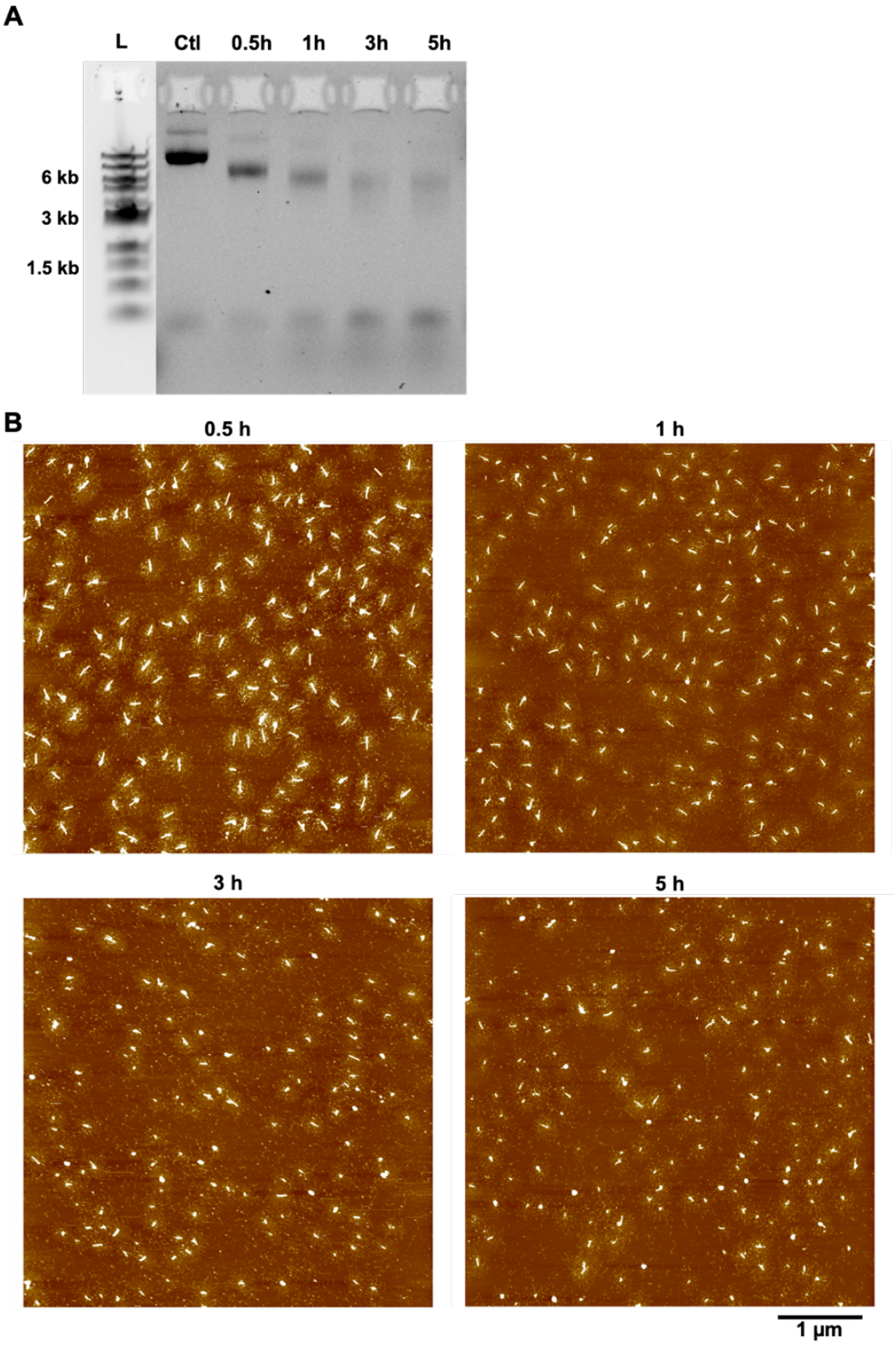
A
L
Ctl
0.5h
1h
3h
5h
6 kb
3 kb
1.5 kb
B
0.5 h
1 h
3 h
5 h
1 µm

Figure S17. (A) Gel electrophoresis image and **(B)** AFM images showing the stability of half-modified 16HB-S^{4}1/2-pn1000 (M/I = 1000) upon incubation with 3.6 U/mL DNase I for different lengths of time. The assay was supplemented with 10mM Mg^{2+} to maintain the stability of the origami core.

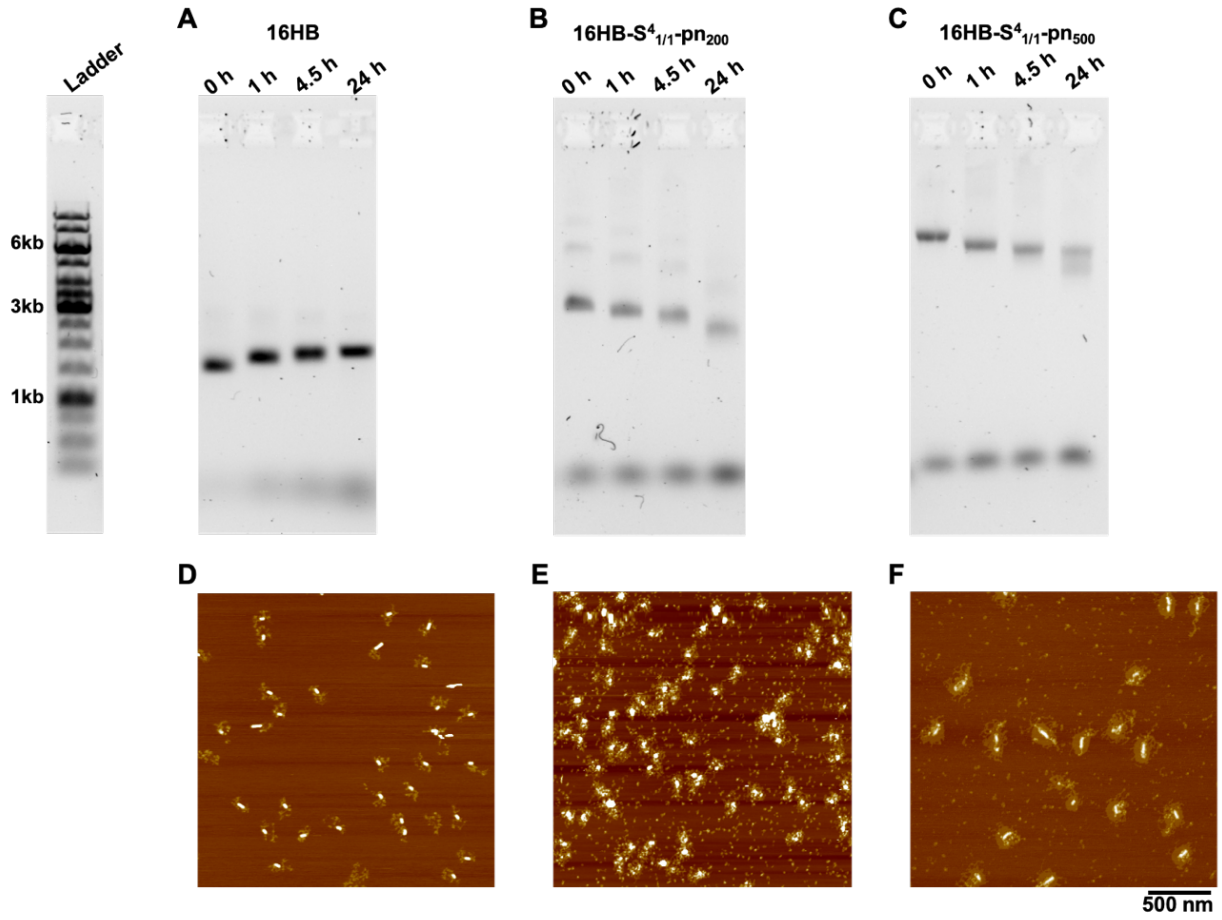

Figure S18. Mg^{2+} depletion assay to study the stability of 16HB without and with poly(dT) brush corona in physiological buffer conditions, *i.e.*, low Mg^{2+} concentration. Agarose gel images showing the stability of **(A)** 16HB without poly(dT) brush corona, **(B)** fully decorated 16HB (M/I = 200), and **(C)** fully decorated 16HB (M/I = 500) after incubation in 1X DPBS (containing 0.9 mM Ca^{2+} and 0.5 mM Mg^{2+}) at 37 °C for different lengths of time. AFM images showing

the morphology of **(D)** 16HB, **(E)** 16HB-S^{4}1/1-pn200, and **(F)** 16HB-S^{4}1/1-pn500 after 24 h incubation.

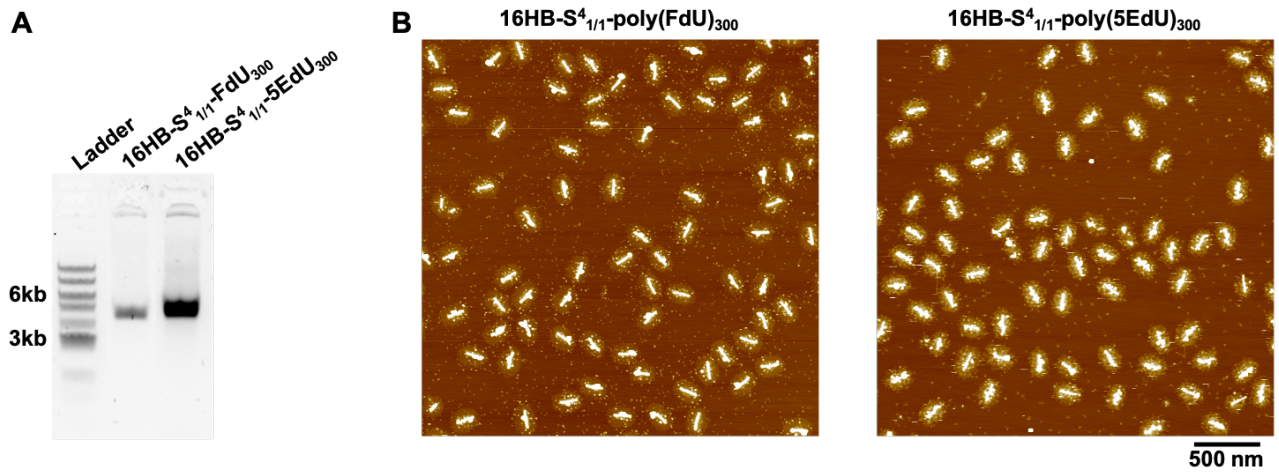

Figure S19. Surface-initiated polymerization of non-natural nucleotides. **(A)** Gel electrophoresis image and **(B)** AFM images for polymerization of 5F-dUTP and 5E-dUTP on 16HB-S^{4}1/1 with M/I = 300.

2.7.5 Supporting Table

Table S1. Comparison of brush heights of 16HB-S[4]1/1-pn200, 16HB-S[4]1/1-pn500, and 16HB-S[4]1/1-pn1000 obtained from AFMimage analysis with those predicted by 2D (on surface) and 3D (in solution) oxDNA simulations.

	M/I = 200	**M/I = 500**	**M/I = 1000**	**n**
Theoretical contour length / **Estimated brush height**	135.2 nm	338.0 nm	676.0 nm	N/A
AFM analysis (nm)	51.10 ± 2.50	107.91 ± 5.38	187.57 ± 10.36	20-35
On surface simulation (nm)	50.21 ± 2.47	108.23 ± 4.27	191.46 ± 5.53	100
In solution simulation (nm)	42.64 ± 2.97	80.38 ± 5.90	130.99 ± 10.84	200

2.8 References.

[1] M. DeLuca, Z. Shi, C. E. Castro, G. Arya, *Nanoscale Horiz* **2020**, *5*, 182-201; b) P. Wang, T. A. Meyer, V. Pan, P. K. Dutta, Y. Ke, *Chem* **2017**, *2*, 359-382; c) P. W. K. Rothemund,

Nature **2006**, *440*, 297-302; d) F. Hong, F. Zhang, Y. Liu, H. Yan, *Chem Rev* **2017**, *117*, 12584-12640; e) T. Tørring, N. V. Voigt, J. Nangreave, H. Yan, K. V. Gothelf, *Chem Soc Rev* **2011**, *40*, 5636-5646.

[2] A. H. Okholm, H. Aslan, F. Besenbacher, M. Dong, J. Kjems, *Nanoscale* **2015**, *7*, 10970-10973.

[3] a) R. Jungmann, M. S. Avendaño, J. B. Woehrstein, M. Dai, W. M. Shih, P. Yin, *Nat Methods* **2014**, *11*, 313-318; b) M. Dai, R. Jungmann, P. Yin, *Nat Nanotechnol* **2016**, *11*, 798-807.

[4] a) J. Li, C. Fan, H. Pei, J. Shi, Q. Huang, *Adv Mater* **2013**, *25*, 4386-4396; b) P. D. Halley, C. R. Lucas, E. M. McWilliams, M. J. Webber, R. A. Patton, C. Kural, D. M. Lucas, J. C. Byrd, C. E. Castro, *Small* **2016**, *12*, 308-320; c) Y.-X. Zhao, A. Shaw, X. Zeng, E. Benson, A. M. Nyström, B. r. Högberg, *ACS nano* **2012**, *6*, 8684-8691; d) Q. Zhang, Q. Jiang, N. Li, L. Dai, Q. Liu, L. Song, J. Wang, Y. Li, J. Tian, B. Ding, *ACS nano* **2014**, *8*, 6633-6643.

[5] A. R. Chandrasekaran, N. Anderson, M. Kizer, K. Halvorsen, X. Wang, *ChemBioChem* **2016**, *17*, 1081-1089.

[6] Q. Jiang, S. Liu, J. Liu, Z. G. Wang, B. Ding, *Adv Mater* **2019**, *31*, e1804785.

[7] a) S. Senapati, A. K. Mahanta, S. Kumar, P. Maiti, *Signal Transduct Target Ther* **2018**, *3*, 7; b) A. Wicki, D. Witzigmann, V. Balasubramanian, J. Huwyler, *J Control Release* **2015**, *200*, 138-157; c) S. Gupta, P. K. Gupta, G. Dharanivasan, R. S. Verma, *Nanomedicine* **2017**, *12*, 2675-2692.

[8] S. D. Perrault, W. M. Shih, *ACS Nano* **2014**, *8*, 5132-5140.

[9] J. Mikkila, A. P. Eskelinen, E. H. Niemela, V. Linko, M. J. Frilander, P. Torma, M. A. Kostiainen, *Nano Lett* **2014**, *14*, 2196-2200.

[10] N. Ponnuswamy, M. M. C. Bastings, B. Nathwani, J. H. Ryu, L. Y. T. Chou, M. Vinther, W. A. Li, F. M. Anastassacos, D. J. Mooney, W. M. Shih, *Nat Comms* **2017**, *8*, 15654.

[11] N. P. Agarwal, M. Matthies, F. N. Gür, K. Osada, T. L. Schmidt, *Angew Chem Int Ed* **2017**, *56*, 5460-5464.

[12] S. T. Wang, M. A. Gray, S. Xuan, Y. Lin, J. Byrnes, A. I. Nguyen, N. Todorova, M. M. Stevens, C. R. Bertozzi, R. N. Zuckermann, O. Gang, *Proc Natl Acad Sci U S A* **2020**, *117*, 6339-6348.

[13] Y. Tokura, Y. Jiang, A. Welle, M. H. Stenzel, K. M. Krzemien, J. Michaelis, R. Berger, C. Barner-Kowollik, Y. Wu, T. Weil, *Angew Chem Int Ed* **2016**, *55*, 5692-5697.

[14] a) L. Tang, V. Tjong, N. Li, Y. G. Yingling, A. Chilkoti, S. Zauscher, *Adv Mater* **2014**, *26*, 3050-3054; b) L. Tang, L. A. Navarro, Jr., A. Chilkoti, S. Zauscher, *Angew Chem Int Ed Engl* **2017**, *56*, 6778-6782.

[15] F. J. Bollum, in *The Enzymes*, 3rd ed. (Ed.: P. D. Boyer), Academic Press, New York, **1974**, pp. 145-171.

[16] R. Gu, T. Oweida, Y. G. Yingling, A. Chilkoti, S. Zauscher, *Biomacromolecules* **2018**, *19*, 3525-3535.

[17] a) D. C. Chow, W.-K. Lee, S. Zauscher, A. Chilkoti, *J Am Chem Soc* **2005**, *127*, 14122-14123; b) V. Tjong, L. Tang, S. Zauscher, A. Chilkoti, *Chem Soc Rev* **2014**, *43*, 1612-1626; c) S. Deshpande, Y. Yang, A. Chilkoti, S. Zauscher, in *Methods in enzymology, Vol. 627*, Elsevier, **2019**, pp. 163-188.

[18] a) B. E. K. Snodin, F. Randisi, M. Mosayebi, P. Sulc, J. S. S. F. Romano, F. Romano, T. E. Ouldridge, R. Tsukanov, E. Nir, A. A. Louis, J. P. K. Doye, *J Chem Phys* **2015**, *142*, 234901; b) J. P. K. Doye, T. E. Ouldridge, A. A. Louis, F. Romano, P. Sulc, C. Matek, B. E. K. Snodin,

L. Rovigatti, J. S. Schreck, R. M. Harrison, W. P. J. Smith, *Phys Chem Chem Phys* **2013**, *15*, 20395-20414; c) L. Rovigatti, P. Šulc, I. Z. Reguly, F. Romano, *J Comput Chem* **2015**, *36*, 1-8.

[19] a) J. Le Guillou, J. Zinn-Justin, *Physical Review B* **1980**, *21*, 3976; b) K. Binder, A. Milchev, *J Polym Sci Part B: Polym Phys* **2012**, *50*, 1515-1555.

[20] D. S. Seferos, A. E. Prigodich, D. A. Giljohann, P. C. Patel, C. A. Mirkin, *Nano Lett* **2009**, *9*, 308-311.

[21] E. Benson, A. Mohammed, J. Gardell, S. Masich, E. Czeizler, P. Orponen, B. Högberg, *Nature* **2015**, *523*, 441-444.

[22] L. Li, W. Sun, J. Zhong, Q. Yang, X. Zhu, Z. Zhou, Z. Zhang, Y. Huang, *Adv Funct Mater* **2015**, *25*, 4101-4113.

Chapter 3. Spatiotemporal Control of Polynucleotide Brush Growth and Mesoscale Self-assembly of DNA Origami Nanorod

3.1 Abstract

We show that the combination of surface-initiated, TdT (terminal deoxynucleotidyl polymerase) catalyzed enzymatic polymerization (SI-TcEP) with precisely engineered DNA origami nanostructures (DONs) presents an innovative pathway for the generation of stable, polynucleotide brush-functionalized origami nanostructures. Specifically, we demonstrate that SI-TcEP can be used to site-specifically decorate DONs with brushes containing not only natural but also non-natural nucleotides. The brush functionalization can be precisely controlled in terms of the site-specific location of initiation sites on the origami core and the brush height and composition. Coarse-grained simulations are able to predict the morphology of brush-functionalized DONs and reveal a monomer density scaling that is consistent with the experimentally observed brush conformation of surface-functionalized DONs. We find that compared to unprotected DNA origami, polynucleotide brush-functionalization increases the nuclease resistance of DONs significantly, and that this stability can be spatially programmed by designing the site-specific location of initiation sites on the origami core. The ability to site-specifically decorate DONs with brushes of natural and non-natural nucleotides provides access to a large range of functionalized DON architectures that would allow for further supramolecular assembly and for potential applications in drug delivery and smart nanoscale delivery systems, where the site-directed degradation of DON-based drug delivery vehicles could facilitate cellular uptake.

Key words: Terminal deoxynucleotidyl transferase, surface-initiated polymerization, molecular dynamics simulations, nuclease resistance, drug delivery

3.2 Introduction

Over the last two decades, research in DNA nanotechnology has seen astonishing growth and has yielded exquisite DNA-based nanostructures that span a broad range of sizes and complexity.[1] DNA origami nanostructures (DONs) have been widely investigated for biomedical applications, such as biosensing,[2] *in vivo* imaging,[3] and drug and gene delivery,[4] due to their inherent biocompatibility, exquisite control over nanoscale geometry, mechanical properties, and suitability for site-specific functionalization.[5]

Self-assembly is a powerful approach for fabricating materials architectures over many length scales. Self-assembly describes the spontaneous arrangement of building blocks into larger structures with well-defined symmetry, complex architecture, and long-range order. The central challenge to achieving self-assembly, however, is the fabrication of building blocks that are encoded with spatially well-defined repulsive and attractive surface chemistries (patches) which provide the directional interactions necessary to drive assembly.

The organization of DNA-based nanomaterials on the mesoscale is an emerging topic because of the importance, of DNA nanodevices in promising recent diagnostic and therapeutic applications,8 among others. While giga-dalton DNA mesostructures have been achieved by site-specific base paring and by shape-complementary blunt-end stacking contacts, the design and assembly of these structures is still formidable and typically results in low yields.8-10 Our ability to site-specifically encode DONs with brushes containing natural and non-natural nucleotides, promises access to a large range of functionalized DON architectures primed for directed supramolecular self-assembly at high yields.

DNA origami nanostructures (DONs) provide an exquisite platform for self-assembly because they can be designed into a vast range of shapes and sizes, and also because they possess

specifically addressable sites for functionalization with nanoscale precision.3-6 Recently we demonstrated that surface-initiated, TdT-catalyzed enzymatic polymerization (SI-TcEP) can site-specifically pattern DONs with polynucleotide brushes containing both natural and non-natural nucleotides. We showed that brush growth can be precisely controlled in terms of the location of initiation sites on the origami core and the brush height and composition, and that the conformations of the brushes could be accurately modeled through coarse-grained simulations. This control will allow us to program the surface chemistry of the building blocks to regulate their interactions with each other, which will offer a route to achieving hierarchically ordered mesostructures.

Here, we report on the strategies that allow for spatiotemporal polymerization and de-grafting (cleavage) of polynucleotide brushes by restriction enzyme cutting. Our experimental results show that we have precise control over blocking, activating, and re-activating of SI-TcEP reactions. Furthermore, we show that this strategy allows sequential SI-TcEP reactions, which can generate bifunctional, asymmetric modification on a single DON. The resulting pn-DONs could be useful for DNA-based drug delivery to incorporate different cargos at the same time. In addition, we show that site-selective modification of DONs is not only useful for hydrophilic polynucleotide brushes growth as shown in our recent publication but can also generate DONs with hydrophobic patches that can self-assemble into mesoscale micellar structures.

3.3 Results and Discussion

3.3.1 Spatiotemporal Control of Polynucleotide Brush Growth on DNA Origami

To this end, we explored site-specific, enzymatic cleavage of surface accessible loops in staple strands using restriction enzymes (REs) (**Scheme 1A**). We can also use RE cutting (**Scheme 1B**), to site-specifically remove (de-graft) polynucleotide chains from the surface of DON. We choose rod-shaped 6-helix bundle (6HB) origami because of its simple geometry and large aspect ratio to demonstrate spatial control. For brevity, we term 6HB modified with oligo(dT)$_8$ initiators as x/27 8T 6HB, 6HB modified with switchable hairpin (HP) initiators as 6/27 HP 6HB, and 6HB modified with removable double-stranded (DS) initiators as 6/27 DS 6HB, where x specifies the number of the 27 fractions of 6HB that is modified with initiators. Similarly, we term 6HB modified with both oligo(dT)$_8$ and HP initiators as 6/27 HP_8T 6HB, 6HB modified with both oligo(dT)$_8$ and DS initiators as 6/27 DS_8T 6HB.

For a typical SI-TcEP reaction, we mixed DONs, dTTP, and TdT together in the TdT reaction buffer and incubated the mixture at 37 C overnight. The resulting pn-DONs were purified by centrifugal filtration and characterized by agarose gel electrophoresis, and, after deposition onto a mica surface, by tapping mode atomic force microscopy (AFM) in air. Here, we kept the monomer to initiator ratio (M/I) constant for dTTP as 500.

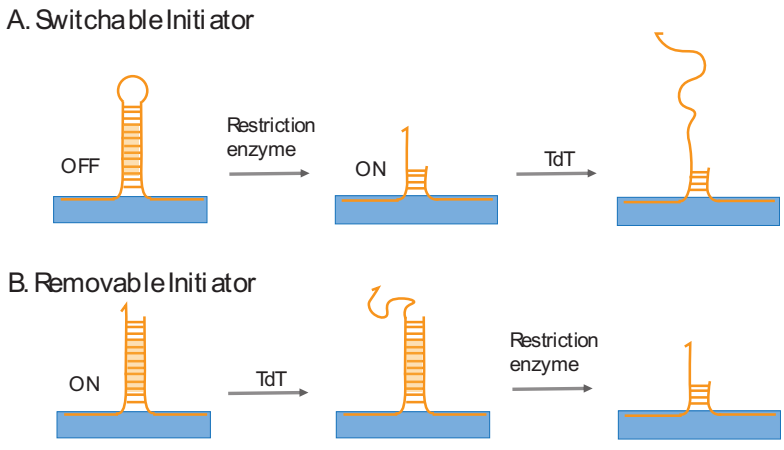

Scheme 1. Schematic showing different designs of the SI-TcEP initiators and their manipulation. (A) Initiator switchable from the OFF to the ON state through RE cutting of a target sequence in

the hairpin. (B) An already ON initiator can be removed after SI-TcEP through RE cutting of a target sequence, generating a new active initiation site.

Activable Initiator

An effective initiator activation strategy is to use restriction enzyme (RE) to cut the restriction sites (RS) embedded in the sequence of the hairpin containing staples (**Scheme 1A**). As a proof-of-concept, we chose a RE called KpnI, of which the restriction site contains 6 base pairs and yields a sticky end with 4 bases at the 3' end (**Figure 1A**). Importantly, this RS sequence has minimum overlap with the sequence of 6HB DNA origami to reduce star activity of RE. By designing in such a way that the 3' end of the hairpins are buried inside the structure of DNA origami (**Figure 1A**), minimum unspecific growth was observed when we added TdT and dTTP directly to structure 1 (labeled as "1+T" in **Figure 1B, 1C**). The short DNA strands on one end of 3/27 6HB observed in Figure 1C for both structure 1 and 1+T (negative control group) are attributed to the hairpin strands. As expected, after activating the hairpins by adding RE, polyT brushes were grown on the activated initiators to yield structure 3 (**Figure 1B, 1C**).

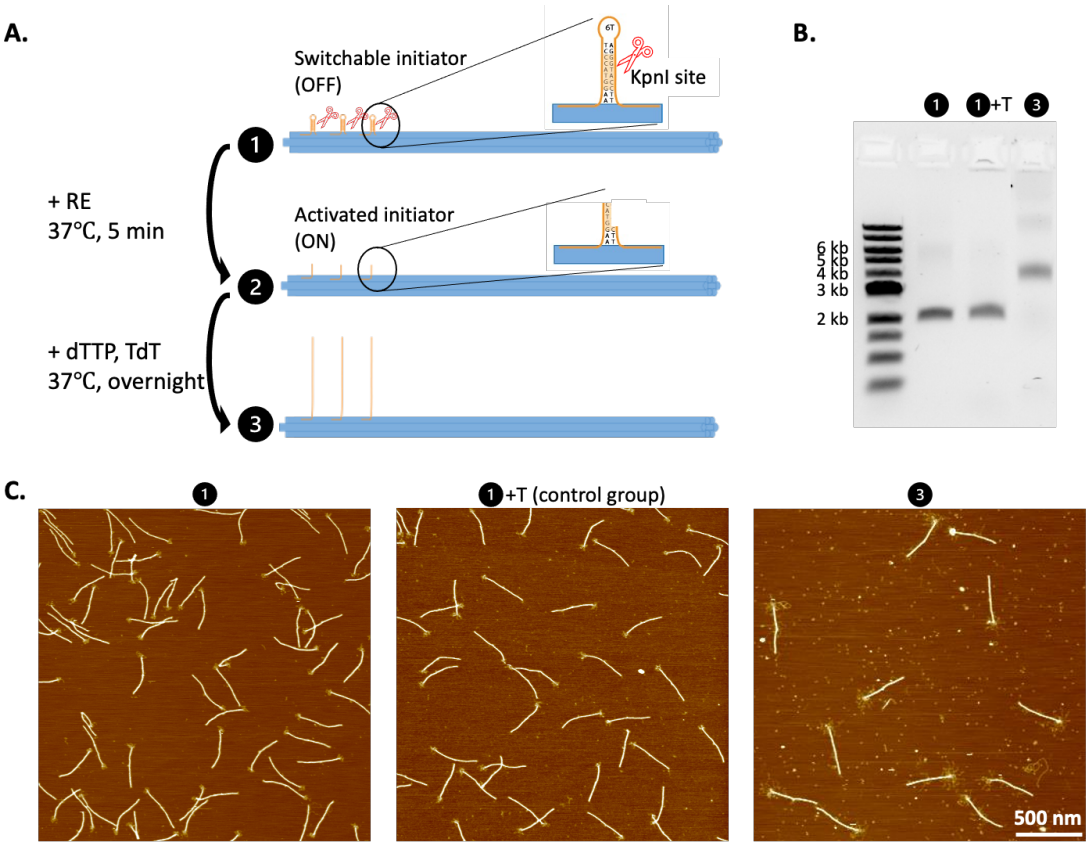

Figure 1. Activable initiators by RE cutting in 3/27 HP 6HB (18 switchable initiators): (A) Schematics showing the process of RE cutting and TcEP reaction; (B, C) Agarose gel image and AFM images showing the growth of polyT before (no unspecific growth) and after initiator activation.

Removable Initiator

Another strategy of initiation control is to design a short double-stranded DNA (dsDNA) with sticky ends as the 3' end of staple strands (**Scheme 1B, Figure 2A**). The sticky end initiators enabled first round of TcEP reaction to yield structure 2 (**Figure 2B**). By designing the dsDNA in a specific way, *i.e.*, containing a restriction cutting site in the stem (indicated by yellow shade in **Figure 2A**), the polyT brushes can be shaved off by adding RE, yielding bare DNA origami with new initiators. The decrease of MW (**Figure 2B**) and the lack of brushes of structure 3 confirmed

the successful removal of polyT brushes. Then polyT brushes can be re-grown by another round of TcEP reaction. The increase of MW (**Figure 2B**) and the existence of brushes of structure 4 confirmed that RE cutting yielded active initiators and enabled polynucleotide brushes growth again. Here, we used dTTP growth as proof of concept, but two different type of polynucleotides containing functional groups can be added sequentially as needed for applications such as biosensors.

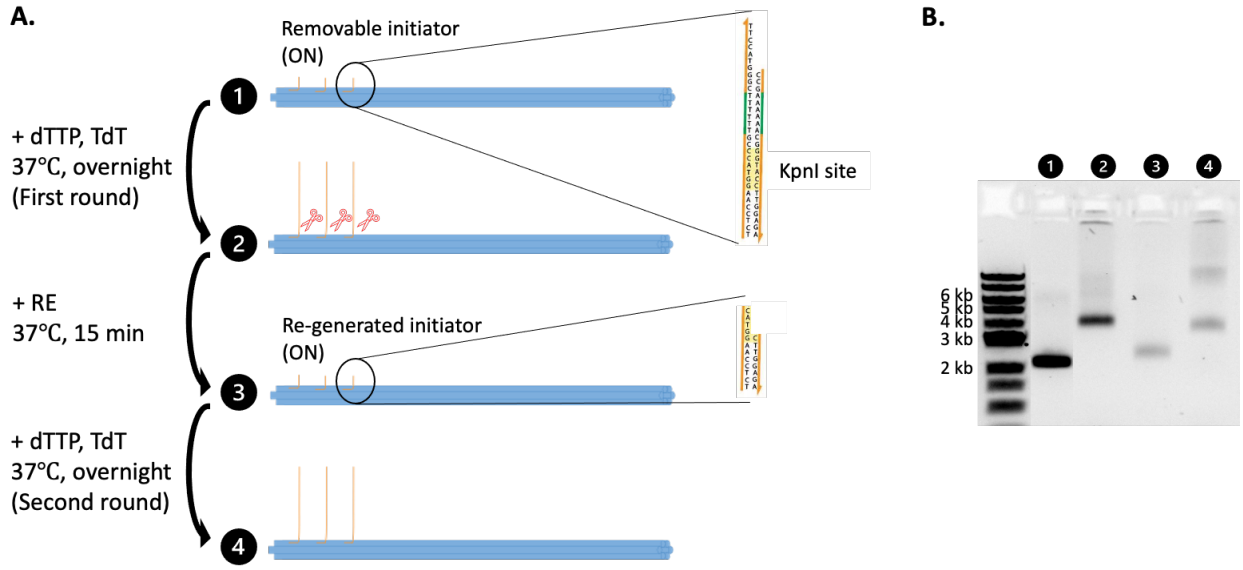

Figure 2. Removable initiators by RE cutting in 6/27 DS 6HB (36 removable initiators): (A) Schematics showing the process of two rounds of TcEP reactions with RE cutting in between; (B) Agarose gel image showing effective brush removal and second round of polyT growth after cutting.

3.3.2 Bi-functional Modification Through Sequential Polymerization

Bi-functional, asymmetric modifications can be achieved by having a combination of different types of initiators (*i.e.*, "always on" 8T initiators and activable/removable initiators) on a single DNA origami nanoparticle. As a proof-of-concept, we showed the combination of 8T initiators

and removable initiators below (**Figure 3A**). In this case, polynucleotide brushes were added to both ends first to yield structure 2, which has polyT brushes on both ends (**Figure 3C**). Then the brushes on the removable side can be cleaved off by adding RE. Successful removal of polyT brushes on only one end of the nanorods can be confirmed by AFM image of structure 3 in Figure 3C. After a second round of TcEP reaction, the nanorods were modified on both ends, but in an asymmetric form with different lengths on two ends, as shown by AFM image of structure 4 in Figure 3C.

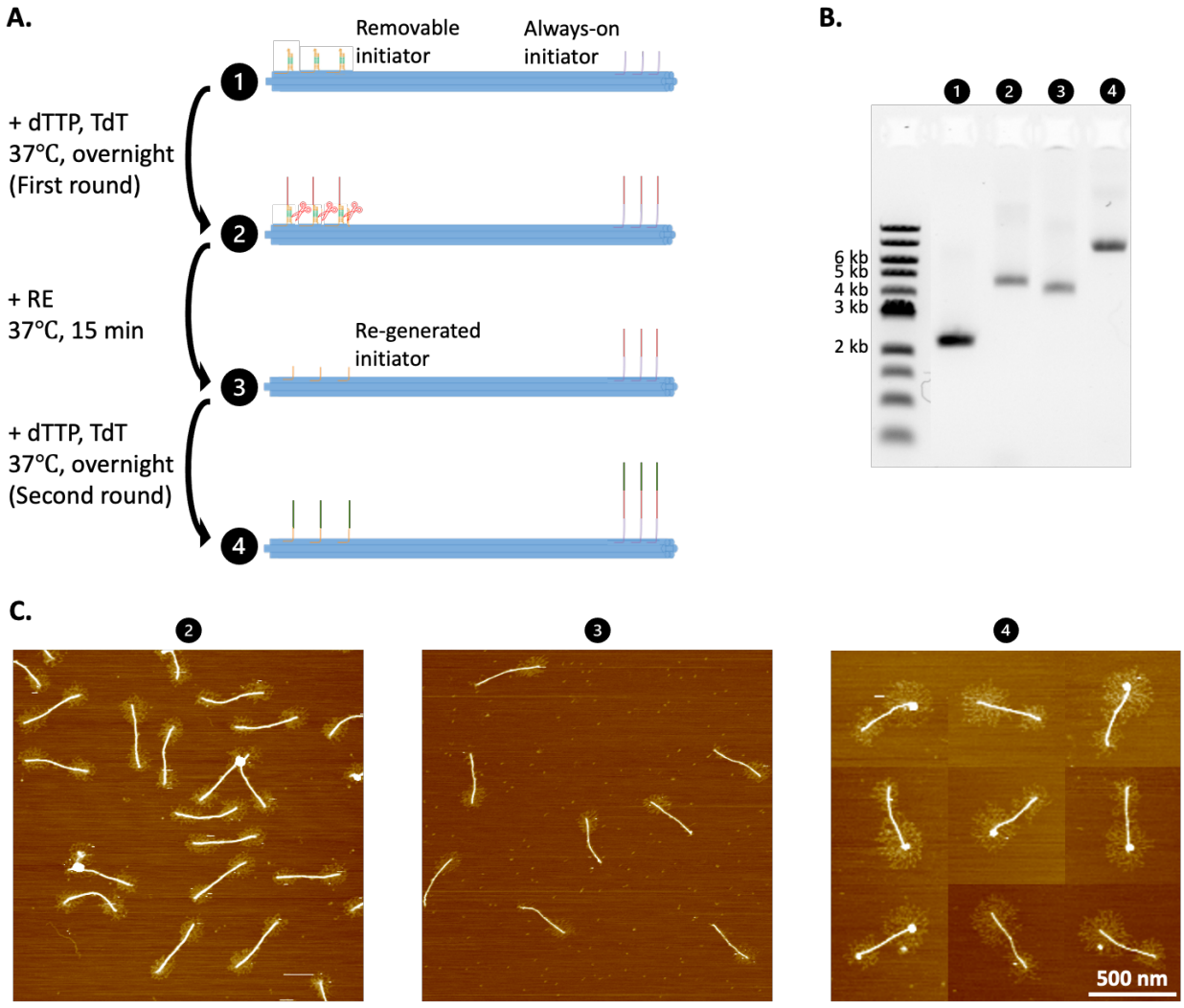

Figure 3. Sequential polymerization on 6/27 DS_HP 6HB (36 removable initiators on one end and 36 active 8T initiators on the other end: (A) Schematics showing the process of RE cutting and

TcEP reaction; (B, C) Agarose gel image and AFM images showing effective brush removal and second round of polyT growth after cutting.

As proof of concept, we used polyT for both rounds of TcEP reactions. But with this controllable sequential growth strategy, two different species of polynucleotides can be added to a single DNA nanorod. We have shown in our previous study that unnatural nucleotides like F-dUTP, a cytotoxic nucleotide, and ethynyl-dUTP, a clickable nucleotide, can be used to modify DNA origami. Therefore, this strategy can be potentially useful for drug delivery, where DNA nanorods can carry polynucleotides with different functions. In addition, if multiple restriction sites that can be cut by different REs exist on the surface of a single DNA origami, polynucleotide brushes can potentially be added sequentially by activating/removing the initiation sites one by one.

3.3.3 Spatio Control of DNA Origami Mesoscale Self-assembly

The site-specific, surface-initiated polymerization of non-natural, hydrophobic nucleotides is a critical first step towards generating building blocks that are suitable for self-assembly. Hydrophobic brush "patches" on DON surfaces can interact through non-specific hydrophobic interactions and through π-π stacking contacts to drive the assembly of pnDONs into mesoscale, micellar structures. For a typical SI-TcEP reaction, we mixed DONs, Atto-dUTP (M/I=5), and TdT together in the TdT reaction buffer and incubated the mixture at 37°C for 1.5 hours unless otherwise indicated. The resulting self-assembled micelles were characterized by tapping mode atomic force microscopy (AFM) in air after being deposited on mica.

We have shown in a previous study that ssDNA can self-assemble into micellar structure after adding hydrophobic nucleotide at the 3' end using TdT. Similarly, adding hydrophobic nucleotides (*e.g.,* Atto-dUTP) to the initiation sites one end of 6HB can induce self-assembly into quasi-micellar "dandelionlike" mesostructures (**Figure 4A, 4B**). Here, the corona of the micelles are rigid DNA origami nanorods instead of flexible polymer strands. Since TdT can only add a certain number (1-2) of hydrophobic nucleotides (data not shown), the number of initiation sites on DNA origami surface will determine the number of hydrophobic moieties, and thus will affect the aggregation behavior. We found that 6/27 8T 6HB gave the best self-assembly behavior (682.2 nm diameter), while 3/27 8T 6HB lacked enough hydrophobicity and 9/27 8T 6HB induced too much aggregation (data not shown). If increasing the incubation time at 37 C to 5 hours or overnight, 3/27 8T 6HB appeared to form more self-assembled structures, indicating that incubation time can also affect aggregation behavior. In addition, similar to the programmable hydrophilic brushes we have shown in a recent study, we can also add hydrophobic moieties to the middle of the nanorod (roller-pin (RP) 7/27 8T 6HB) instead of the end. In this case, mesoscale micelles were also formed, with a much larger aggregation number and smaller diameter (443.2 nm) resulted from different aggregation locations (**Figure 4C, 4D**).

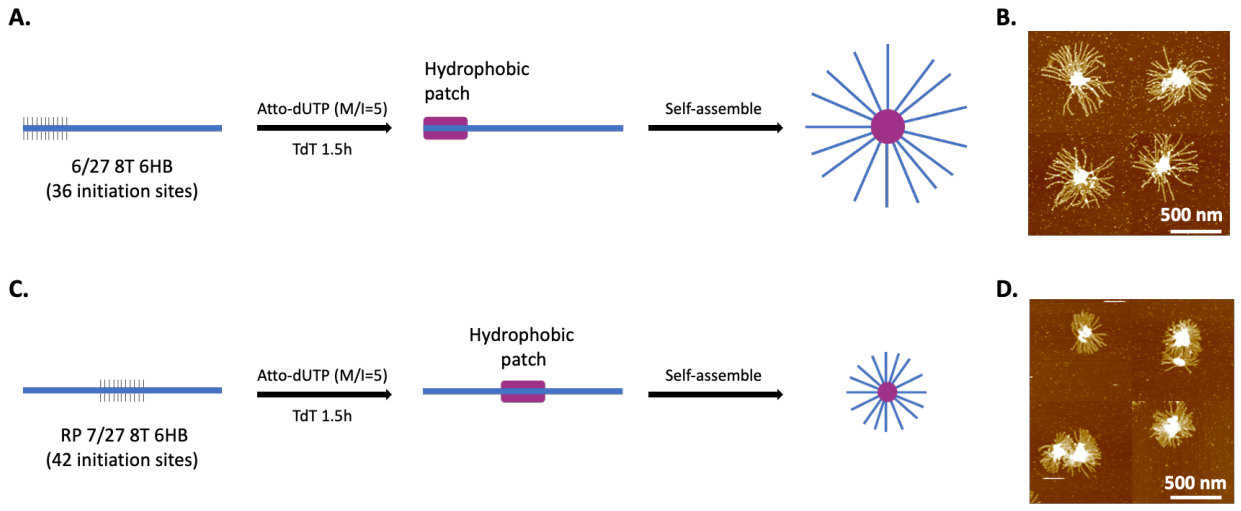

Figure 4. Mesoscale self-assembly of 6HB. (A, C) Schematics showing the location of initiation sites and the aggregation behavior of the amphiphilic 6HB nanorods; (B, D) AFM images showing the mesoscale micelles formed by amphiphilic 6HB nanorods.

Effect of missing staples: To increase the flexibility and hydrophilicity of the micellar corona, we removed some or all of the staple strands on the other end of 6/27 8T 6HB during origami annealing (**Figure 5A**) and then added hydrophobic moieties to the 8T initiation sites by TcEP reaction. Interestingly, the resulting self-assembled micelles appeared to have distinguished morphology and size. With more staples being removed, the corona became more flexible (**Figure 5B**), and the size of the micelles decreased from 682.2 nm to 278.7 nm (**Figure 5C**). Since drug delivery systems for different applications require different sizes of nano-/micro- particles, this origami micelle platform can be useful for a range of all-nucleotide drug delivery applications.

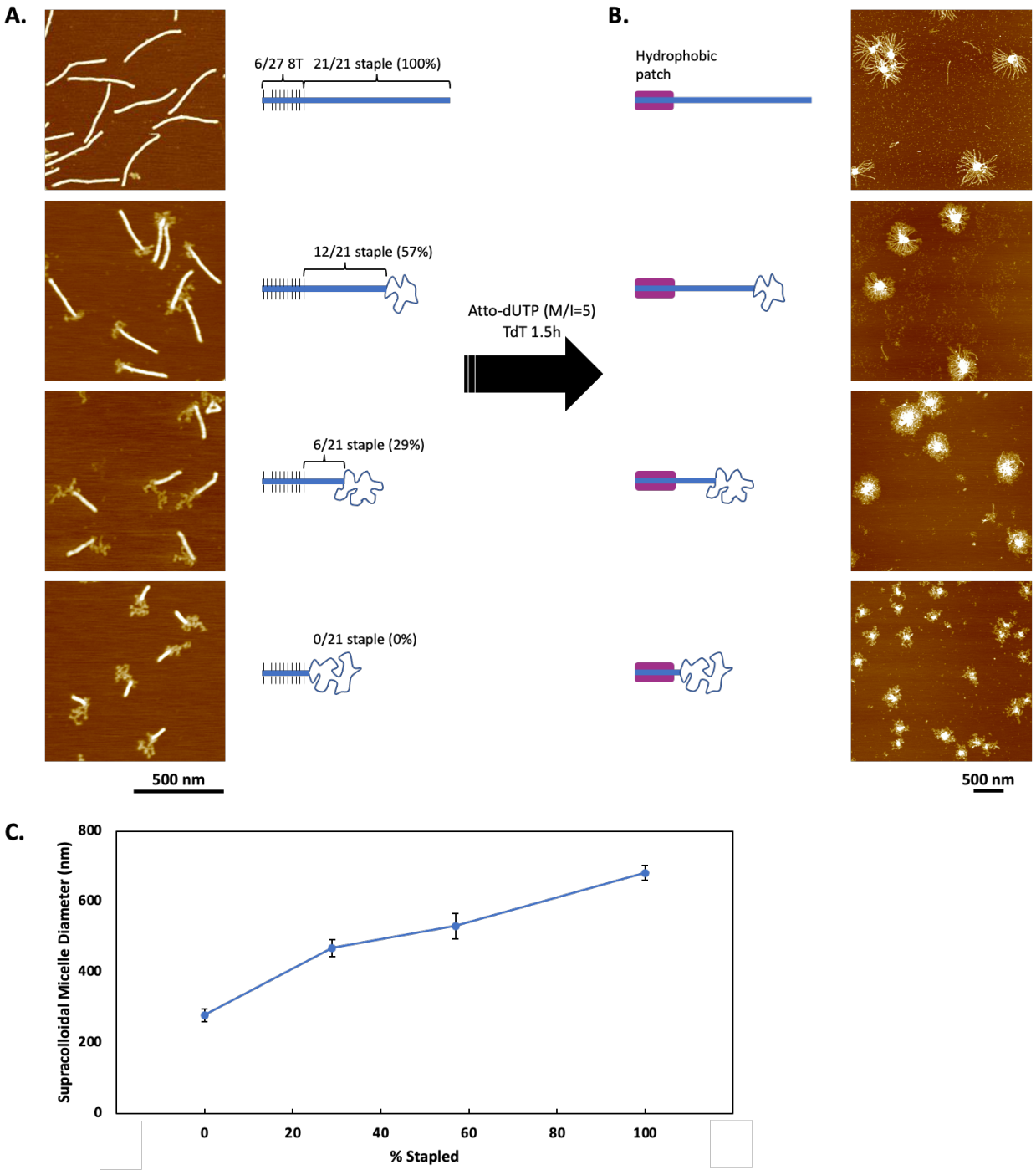

Figure 5. Mesoscale self-assembly of 6/27 8T 6HB with removed staples. (A) AFM images and schematics showing the location and number of missing staples on 6HB; (B) Schematics and AFM images showing the aggregation behavior of the amphiphilic 6HB nanorods with missing staples; (C) Graph showing the diameter of supracolloidal micelles with different staple percentage.

3.4 Conclusions

In summary, our research on the synergistic combination of surface initiated enzymatic polynucleotide brush synthesis with precisely engineered DNA origami is new and presents, guided by multiscale modeling, an innovative pathway for the generation of adaptive, stable polynucleotide brush-functionalized origami nano- and meso-structures. Specifically, we have devised a strategy that harnesses the broad polymerization capability of TdT to synthesize adaptive DNA origami nanostructures by site-specifically programming the surface-initiated growth of polynucleotide brushes on the surface of DNA origami. We found that fully brush-decorated pn-DONs can be stable for many hours in presence of nucleases and physiologically relevant buffer conditions. We showed that site-specific, partial brush decoration will direct nuclease degradation primarily to unprotected areas of the origami core, thus providing a route to generate adaptive pn-DONs. Finally, the ability of TdT to polymerize a broad range of nucleotide analogues enables the synthesis of a broad range of polynucleotide brush-modified DNA origami which are poised to find applications ranging from drug delivery and biosensing to the generation of microreactors by supramolecular self-assembly.

3.5 Reference

[1] M. DeLuca, Z. Shi, C. E. Castro, G. Arya, Nanoscale Horiz 2020, 5, 182; P. Wang, T. A. Meyer, V. Pan, P. K. Dutta, Y. Ke, Chem 2017, 2, 359; P. W. K. Rothemund, Nature 2006, 440, 297; F. Hong, F. Zhang, Y. Liu, H. Yan, Chemical Reviews 2017, 117, 12584; T. Tørring, N. V. Voigt, J. Nangreave, H. Yan, K. V. Gothelf, Chemical Society reviews 2011, 40, 5636.

[2] A. H. Okholm, H. Aslan, F. Besenbacher, M. Dong, J. Kjems, Nanoscale 2015, 7, 10970.

[3] R. Jungmann, M. S. Avendaño, J. B. Woehrstein, M. Dai, W. M. Shih, P. Yin, Nature methods 2014, 11, 313; M. Dai, R. Jungmann, P. Yin, Nat Nanotechnol 2016, 11, 798.

[4] J. Li, C. Fan, H. Pei, J. Shi, Q. Huang, Advanced materials 2013, 25, 4386; P. D. Halley, C. R. Lucas, E. M. McWilliams, M. J. Webber, R. A. Patton, C. Kural, D. M. Lucas, J. C. Byrd, C. E. Castro, Small 2016, 12, 308; Y.-X. Zhao, A. Shaw, X. Zeng, E. Benson, A. M. Nyström, B. r. Högberg, ACS nano 2012, 6, 8684; Q. Zhang, Q. Jiang, N. Li, L. Dai, Q. Liu, L. Song, J. Wang, Y. Li, J. Tian, B. Ding, ACS nano 2014, 8, 6633.

[5] A. R. Chandrasekaran, N. Anderson, M. Kizer, K. Halvorsen, X. Wang, Chembiochem 2016, 17, 1081.

[6] Q. Jiang, S. Liu, J. Liu, Z. G. Wang, B. Ding, Adv Mater 2019, 31, e1804785.

[7] S. Senapati, A. K. Mahanta, S. Kumar, P. Maiti, Signal Transduct Target Ther 2018, 3, 7; A. Wicki, D. Witzigmann, V. Balasubramanian, J. Huwyler, J Control Release 2015, 200, 138; S. Gupta, P. K. Gupta, G. Dharanivasan, R. S. Verma, Nanomedicine 2017, 12, 2675.

[8] S. D. Perrault, W. M. Shih, ACS Nano 2014, 8, 5132.

[9] J. Mikkila, A. P. Eskelinen, E. H. Niemela, V. Linko, M. J. Frilander, P. Torma, M. A. Kostiainen, Nano Lett. 2014, 14, 2196.

[10] N. Ponnuswamy, M. M. C. Bastings, B. Nathwani, J. H. Ryu, L. Y. T. Chou, M. Vinther, W. A. Li, F. M. Anastassacos, D. J. Mooney, W. M. Shih, Nat Comms 2017, 8, 15654.

[11] N. P. Agarwal, M. Matthies, F. N. Gür, K. Osada, T. L. Schmidt, Angewandte Chemie International Edition 2017, 56, 5460.

[12] S. T. Wang, M. A. Gray, S. Xuan, Y. Lin, J. Byrnes, A. I. Nguyen, N. Todorova, M. M. Stevens, C. R. Bertozzi, R. N. Zuckermann, O. Gang, Proc Natl Acad Sci U S A 2020, 117, 6339.

[13] L. Tang, V. Tjong, N. Li, Y. G. Yingling, A. Chilkoti, S. Zauscher, Adv Mater 2014, 26, 3050.

[14] L. Tang, L. A. Navarro, Jr., A. Chilkoti, S. Zauscher, Angew Chem Int Ed Engl 2017, 56, 6778.

[15] F. J. Bollum, in *The Enzymes*, (Ed: P. D. Boyer), Academic Press, New York 1974, 145.

[16] R. Gu, T. Oweida, Y. G. Yingling, A. Chilkoti, S. Zauscher, Biomacromolecules 2018, 19, 3525.

[17] D. C. Chow, W.-K. Lee, S. Zauscher, A. Chilkoti, Journal of the American Chemical Society 2005, 127, 14122; V. Tjong, L. Tang, S. Zauscher, A. Chilkoti, Chemical Society Reviews 2014, 43, 1612; S. Deshpande, Y. Yang, A. Chilkoti, S. Zauscher, in *Methods in enzymology*, Vol. 627, Elsevier, 2019, 163.

[18] D. S. Seferos, A. E. Prigodich, D. A. Giljohann, P. C. Patel, C. A. Mirkin, Nano letters 2009, 9, 308.

[19] E. Benson, A. Mohammed, J. Gardell, S. Masich, E. Czeizler, P. Orponen, B. Högberg, Nature 2015, 523, 441.

[20] L. Li, W. Sun, J. Zhong, Q. Yang, X. Zhu, Z. Zhou, Z. Zhang, Y. Huang, Advanced Functional Materials 2015, 25, 4101.

Chatper 4. Seeded DNA Origami Assembly Pathway Study

4.1 Abstract.

In this project, we will systematically investigate (1) how DNA molecules and complexes interact with the solid support in order to create dynamic surfaces and (2) how these interactions affect the self-assembly of tethered supramolecular complexes at the solid-liquid interface. The former will be addressed using a combination of single-molecule force spectroscopy and all-atom molecular dynamics simulations. The latter will be addressed through a combination of in situ imaging and lattice simulations, where we will compare two model systems of multicomponent supramolecular self-assembly: DNA origami and DNA bricks. Before tethering DNA nanostructure to the surface, we decided to study the seeded assembly process of DNA nanostructure in the solution first. The result of this study can provide useful suggestions for designing experiments for DNA assembly on the surface. More importantly, it can reveal the mechanism of DNA origami assembly in different ways.

4.2 Results and Discussions

4.2.1 4HB ends & 1/3 seeds comparison

We first design a small 1D DNA nanostructure, a 150nm four-helix-bundle to start this study. The 4HB was divided into 12 domains horizontally (Figure 1a), and each domain contains four 32nt staples (Figure 1b). To create seed domains, use two 64nt staples to hybridize with the scaffold at the selected domain before adding other staples (Figure 1c).

To study how the seed locations affect the assembly process, we choose to compare two different seeding ways. Seeds at ends has long staples seeding at domain 1 and 12, which are the two ends of the 4HB. Seeds at 1/3 has long staples seeding at domain 4 and 9, which are the two domains locating at 1/3 and 2/3 of the 4HB (Figure 1d). After seeding at chosen domains, the scaffold is locked at certain points, which makes it more organized for other staples to hybridized with and form designed structures. For the 1/3 design, two seeded domains separate the unhybridized scaffold into three parts, and the assembly is limited in the three small areas. On the other hand, although the scaffold is more organized after both ends locked in the end design, the staples still need to find their places around an overall large area between two seeds. Thus, we hypothesize that the assembly process after seeding at 1/3 is easier than seeding at ends.

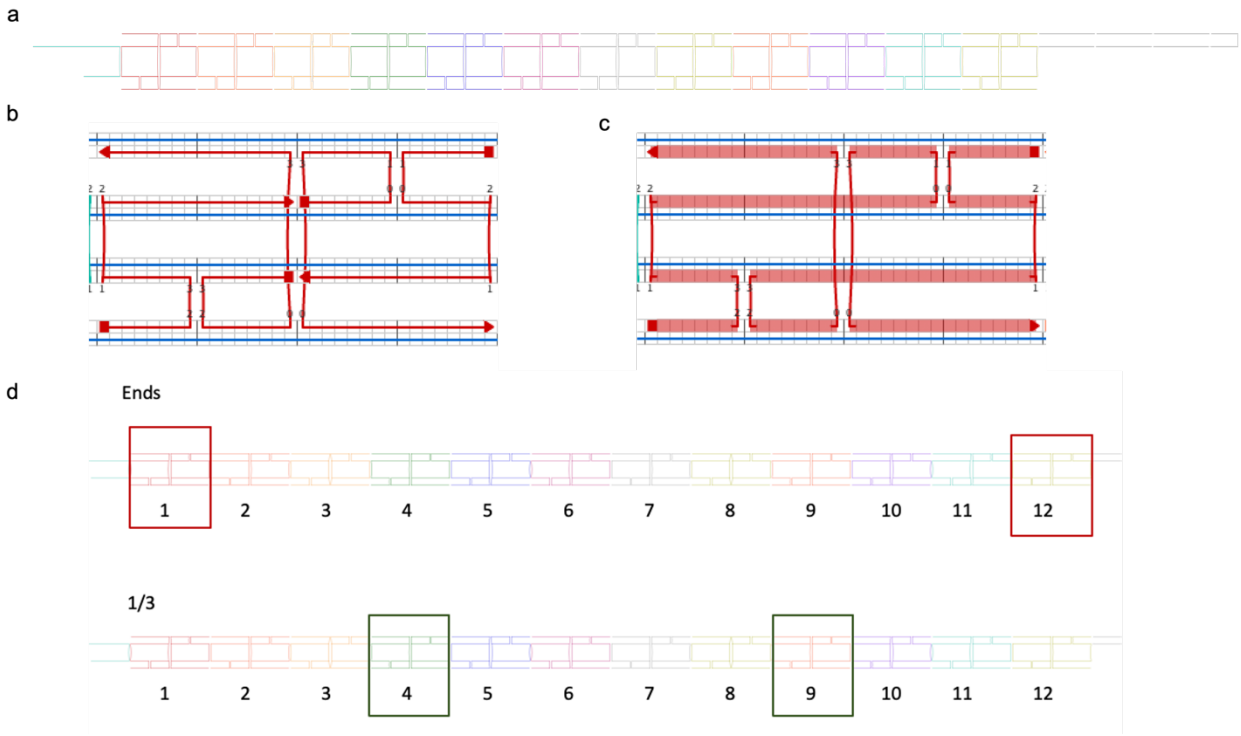

Figure 1. Design details of 4HB. (a) The design of 4HB, divided into 12 domains. (b) Four short 32nt staples at one domain. (c) Two long 64nt staples at one domain. (d) Ends design: seeding at domain 1 &12; 1/3 design: seeding at domain 4 &9.

The mobility of seeded scaffold, either ends or 1/3, is slower than fully assembled 4HB (Figure 2a). The mobility of ends seeded and 1/3 seeded scaffolds have no difference. While fully assembled 4HB looks like a 150nm nanorod (Figure 2b), the seeded scaffold was observed as swallowtail-like, unassembled structures (Figure 2c, 2d).

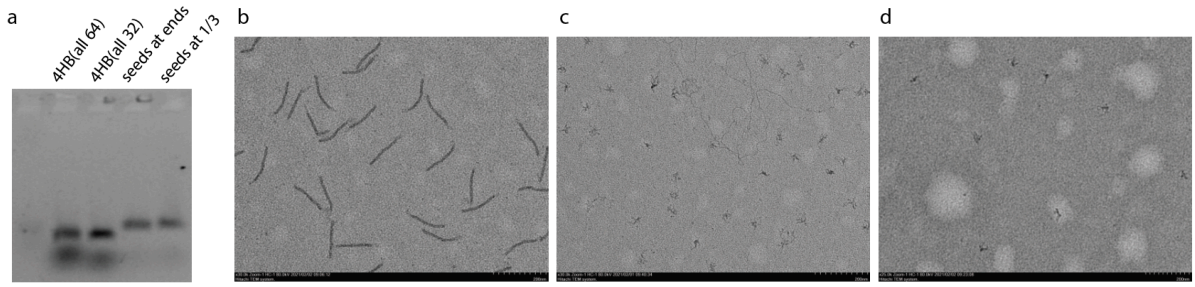

Figure 2. Differences of 4HB assembled with seeds. (a) Agarose gel of 4HB made of all 64nt staples, 4HB made of all 32nt staples, scaffold seeding at ends, scaffold seeding at 1/3. (b), (c), (d) TEM image of 4HB made of all 32nt staples, scaffold seeding at ends, scaffold seeding at 1/3.

In most cases, annealing protocols are used to produce DNA nanostructures. Here we decided to use isothermal incubation for the assembly since it only has two variables, one temperature and one time. This makes the comparison among different designs more controllable. Before comparing the assembly speeds of two seeded assemblies, we first tried different temperatures and times to find out the best isothermal condition for the assembly. Bare scaffold, scaffold seeded at ends, and scaffold seeded at 1/3 were incubated with the total set of 32nt staples under eight temperatures from 30°C to 65°C for 1h, 2h, and 4h. The agarose gel result shows that the assembly is completed starting from 50°C and most 4HB can be fully assembled after 2 hours as

these sharp bands suggested (Figure 3a). When reaching a higher temperature at 65°C, the bare scaffold cannot assembly while slight seeded scaffolds still assemble. This observation suggests that nanostructures assembled from seeded scaffolds could be more stable than those from the bare scaffold. To find out the exact point that unseeded scaffold starts not to assemble while seeded scaffolds assemble, we narrowed down the temperature range first from 50°C to 64°C, then from 59°C to 65°C and incubated the three sets of scaffolds for one hour. The critical point for the bare scaffold is around 60°C (60.4°C in the gel) (Figure 3b).

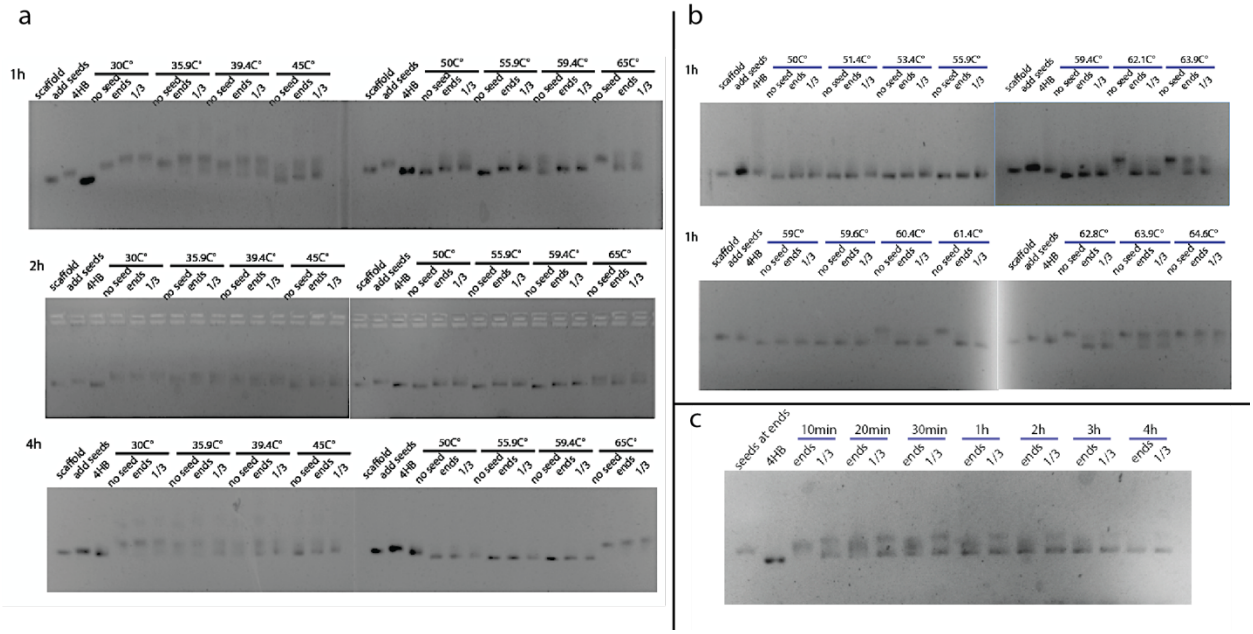

Figure 3. 4HB and 6HB assembly in different times and temperature. (a). Bare scaffold, scaffold seeded at ends and scaffold seeded at 1/3 were incubated with total set of 32nt staples under eight temperatures from 30°C to 65°C for 1h, 2h, and 4h. (b). Narrow down the temperature range to find out the critical point that unseeded scaffold starts not to assemble while seeded scaffolds assemble. (c). Locked 4HB assembly in different times.

Both seeded scaffolds can be assembled completely after 4 hours. Here, we use 60°C to incubate the two seeded scaffolds for seven time slots to track the assembly process. It can be observed that the assembly gradually accomplished by time based on the gel (Figure 3c). At each time slot, the intensity of the 4HB band of 1/3 is stronger than that of ends, especially at times less than one hour. Chart 1 shows the calculated 4HB yield assembled by ends and 1/3 seeded scaffold at different times. Based on this result, we can conclude that seeding at 1/3 of the origami makes the assembly pathway easier than seeding at ends, which demonstrates our previous hypothesis.

4.2.2 6HB assembly study

After 4HB, we decided to extend the assembly study to a larger and more complex structure. Here we chose a 400nm 6HB which is much longer than the 4HB. The 6HB has 27 domains and each contains six 42nt staples. To make seeds, four 63nt staples are used to replace 42nt staples at selected domains. The scaffold routing of 6HB has a seam at domain 14. While seeding at domain 13 can lock the left half of the scaffold, seeding at domain 14 locks both two halves of the scaffold and greatly decreases the difficulty of later assembly (Figure 4). We will study how this issue influences the assembly as well as further demonstrate assembly limited in small areas is easier than in rather large areas.

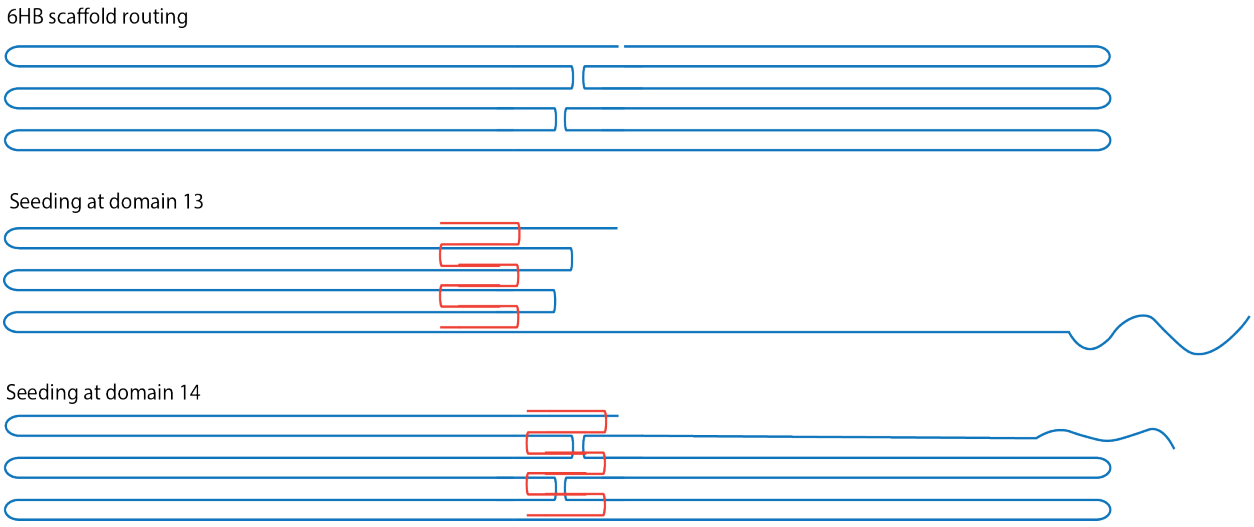

Figure 4. 6HB scaffold routing, and how seed at domain 13 and domain 14 lock the scaffold.

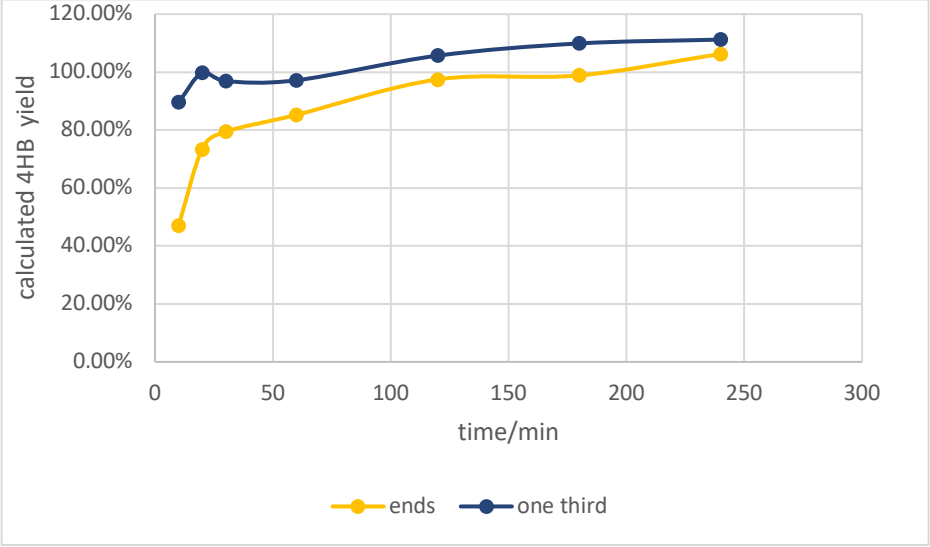

Chart 1. Calculated 4HB yield based on band intensities of ends and 1/3 design at different times.

We used a five-hour annealing protocol to bind seed strands to the scaffold. Seeded scaffolds showed different mobility in agarose gel. While seeds are not added, the scaffold shrunk into a thread ball and has high mobility. After seeds are added, the scaffold stretches a little bit to decrease the mobility. However, when more seeds are added, the structure becomes more organized, which can lead to higher mobility. Comparing to seeding at domain 1, 13, 27, the higher mobility of scaffold seeding at 1, 14, 27 suggests that locking the seam can organize the scaffold better (Figure 5a).

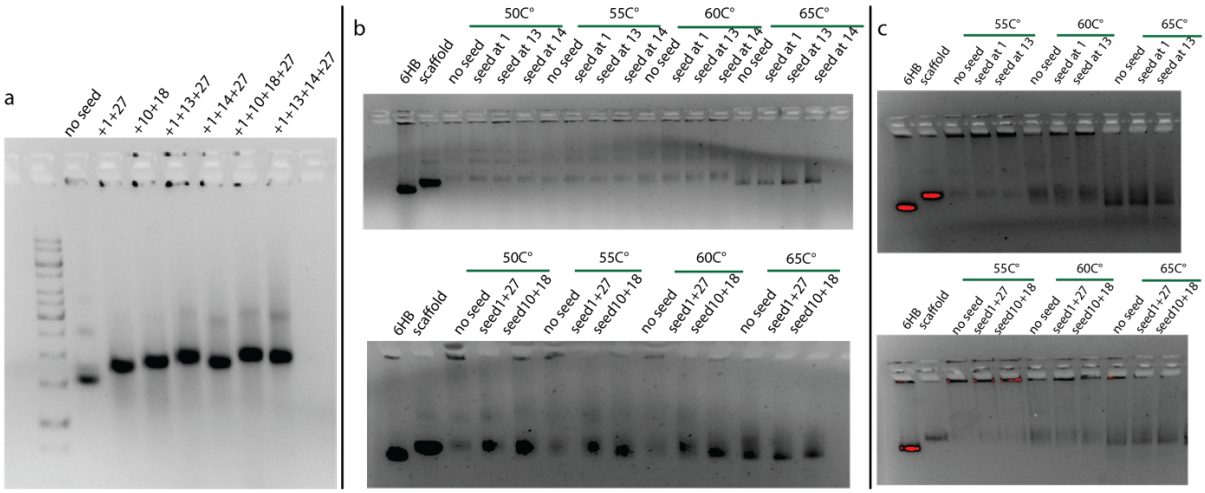

Figure 5. (a). Different mobilities of seeded scaffolds. (b). Seeded scaffolds assembly under 50, 55, 60, 65°C for 4 hours. (c). Seeded scaffolds assembly under 55, 60, 65°C for 6 hours.

Same as the 4HB, we tried different temperatures and times to find out the best isothermal condition for 6HB assembly. We use one seed (1, 13, 14), and double seeds (1+27, 10+18) scaffolds to incubate at 50, 55, 60, 65°C for 4h, and then 55, 60, 65°C for 6h (Figure 5b, 5c). There is almost no difference among seeded scaffolds and no seed control under every condition, which means one or two seeds are too less to change the assembly progress for this larger

structure. The assembly tends to complete at 65°C after 6h. We image the purified 6HB under this condition with TEM. Though most 6HB have a clear structure and reach 400nm, part of them have one or two unassembled points causing folding (Figure 6b). Thus, we tried to increase the time and temperature to reach a better assembly yield. Figure 6a showed the gel result of assembly under 65°C 8h, 70°C 6h, and 65°C 10h. Increasing the temperature to 70°C leads to much aggregate. Even though the 6HB under 70°C looks more completed, the low yield makes it not usable (Figure 6e). 65°C 8h has a better result than 65°C 6h, but still has some uncompleted structure (Figure 6c). 65°C 10h has the best yield compared to others and forms the best nanostructure observed under TEM (Figure 6d). We can conclude that 6HB could be fully assembled under 65°C after 10 hours.

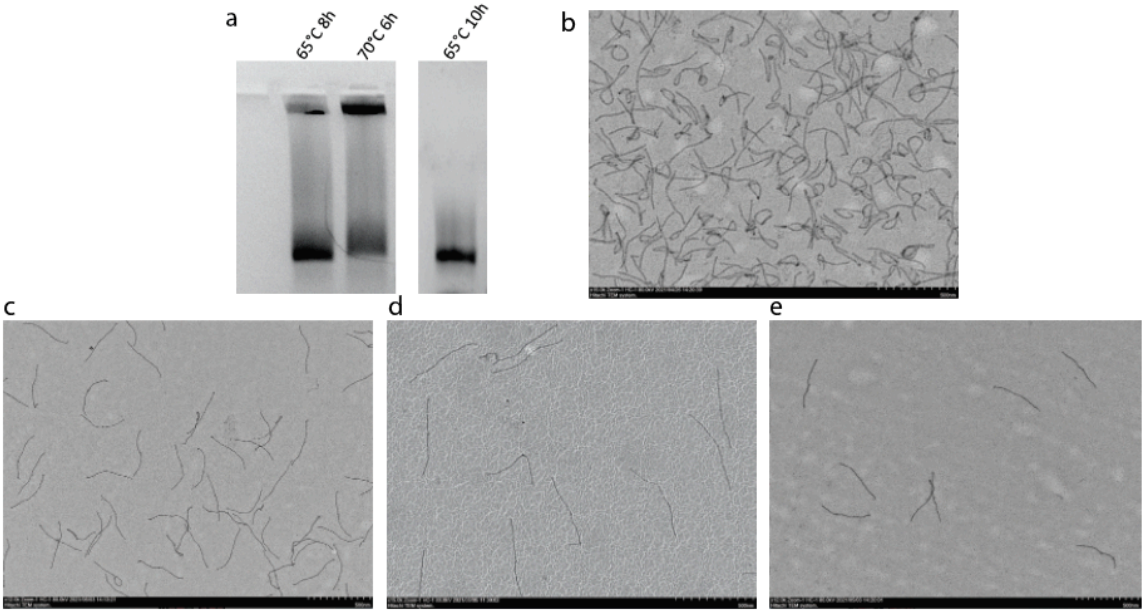

Figure 6. (a). Agarose gel of 6HB assembled at 65°C 8h, 70°C 6h, 65°C 10h. (b, c, d, e). TEM images of 6HB assembled at 65°C 6h, 65°C 8h, 70°C 6h, 65°C 10h.

Then, we incubated ends seeds, 1/3 seeds, seeds at ends with domain 13 and with domain 14 (seam domain) assembly tracking under 65°C from 1h to 4h to compare their assembly progress (Figure 7a). At 1h, 2h, and 3h, seeds at ends with domain 14 has a stronger intensity of 6HB band than that of seeds at ends with domain 13 (Figure 7b). This demonstrates that locking the seam of the scaffold does help to improve the assembly. However, no difference shows between ends seeds and 1/3 seeds. It might because two seeds are too less to change the assembly progress. Thus, we tried to seed at three domains with long staples instead of only one to study.

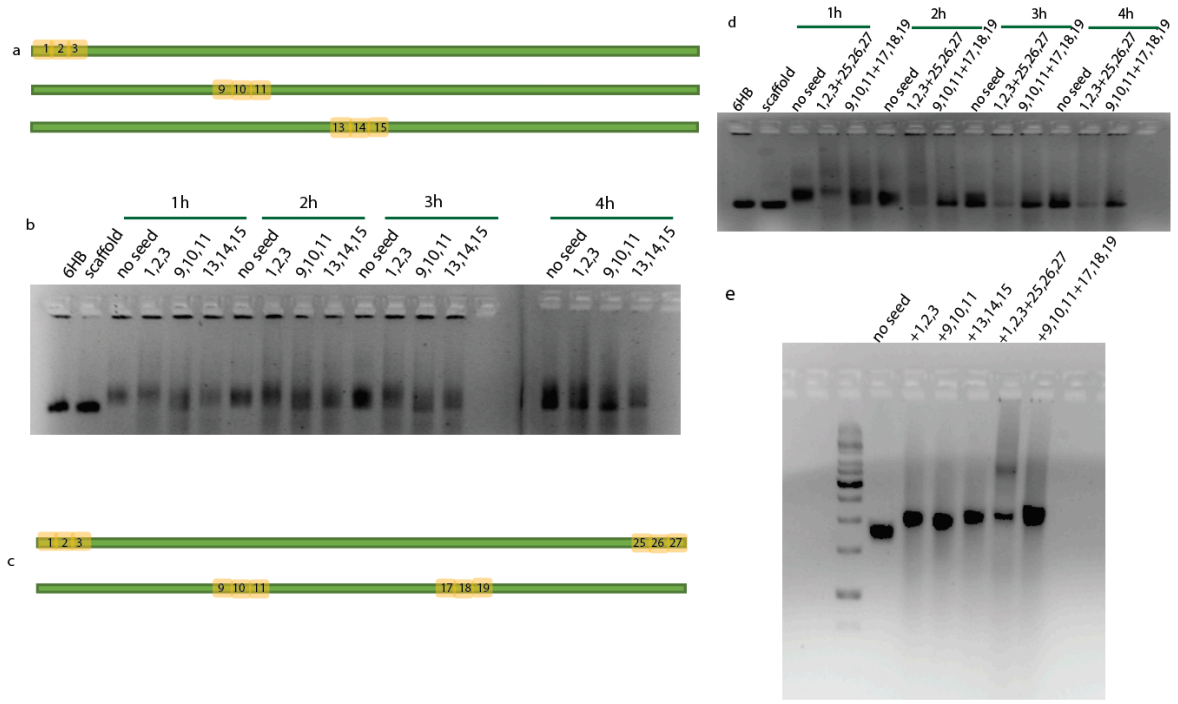

Figure 7. (a) Locations of one set three-domain seeds. (b) Seeds (1, 2, 3), seeds (9, 10, 11), seeds (13, 14, 15) assembly tracking under 65°C from 1h to 4h. (c). Locations of two sets three-domain seeds. (d) Ends seeds (1, 2, 3 + 25, 26, 27), 1/3 seeds (9, 10, 11 + 17, 18, 19) assembly tracking under 65°C from 1h to 4h. (e). Agarose gel of three-domain seeded scaffolds.

After binding three-domain seed strands to the scaffolds (Figure 7e), we first tracked the assembly of one three-domain seeded scaffold, one end (1, 2, 3), one 1/3 (9, 10, 11), and the center (13, 14, 15) (Figure 7a). Based on the previous discussion, the rank of assembly speed should be the center > 1/3 > end. Surprisingly, the actual rank of speed is 1/3 > the center > one end (Figure 7b). This probably because the short 1/3 divided by seed (9, 10, 11) can be quickly assembled. The mechanism needs to be studied further. When we tracked the three-domain ends and 1/3 assembly (Figure 7c), it was obvious that 1/3 assembled faster than ends (Figure 7d). This result reconfirmed the hypothesis that assembly limited in small areas is easier than in rather large areas.

4.2.3 FRET (fluorescence resonance energy transfer) experiments

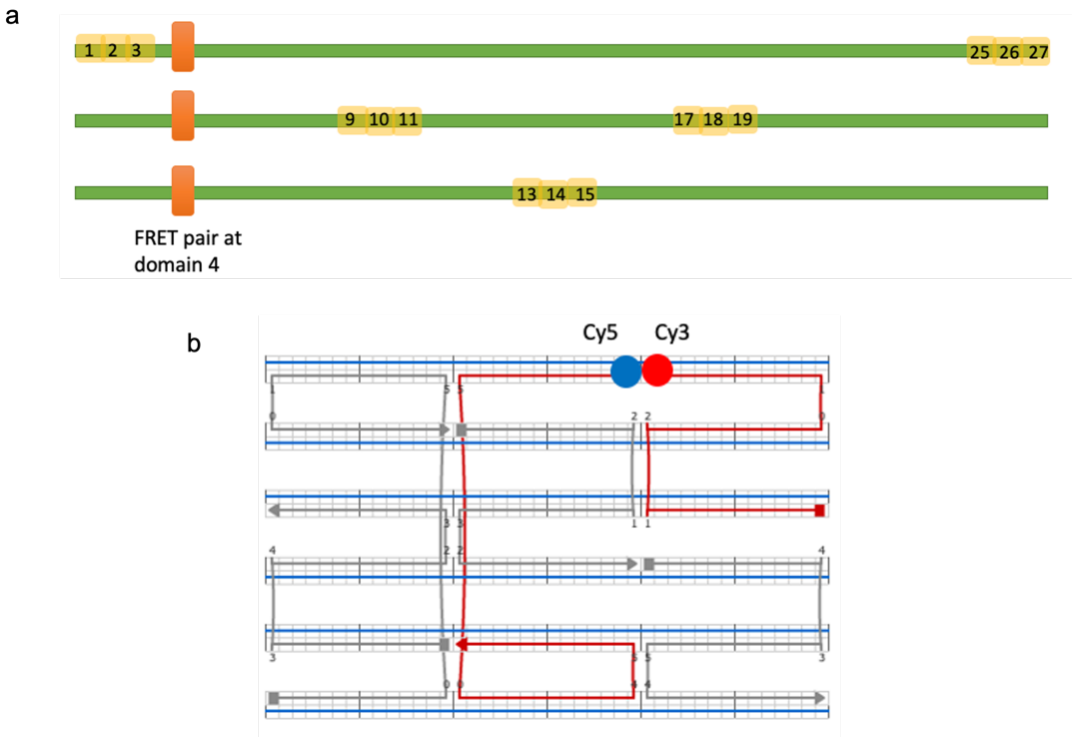

Figure 8. FRET pairs design. (a) FRET pair locations at the 6HB. (b) Cy3, Cy5 staples' locations

We have demonstrated that 1/3 seeded scaffold assembled faster than ends seeded in 6HB through gel. Further, we would like to use FRET to track the process. After using long staples to lock the scaffold at certain locations, the scaffold around the seed can be brought closer to each other. Thus, we hypothesis that staples closed to the seeded area can hybridized faster than others since the scaffold makes them easier to bind with. To demonstrate this, we design the FRET experiments with Cy3 and Cy5 staples pair near the ends seed (Figure 8b). While incubating them with ends, 1/3, center seeded scaffolds as well as other staples, the FRET signal increasing is supposed to be ends > 1/3 > center.

4.3 Methods and Technologies

Annealing protocol of DNA origami: 4HB and scaffold seeding for 4HB & 6HB shared the same annealing protocol. Scaffolds are mixed with 10 folds of staples in need and diluted in a 1 × TBE, 10mM $MgCl_2$, 50uL solution to make the final concentration of the scaffold as 30nM. Heat the solution at 90°C for 5 min, then lower temperature to 60℃ and decrease to 25 ℃ in increments of 1 ℃ every 10 min. For 6HB, the scaffold is mixed with 10 folds of staples in need,

and diluted in a 1 × TBE, 10mM $MgCl_2$, 50uL solution to make the final concentration of the scaffold as 30nM. Heat the solution at 90°C for 5 min, then lower temperature to 60℃ and decrease to 25 ℃ in increments of 1 ℃ every 20 min. Extra staples are not removed for later use. The scaffold of 4HB is pScaf 1800, and of 6HB is p7308.

Isothermal incubation: Adding 10 folds of total set staples to seeded / unseeded scaffold and dilute it to 10nM with 1 × TBE, 10mM $MgCl_2$ buffer. Then divide the mixture to 5uL each tube, incubate them at desired temperatures for the chosen time.

Agarose Gel Analysis: Samples were analyzed with a 1.5% agarose gel in 0.5X TBE with 10mM Mg^{2+} as the running buffer (45 mM Tris, 45 mM boric acid, 1 mM EDTA, and 10 mM Mg^{2+}, pH=8.0) for 150 min at 75 V under 4 ℃. Gels were pre-stained with 1X Ethidium Bromide for visualization. We imaged the gels using a Bio-Rad Gel Doc EZ Imager.

Transmission electron microscopy (TEM) imaging: 20-30 ng sample solutions were deposited onto charged, carbon film-coated copper EM grids and incubated for 30 s after which excess solvent was blotted and removed with filter paper. 8 μL 1% uranyl formate (UF) solution was used for negative staining, and as before, excess liquid was blotted and removed with filter paper after 20 s incubation time. We imaged the samples using a Hitachi HT-7700 120 kV W (Tungsten) TEM with AMT CCD camera.

Chapter 5. Other Contributions

As a PhD student working on various applications lying on the interfaces between DAN nanotechnology and other fields, I designed DNA origamis and small DNA structures to fit in other works in electrical engineering, film deposition, and virus behaviors. Although these work does not fit into the scope of this dissertation, I list these projects below.

1. **Artificial HIV capsid mimicked by DNA nanostructure** (Collaboration with Melikian Lab in Emory University)
   • De Novo designed a complex DNA framework mimicking the structure of HIV capsid
   • Conjugated a DNA handle to HIV capsid protein and attached it to the artificial DNA structure
2. **DNA nanoswitch in microelectrode** (Collaboration with Wang Lab in Georgia Tech)
   • Fabricated a self-designed 2um DNA nanorod as the nanoswitch
   • Modified the DNA nanostructure with a fluorescent dye and imaged the nanoswitch on the electric device
   • Attached the DNA nanorod on carbon nanotube to increase the conductivity of the nanoswitch
3. **Electric field-controlled DNA nanospring** (Collaboration with Cai Lab in Georgia Tech)
   • Designed DNA oligos attached to electric surfaces and formed them as nanospring for the electric field test
4. **Deposition of DNA Nanostructures on Hydrophobic Surfaces** (Collaboration with Liu Lab in University of Pittsburgh)
   • Modified DNA nanorods with single-strand nucleotides in different locations for the test on hydrophobic surfaces

Hui, L; **Lu, Q**; Zhou, K; Duan, Y; Ke, Y; Wang, R; Liu, H. “Deposition of DNA Nanostructures on Polymer Surfaces”, manuscript submitted to Advanced Materials

5. **Electrical Conductance of DNA Origami Nanowires Study** (Collaboration with Hihath Lab in UC Davis)

• Produced DNA 6HB dimer and 10HB 5mer and attached fluorescent dye to them

Jonathan Marrs, **Qinyi Lu**, Victor Pan, Yonggang Ke, Joshua Hihath, Structure-Dependent Electrical Conductance of DNA Origami Nanowires. *ChemBioChem.*